RECLAMATION

Managing Water in the West

Technical Memorandum 85-833000-2017-15

Integrated Subsurface Geologic Model, Paradox Valley, Colorado

Colorado Basin Salinity Control Project,
Paradox Valley Unit, Colorado
Upper Colorado Region

U.S. Department of the Interior
Bureau of Reclamation

June 2018

Mission Statements

The mission of the Department of the Interior is to protect and provide access to our Nation's natural and cultural heritage and honor our trust responsibilities to Indian Tribes and our commitments to island communities.

The mission of the Bureau of Reclamation is to manage, develop, and protect water and related resources in an environmentally and economically sound manner in the interest of the American public.

BUREAU OF RECLAMATION
Technical Service Center, Denver, Colorado
Seismology, Geomorphology, and Geophysics Group, 86-68330

Technical Memorandum 85-833000-2017-15

Integrated Subsurface Geologic Model, Paradox Valley, Colorado

Colorado Basin Salinity Control Project,
Paradox Valley Unit, Colorado
Upper Colorado Region

Prepared by:

VANESSA KING Digitally signed by VANESSA KING Date: 2021.08.25 12:01:05 -07'00'

Vanessa M. King, geophysicist — Date

CHRISTOPHER WOOD 2021.08.25 16:21:47 -06'00'

Christopher K. Wood, geophysicist — Date

LISA BLOCK Digitally signed by LISA BLOCK Date: 2021.08.25 09:18:12 -06'00'

Lisa V. Block, geophysicist — Date

Peer Review Certification

This report has been reviewed and is believed to be in accordance with the service agreement and standards of the profession.

Peer reviewed by:

GLENDA BESANA-OSTMAN Digitally signed by GLENDA BESANA-OSTMAN Date: 2021.08.25 09:36:48 -06'00'

Glenda Besana-Ostman, geophysicist — Date

Contents

Tables

Page

Figures

Page

1 Introduction

The Bureau of Reclamation (Reclamation) operates a deep injection well at Paradox Valley in western Colorado (Figure 1-1), as part of the Paradox Valley Unit (PVU) of the Colorado River Basin Salinity Control Program (CRBSCP). Paradox Valley, overlying a salt anticline, is a major contributor to the salt load of the Colorado River. The Dolores River, a tributary of the Colorado, picks up about 205,000 short tons (185,000 metric tons) of salt annually from natural brine inflows as it crosses Paradox Valley. PVU was authorized for construction by the Colorado River Basin Salinity Control Act of 1974 (Public Law 93-320; amended in 1984 as Public Law 98-569).

The purpose of PVU is to divert up to 90 percent of the Paradox Valley brine inflows from entering the Dolores River, where they would substantially degrade water quality. Subsurface brine flows are intercepted by long-term pumping from a field of shallow extraction wells located along the river. The extracted brine is then collected and filtered at a surface-treatment facility, piped about 3.6 miles (6 km) to an injection facility at the edge of the valley, and finally injected into a 15,900-ft (4.8-km) deep injection well for long-term disposal. The injection well is designed to dispose of brine deep underground, confined to a narrow target zone extending over only the lowest 1,700 ft (500 m) of the borehole. Within this target zone, most of the injected brine is taken up by the Leadville formation, a subhorizontal formation of Mississippian-age limestone.

From about 2008 through 2012, the pressure required to inject brine was steadily increasing (Figure 1-2), and was approaching the maximum allowable surface injection pressure (MASIP) as permitted by the U.S. Environmental Protection Agency (EPA). The rate of near-well induced earthquakes was also increasing. Following an M_L 4.4 earthquake in January, 2013, the injection flow rate was decreased, which resulted in decreased well-head pressures and near-well seismicity rates. Recent trends of pressures and seismicity rates indicate that these beneficial effects of the operational changes made in 2013 are diminishing (Block, 2017), and that further reductions in injection rate are likely. As the injection rate is reduced, the project benefits are diminished, and the project becomes less economical to operate. Various alternatives therefore are under consideration to dispose of brine in the future, including the drilling of a second injection well.

There are numerous factors involved in the siting of a second injection well, including the subsurface geologic structure, seismic hazard, the feasibility of drilling a well, the feasibility of developing and maintaining surface infrastructure, land use, ownership, environmental concerns, etc. Only the subsurface geologic structure is discussed in this report; other factors are discussed elsewhere.

The Leadville formation and Paradox salt are the primary layers of interest, as these layers serve as the primary injection target formation and confining layer, respectively, in the existing injection well, and are likely to serve the same roles in a second injection well. A geologically

favorable site for a second well would have the following characteristics: (1) the Leadville formation has relatively high values of thickness, porosity, and permeability, (2) the Leadville formation is deep enough to allow injection above the fracture closure pressure without breaching the confining layer, but not so deep as to dramatically increase drilling costs, (3) the reservoir has a large spatial extent, (4) the Paradox formation has adequate thickness, quality, and spatial extent to serve as a confining layer, but is not so thick as to dramatically increase drilling costs, and (5) the reservoir has not already been pressurized by past injection.

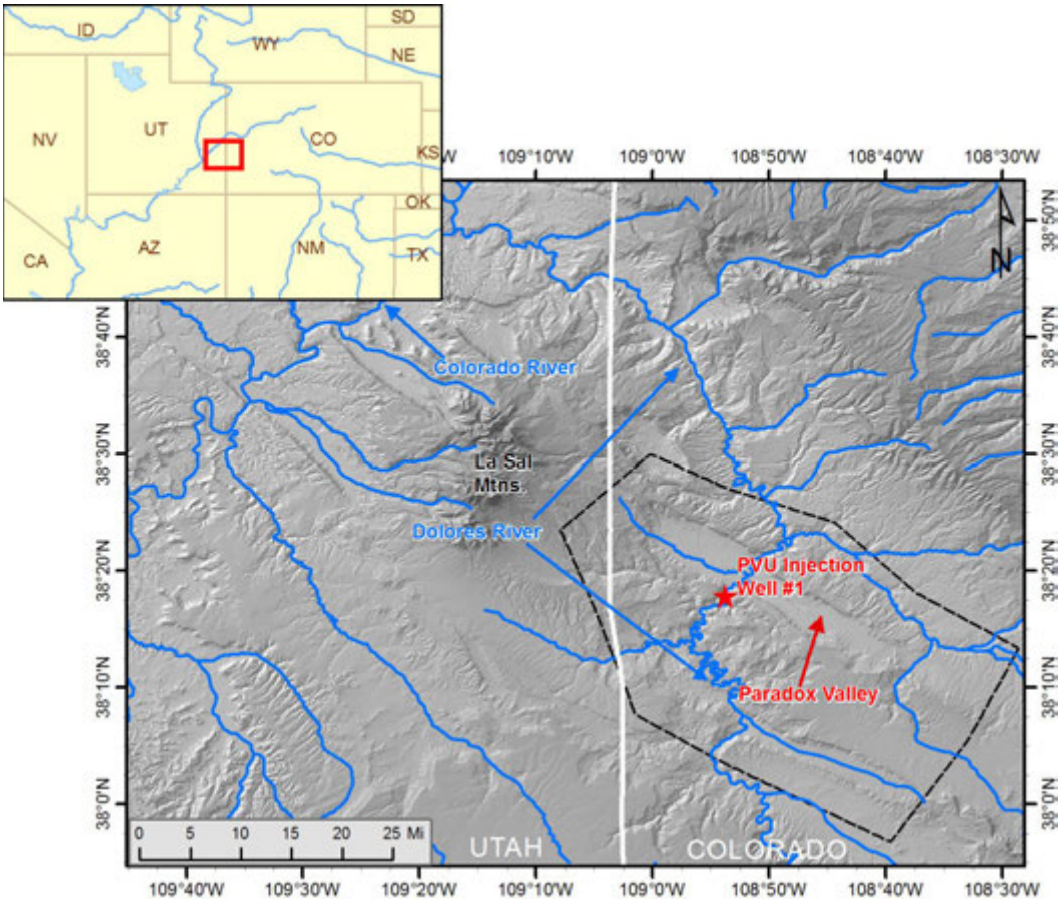

Figure 1-1. Location of the deep injection well at Reclamation's Paradox Valley Unit in western Colorado. Dashed line outlines the area of interest (AOI).

The geologic studies that were used to site PVU Injection Well #1 in the 1980s covered a relatively small area and used limited amounts of data. In order to determine the most geologically favorable site for a second injection well, we have created an integrated geologic model that covers the area shown by the dashed polygon in Figure 1-1. This model includes information from 2D seismic reflection data, well logs from oil and gas wells drilled in the area, aeromagnetic and gravity data, earthquake data, stress data, and InSAR data. These studies are summarized in Section 4. In Section 5, results from these studies are compared and conclusions about relevant formation properties are summarized. In addition, a coupled geomechanical and flow model that was developed based on the subsurface geologic information from the other studies is described.

Approximately 20 potential injection sites were initially selected, based primarily on the feasibility of building and operating surface infrastructure, as well as the limited information that was known about the subsurface geology at that time. The initial sites were bounded by a polygon that we refer to as the area of interest (AOI) (Figure 1-1). The set of sites has since been refined and reduced, but in this TM we discuss the subsurface geology of the entire polygon.

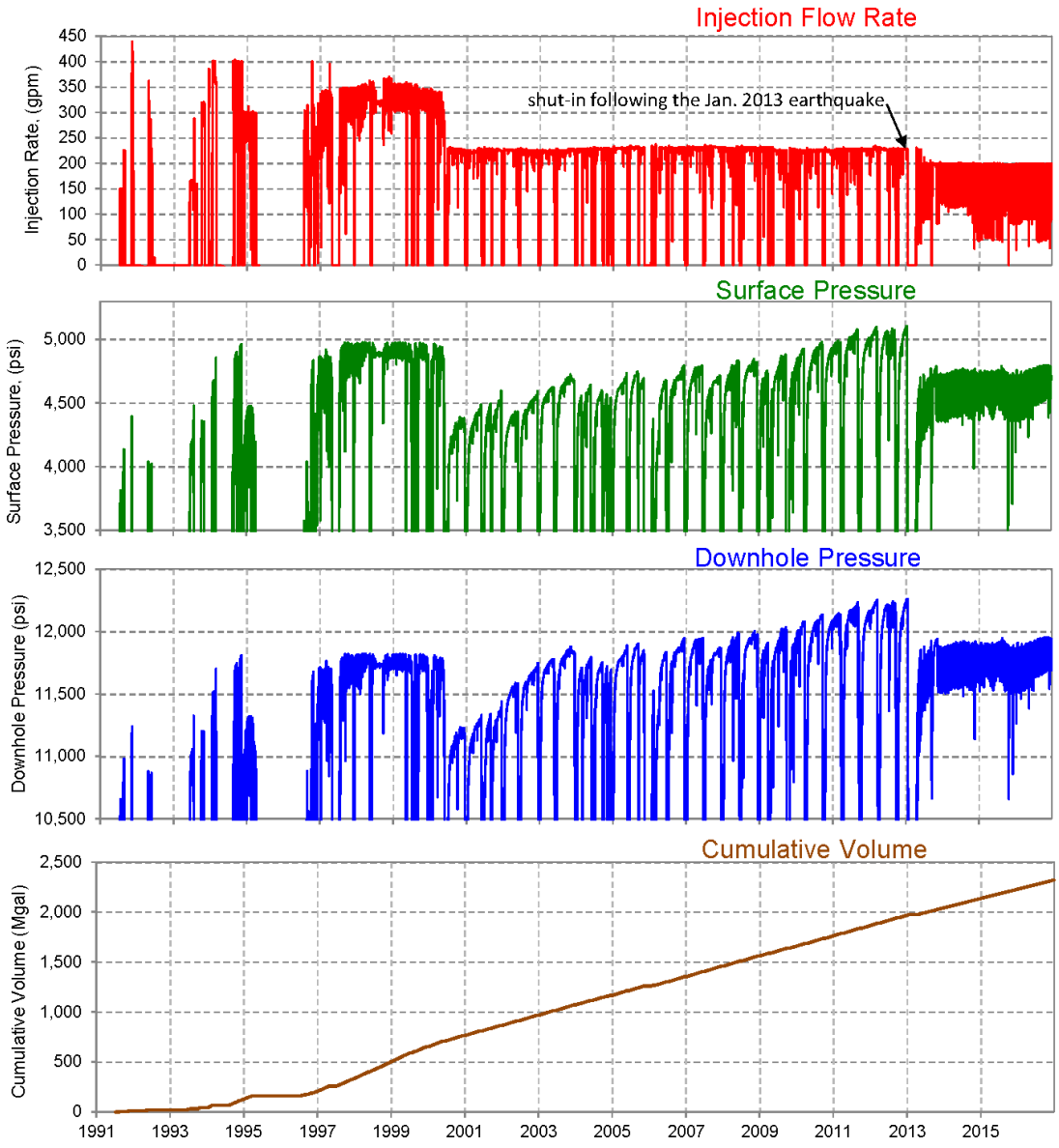

Figure 1-2. Daily average injection flow rate, daily average surface injection pressure, daily average downhole pressure at 4.3 km depth, and cumulative volume of fluid injected from 1991 to 2016. The downhole pressures are computed from the measured surface pressures using the density of the brine in the well. Figure from Block (2017).

2 Geology

2.1 Regional geology

2.1.1 Geologic setting

Paradox Valley is located in the northeastern part of Paradox Basin—an elongate northwest-southeast trending structural basin which extends from eastern Utah into western Colorado, within the Colorado Plateau region (Figure 2-1). Rapid subsidence of Paradox Basin during the Mississippian, Pennsylvanian, and Permian Periods accommodated marine intrusion and resulted in the interfingering of marine deposits, including evaporites, and terrestrial material shed from the Uncompahgre uplift to the northeast (McClure and others, 2003).

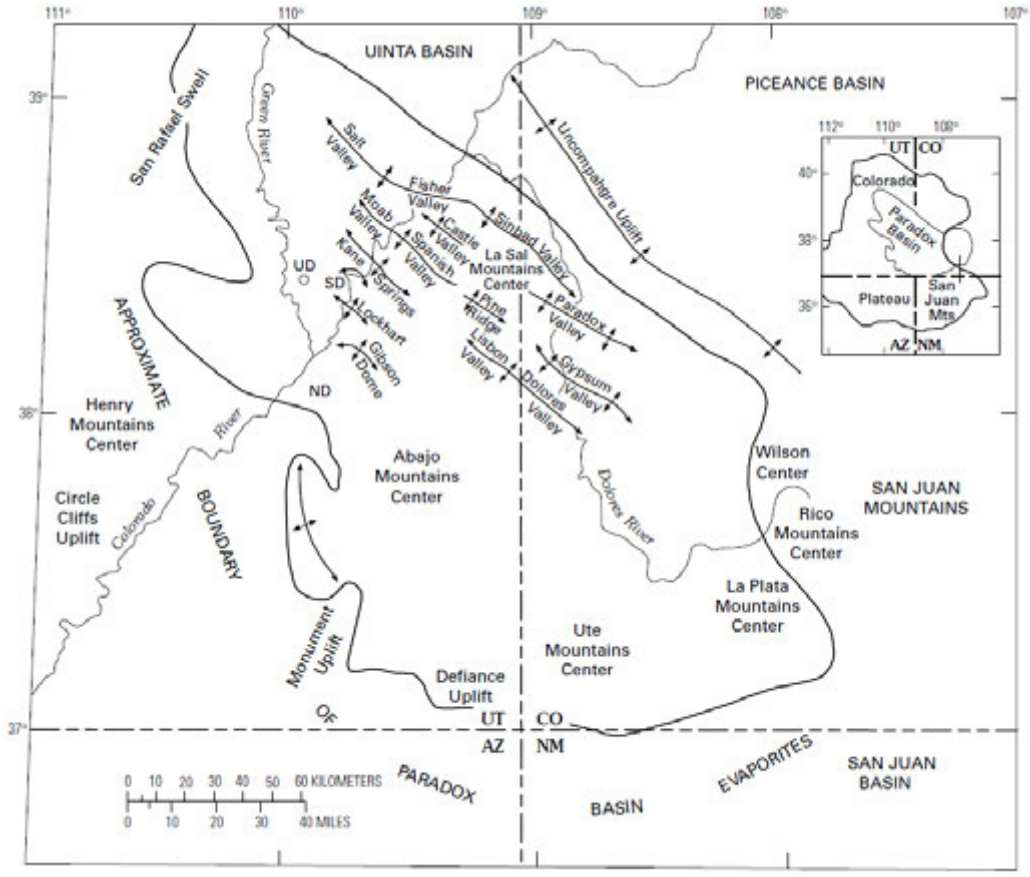

Figure 2-1. Map showing the location and major features of Paradox Basin. Paradox Valley is located near the northeastern edge of Paradox Basin. Figure taken from Grout and Verbeek (1988).

The northern part of Paradox Basin, known as the Paradox fold and fault belt, contains several northwest-striking diapiric salt-cored anticlines. These salt-cored anticlines developed as a result of plastic flow of the Pennsylvanian-age Paradox stratigraphic unit. The Paradox unit consists of

as much as 85% halite and is best imagined as a viscous liquid (Huntoon, 1988). Subsequent dissolution of salt beneath the crests of some of the anticlines resulted in downfaulting and the development of grabens, or salt valleys (Nuccio and Condon, 1996; Gutierrez, 2004). Paradox Valley developed by structural collapse along the crest of one of these salt-cored anticlines and is bounded by nearly vertical normal faults.

2.1.2 Faults and joints

The tectonic history of northern Paradox Basin is complex, as are the resulting fault and joint patterns. This region contains both deep basement faults, possibly originating as long ago as the Precambrian (Baars and Stevenson, 1981), and Tertiary-age surface faults. Sets of joints or fractures are present in both the older and younger rock units. Although these joints are often sub-parallel to the faults, the developmental relationship of the fault and joint patterns is not always clear (Grout and Verbeek, 1998). Varying and sometimes conflicting interpretations of the tectonic development and relationships of the observed structural features of the Paradox fold and fault belt have been published. Here we present an overview of the major regional fault and joint patterns observed rather than a detailed tectonic history.

2.1.2.1 Buried Faults

Parallel, northwest-trending, steeply-dipping normal faults are present in the basement and buried Paleozoic rock units of the Paradox fold and fault belt. The presence of these northwest-trending basement faults contributed to the formation of the northwest-trending diapiric salt anticlines (Baars and Stevenson, 1981; Friedman and others, 1994; Grout and Verbeek, 1998). Although some vertical movement occurred on these faults during the early Paleozoic (Baars and Stevenson, 1981), activity along the faults greatly increased during the Mississippian Period, when Paradox Basin began rapidly subsiding. Significant activity continued on these faults into the Permian Period, and possibly into the Triassic Period. The faults may have been reactivated as late as the Tertiary (Doelling, 1988; Grout and Verbeek, 1998). The faults having the largest vertical displacements generally have their downthrown sides to the northeast, resulting in a deepening of Paradox Basin toward the northeast (Doelling, 1988). In the vicinity of Paradox Valley, these northwest-trending basement faults occur on the northeast flank of the Wray Mesa-Sneffels structural high trend and are referred to in early PVU geology reports as the Wray Mesa fault system (Bremkamp and Harr, 1988).

Northeast-trending fault zones are also present in the basement and buried Paleozoic rocks of northern Paradox Basin. According to Baars and Stevenson (1981), these features, along with the northwest-trending basement faults described above, originated as conjugate shear zones during the Precambrian. While significant vertical movement occurred on the northwest-trending faults during the late Paleozoic (described above), the northeast-trending faults appear to have accommodated mainly strike-slip movement. These northeast-trending basement lineaments are not as well mapped or as well understood as the northwest-trending faults. It is not known whether each of these northeast-trending features consists of a wide shear zone, a single wrench fault, or a series of en echelon strike-slip faults (Hite, 1975). Some of the northwest-trending basement faults are offset by northeast displacement (Hite, 1975), indicating activity along the northeast features at least subsequent to the late Paleozoic. The laccolith complex of the La Sal Mountains, which is located just northwest of Paradox Valley and divides the Paradox Valley - Castle Valley anticlinal structure in two (Figure 2-1), may be located at the intersection of the anticline with one of these northeast-trending fault zones (Friedman and others, 1994).

2.1.2.2 Surface Faults

Many relatively young normal faults are present at the surface in Paradox Basin. Some of these faults may be the result of tectonic extension during the Tertiary, while others are clearly related to salt dissolution and collapse of overlying strata (Doelling, 1988). Regardless of the cause of the fault formation, the faults generally trend northwest-southeast, parallel to the salt anticlines and underlying basement normal faults. Salt diapiric movement, salt dissolution, and the lowering of salt valley floors are continuing (Friedman and others, 1994).

Extensional, northeast-trending, high-angle faults with predominantly vertical offset have also been mapped at the surface in northern Paradox Basin. According to formation cutting relations, these faults were active sometime from Jurassic to Pleistocene time, in strata between the salt section and the surface (Friedman and others, 1994).

2.1.2.3 Joints

Several widespread, extensional joint sets are present across central Paradox Basin. Grout and Verbeek (1998) classify these joint sets into two major systems, one that evolved during the Permian Period and another system of Tertiary and younger age. In addition, a system of Carboniferous-age joint sets is present in Mississippian and older rocks along the eastern margin of Paradox Basin. Regardless of age, each system consists of joint sets striking from northwest to northeast. Strikes of the Paleozoic-age joint sets, which are likely to be present in the sub-salt rock units in the vicinity of Paradox Valley, are reported as: N62W, N27W, N19W, N18E, and N64E, measured from outcrops near Telluride, Colorado, approximately 75 miles southeast of PVU (Grout and Verbeek, 1998). In the Lisbon Valley area in eastern Utah (Figure 2-1), these joint sets are perpendicular to bedding, indicating that they formed prior to the major anticline-building episode in the late Permian to early Triassic (Grout and Verbeek, 1998). Strikes of the Tertiary-age joints range from N85W to N62E. The majority of these joint sets are vertical, regardless of bedding dip.

2.2 Local Geology

Paradox Valley and the surrounding mesas contain rocks spanning Precambrian to mid-Cretaceous time (>570 to approximately 90 Ma). The Precambrian basement rock consists of granite, schist, gneiss, and pegmatite. Overlying the Precambrian rock is a series of sedimentary units deposited primarily in marine or near shore environments. These layers include sandstones, siltstones, shales, conglomerates, limestones, dolomites, and evaporites.

A stratigraphic column of the Paradox Valley area is presented in Table 2-1. PVU Injection Well #1 is sited on the Triassic-age Chinle Formation. The stratigraphy of the underlying formations shown in Table 2-1, down to the Precambrian basement rock, is taken from the geologic well log of this borehole (Harr, 1988). Depths of geologic units encountered in this well are included in the table and are relative to the local ground surface elevation of 4996 ft. Descriptions of the rock units are taken from several sources (see footnote no. 2 in the table). The overlying stratigraphy, including the Triassic-age Wingate sandstone to the Cretaceous-age Mancos shale, was taken from a geologic map of the Moab Quadrangle produced by the U.S. Geological Survey (Williams, 1964). Not all rock units may be present in the immediate vicinity of Paradox Valley. The Jurassic-age Morrison Formation generally tops the cliffs surrounding Paradox Valley, while

the Cretaceous-age Burro Canyon and Dakota Formations are present at the higher elevations of the mesas. A remnant of the Mancos shale is present just beyond the southeastern end of the valley. The floor of Paradox Valley consists of Quaternary alluvial and eolian deposits overlying the diapiric Paradox (salt) formation.

The thickest stratum found in the vicinity of the wellhead was termed the Cutler formation (Harr, 1988). However, the rocks designated the "Cutler formation" actually consist of several rock types, which are both Permian and Pennsylvanian in age, while the type Cutler strata exposed at Cutler Creek in Ouray, Colorado are likely wholly Pennsylvanian in age (Rasmussen, 2014), and thus the term Cutler formation has fallen out of favor. While some authors have used terms such as "Cutler group," (Condon, 1997; Thomas, 2007; Dubiel and others, 2009), Rasmussen (2014) argues that the Cutler group combines the White Rim Sandstone and Organ Rock formation, which have unique characteristics and are separated by a regional unconformity, and that the underlying undifferentiated rocks should be subdivided and assigned to their proper formations or cycles within the Hermosa Group, thus rendering any use of the term "Cutler" unnecessary. Here, we continue to use the term "Cutler formation" for consistency with Harr (1988), although the White Rim formation is also used in the seismic reflection interpretation (Section 4.1).

Table 2-1. Paradox Valley stratigraphy.

Stratigraphic Unit	Depth[1]	Description[2]
CRETACEOUS[3] (145-65 Ma)		
Mancos Shale	Above elevation of wellhead	Dark gray to black, soft, fissile marine shale with thin sandstone beds at various horizons.
Dakota Sandstone		Friable to quartzitic fluvial sandstone and conglomeratic sandstone with interbedded carbonaceous nonmarine shale.
Burro Canyon Fm.		Fluvial sandstone and conglomerate interbedded with lacustrine siltstone, shale, and mudstone, and thin beds of impure limestone.
JURASSIC (205-145 Ma)		
Morrison Fm.	Above elevation of wellhead	Fluvial and lacustrine shale, mudstone, and sandstone; local thin limestone beds.
Summerville Fm.		Sandy shale and mudstone of terrestrial origin.
Entrada Sandstone		Fine- to medium-grained, massive, and cross-bedded eolian sandstone; basal few feet may consist of red siltstone and fine-grained sandstone and is sometimes referred to as the Carmel Formation.
Navajo Sandstone		Fine-grained, cross-bedded eolian sandstone.
TRIASSIC (255-205 Ma)		
Kayenta Fm.	Above elevation of wellhead	Irregularly interbedded fluvial shale, siltstone, and fine to coarse-grained sandstone.
Wingate Sandstone		Fine-grained, massive, thick-bedded and prominently cross-bedded eolian sandstone.
Chinle Fm.	0 (at surface)	Siltstone interbedded with lenses of sandstone and shale, limestone-pebble and shale-pellet conglomerate, with lenses of grit and quartz-pebble conglomerate near base. Terrestrial depositional environment.
Moenkopi Fm.	390	Sandy shale/silty sandstone with some conglomerate present. Marine and terrestrial

Stratigraphic Unit	Depth[1]	Description[2]
		depositional environment.
PERMIAN (298-255 Ma)		
Cutler Fm.	1,140	Fluvial arkose and arkosic conglomerate, with some sandy shales; deposited in alluvial fans.
PENNSYLVANIAN (322-298 Ma)		
Hermosa Group – Honaker Trail Fm.:		
Upper Honaker Trail	8,313	Limestone/sandstone/siltstone; deposited in marine conditions.
La Sal	12,006	Limestone/dolomite; some silty limestone, oolitic limestone, and algal limestone present.
Lower Honaker Trail	12,082	Limestone/sandstone/siltstone; deposited in marine conditions.
Hermosa Group – Paradox Fm.:	12,350	Resulted from intermittently closed marine environment.
Ismay	12,839	Limestone, stacked algal carbonate mounds and other shallow-water carbonates and dolomites.
1st Main Salt	13,104	Dolomite/salt; intermittently closed marine environment.
2nd Main Salt	13,497	Salt/anhydrite/shale; intermittently closed marine environment.
Base Salt – Lower Paradox	13,566	Shale/anhydrite/(minor) limestone; intermittently closed marine depositional environment.
Hermosa Group – Pinkerton Trail Fm.	13,693	Shales/anhydrites/siltstone/(minor) limestones; dark colored shales, limestone formed by marine invasion.
Molas Fm.	13,944	Shale/siltstone/claystone; regolith/soil (*terra rosa*) de-veloped on the karst surface of the Leadville formation after a period of extensive weathering and erosion.
MISSISSIPPIAN (355-322 Ma)		
Leadville Fm.	13,984	Limestone/dolomite. Lower unit (Kinderhookian-age) stromatolitic dolomite, lime mudstones, pelletal lime mudstones; deposited in intertidal to subtidal environments. Upper unit (Osagean-age) fossiliferous pelletal and oolitic limestone, and lime and dolomitic mudstone.
DEVONIAN (416-355 Ma)		
Ouray Fm.	14,400	Limestone—lime mudstone, pelletal lime mudstone and skeletal limestone that is locally dolomitized; formed in quiet-water marine environment.
Elbert Fm.	14,440	Sandstone/shales/shaly dolomites.
McCracken Fm.	14,607	Sandstone with occasional interbeds of sandy dolomite; transgressive depositional environment.
Aneth Fm.	14,681	Dolomite/shale; dense, argillaceous sequence.
CAMBRIAN (540-488 Ma)		
Lynch Fm.:		
Upper Lynch Shale	14,763	Sandstone/interbedded shale, dolomite, limestone.
Lynch Limestone	14,835	Limestone.
Lower Lynch Shale	14,928	Shale.

Stratigraphic Unit	Depth[1]	Description[2]
Muav Fm.	14,988	Limestone.
Bright Angel Fm.	15,103	Shale.
Ignacio Fm.	15,246	Sandstone, sometimes referred to as quartzite; transgressive depositional environment.
PRECAMBRIAN (>540 Ma)		
Precambrian	15,446	Described regionally as granitic rock with well-developed northwest and northeast orthogonal fracture systems; identified in PVU Injection Well #1 as moderately metamorphosed diorite-gabbro schist.

[1]Depths are taken from the geologic drill log of PVU Injection Well #1 by Harr (1988). Depths are relative to the ground surface elevation (4996 ft) and have been corrected for borehole deviation.
[2]Descriptions are taken from: Bremkamp and Harr (1988), Campbell (1981), Doelling (1988), Williams (1964), and Nuccio and Condon (1996).
[3]Ages from Walker and Geissman (2009)

The Mississippian Leadville formation is the primary target reservoir for PVU brine injection, due to its sedimentary and structural characteristics. The Leadville formation consists of limestone and dolomite layers that are fractured, faulted, and contain karst features. The lower Leadville formation (Kinderhookian-age) is stromatilitic dolomite, lime mudstones, and pelletal lime mudstone deposited in intertidal to subtidal environments. The upper Leadville formation (Osagean age) contains fossiliferous pelletal and oolitic limestone, and lime and dolomitic mudstone (Doelling et al., 1988). The upper Leadville underwent uplift and erosion after deposition, resulting in karst-type weathering and the formation of a *terra rossa* type regolith on the surface. *Terra rossa* is a red clay soil that forms on the surface of limestone bedrock. Under oxidizing conditions, iron oxide forms in the clay, giving the soil a red-orange color. This karstic portion of the Leadville is not considered a potential reservoir due to the concentration of fines infilling the karst features (Bremkamp et al., 1984).

3 Geologic models developed in the 1980s

Prior to the selection of the site for the current PVU injection well, geophysical interpretations were performed for Reclamation by two groups of consultants using deep seismic reflection and well log data: Katz and Carroll (1984), and Bremkamp and others (1984). The study area was located southwest of central Paradox Valley, where the Dolores River enters the valley. These investigations utilized 15 single-fold seismic reflection lines recorded in 1961 by Empire Geophysical, and three 12-fold seismic lines recorded in 1982 by Seisport Exploration (Figure 3-1). In both data vintages, the quality decreases greatly in thick salt sections. Data quality also decreases in areas overlain by unconsolidated material such as in valley bottoms. Logs from nine wells were used as control points for formation depth and velocity (Figure 3-1). Only six of the wells, however, penetrated the Paradox salt member and Leadville formation.

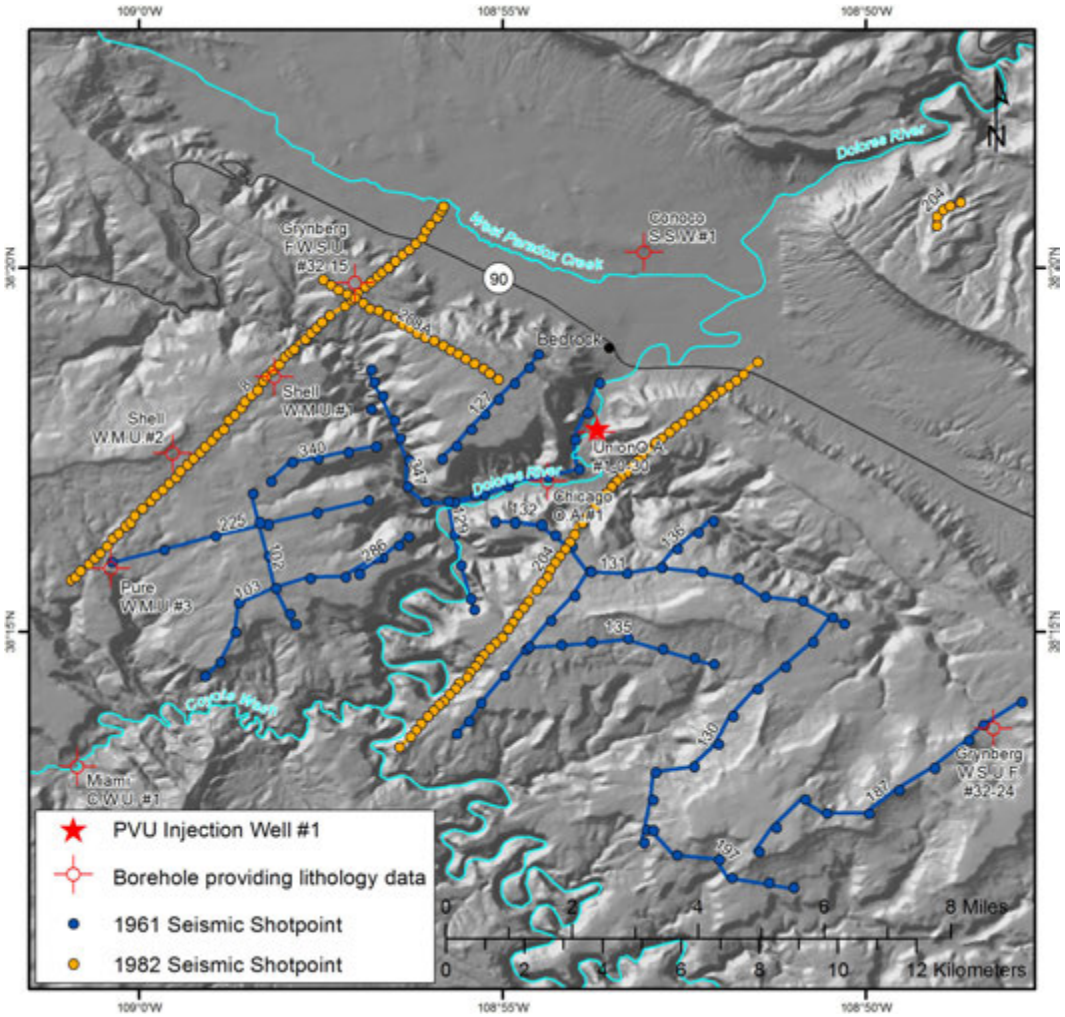

Figure 3-1. Seismic reflection lines and wells used to create the geologic models used in siting PVU Injection Well #1.

Both sets of investigators created contour maps of the tops of the Cutler formation, Paradox salt member, and Leadville formation, as well as the thicknesses of the Paradox salt member and Leadville formation. The contour maps of the Leadville formation are shown in Figure 3-2. There are significant differences between the two sets of models, as described in Block and others (2012) and King and others (2014), suggesting that the data were of marginal quality.

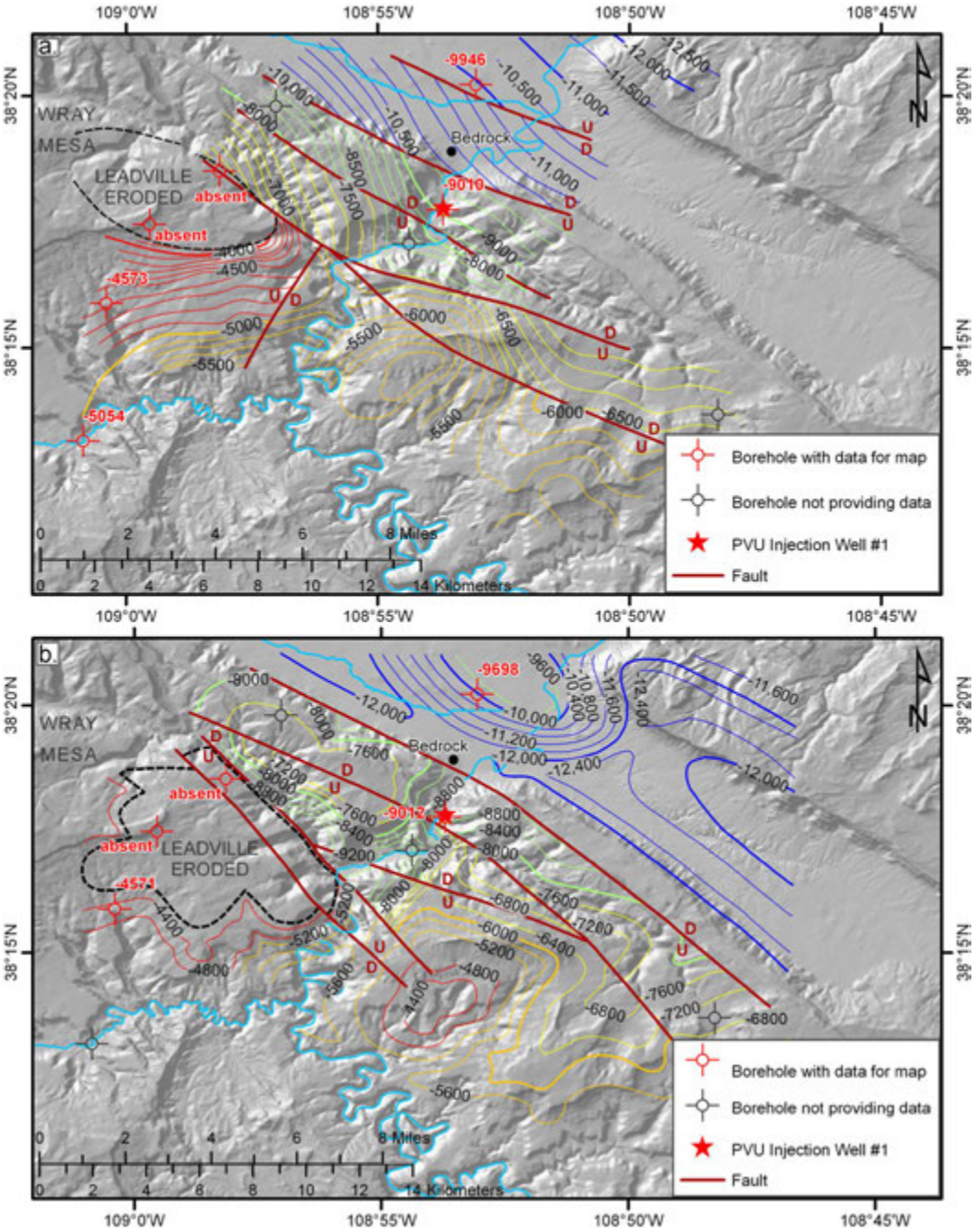

Figure 3-2. Structural contour maps of the top of the Leadville formation. Contour values are elevations in feet relative to sea level. Contour interval is variable. U and D labels indicate the upthrown and downthrown sides of the faults, respectively. Two interpretations are shown, from Bremkamp and others (1984) (top) and Katz and Carroll (1984) (bottom). Red labels indicate the elevation of the Leadville formation in the corresponding borehole.

A geologic model covering a larger area was later created (Bremkamp and Harr, 1988). This model focused on the depth to the Leadville formation (Figure 3-3). The model used no additional seismic reflection data, and the available well log data were relatively sparse, thus the uncertainty in this model is presumably large.

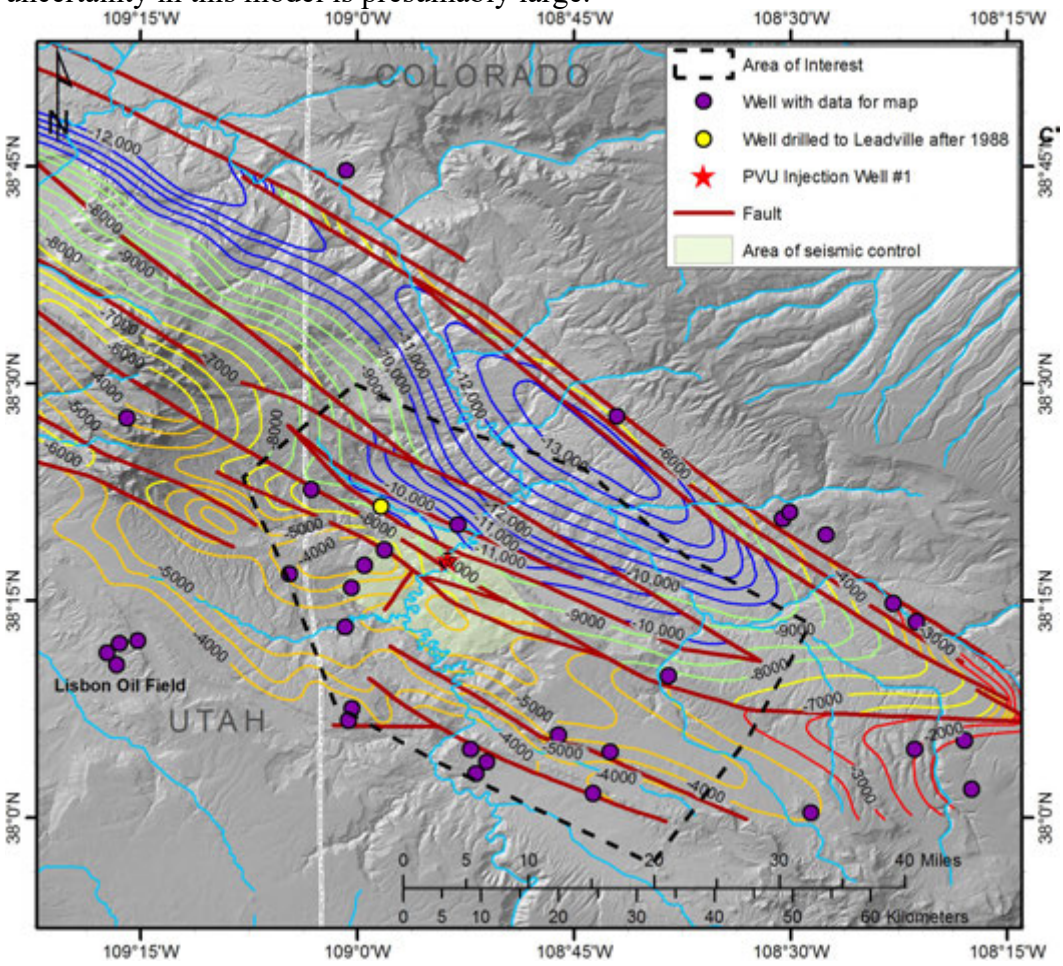

Figure 3-3. Strutural contour map of the top of the Leadville formation, from Bremkamp and Harr (1988). Contour values are elevations in feet relative to sea level. Contour interval is 500 feet. Purple circles represent all wells that were drilled prior to 1988 and were deep enough to reach the Leadville formation; it is not known whether Bremkamp and Harr had access to data from all of these wells. The area of interest for the current study is shown for reference.

Since the time these studies were conducted in the 1980s, only one additional well has been drilled to the depth of the Leadville formation in the area (Figure 3-3), and only a few additional seismic reflection surveys have been shot. However, the investigators in the 1980s used only a small fraction of the available seismic reflection lines that had been acquired to that point. Additionally, seismic reflection data processing and interpretation techniques have improved significantly in the last 30 years. Combined with the new data types incorporated into our model, the increased quantity and quality of data available to us today should allow us to create a geologic model with substantially less uncertainty than the models developed for siting PVU Injection Well #1.

4 Data Sources

Seven different major types of data were used in the integrated geologic model. These include seismic reflection data (Section 4.1), well log data (Section 4.2), aeromagnetic and gravity data (Section 4.3), earthquake hypocenter data (Section 4.4), data on the deep stress field (Section 4.5), and InSAR data (Section 4.6). Various studies were undertaken analyzing and interpreting these datasets. Most of the studies are described elsewhere in more detail. Here we summarize the datasets and the interpretations that were derived from them.

4.1 Seismic reflection data

4.1.1 Method

Seismic reflection is a geophysical technique commonly used in the oil and gas industry. In this technique, a source is used to generate seismic waves. The most common sources for deep surveys are dynamite or Vibroseis. Each time the wave reaches an interface between two layers with differing acoustic impedances, a portion of the wave is reflected back. The reflected waves are measured by an array of geophones, and the travel times to each geophone can be used to build an image of the subsurface. Seismic reflection images have higher resolution than most other geophysical techniques, but they require skilled processing and interpretation in order to produce a meaningful subsurface model, and, as with all geophysical methods, that model is non-unique.

4.1.2 Data

For this project, Reclamation licensed all or part of 39 existing 2D seismic reflection lines from Seismic Exchange International, totaling approximately 580 miles. These lines were acquired in the 1970s and 1980s and include both dynamite and Vibroseis sources. They are depicted in Figure 4-1 and described in Table 4-1.

The seismic reflection lines were processed by Excel Geophysical Services, using standard processing techniques, including pre-stack time migration. A description of processing steps and parameters is given in a separate report (Excel Geophysical Services, 2016). The licensing, processing, and interpretation were completed in three phases. Phase I included approximately 80 miles of seismic reflection lines, while Phase II added an additional 500 miles of seismic reflection lines (Figure 4-1). Phase III involved comparing the major features from the seismic reflection and aeromagnetic interpretations, comparing the earthquake hypocenter data with the seismic reflection interpretation in order to refine the interpretation in select areas, particularly near PVU Injection Well #1, and creating detailed cross sections of twelve sites that were being considered for potential injection wells at that time. The details of the comparison between earthquakes and seismic reflection data are discussed in Section 5.1.1, but the Leadville structure map (Figure 4-6) and Paradox-to-Leadville isochore map (Figure 4-7) contain modifications resulting from this comparison. All of the Phase I lines were included in the Phase II and III seismic reflection interpretations, and thus only the Phase II and III interpretations are included in the integrated model.

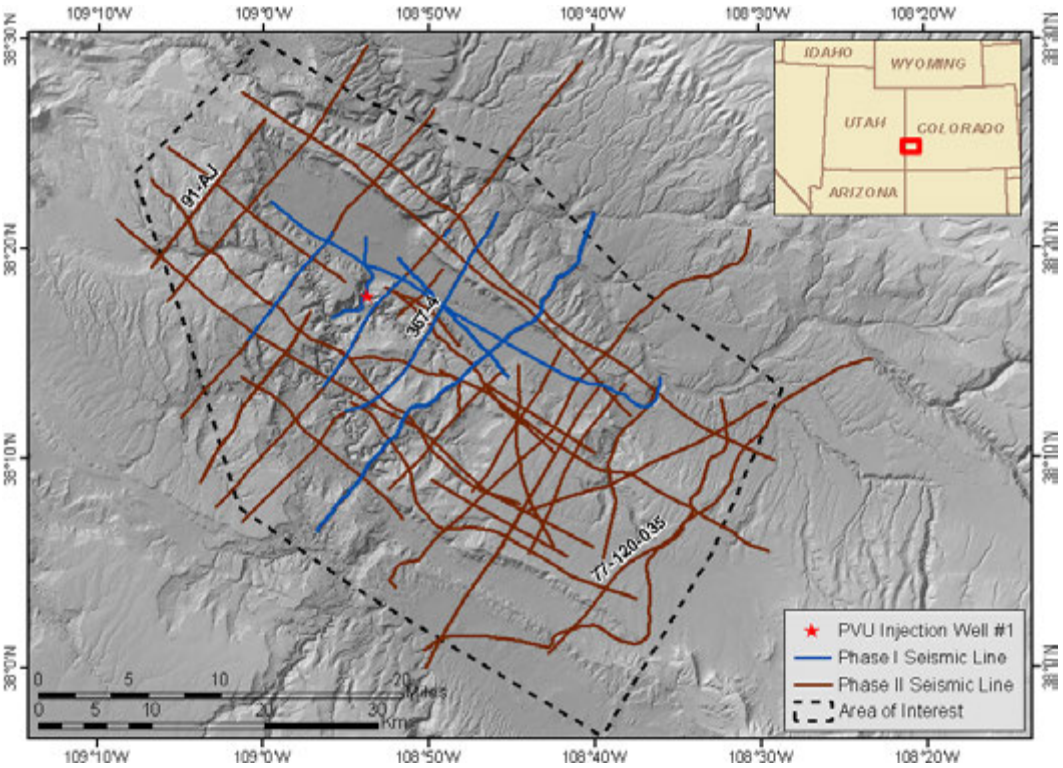

Figure 4-1. Locations of seismic reflection lines. Lines shown in Figure 4-2, Figure 4-3, and Figure 4-4 are labeled.

Table 4-1. Seismic reflection lines.

Dataset	Line ID	Shot Date	Listed Energy Source	Shotpoint Range Licensed	Approximate Line Length Licensed (Miles)
Chevron	367-10	1984	DYNAMITE	2857 - 3243 (entire line)	12.1
Chevron	367-4	1982	VIBROSEIS	965-1310 (entire line)	14.2
Chevron	367-6	1984	DYNAMITE	1511 - 1867 (entire line)	11.2
Chevron	367-7	1984	DYNAMITE	1884 - 2208 (entire line)	10.2
Chevron	72-687	1974	DYNAMITE	110 - 290 (entire line)	11.3
Chevron	72-689	1974	DYNAMITE	113 - 256 (entire line)	9.0
Chevron	72-690	1974	DYNAMITE	110 - 315 (entire line)	12.9
Chevron	91-AJ	1984	DYNAMITE	5855 - 6189 (entire line)	10.5
Shell	77-120-028	1977	PRIMACORD	550 - 2107 (entire line)	29.5
Shell	77-120-030	1977	DYNAMITE	576 - 1055 (entire line)	9.1

Dataset	Line ID	Shot Date	Listed Energy Source	Shotpoint Range Licensed	Approximate Line Length Licensed (Miles)
Shell	77-120-035	1977	DYNAMITE	635 - 1360 (entire line)	13.8
Shell	77-120-038	1977	VIBROSEIS	457 - 1014 (entire line)	10.6
Shell	77-120-26	1977	DYNAMITE	900 - 2152 (SE end)	23.7
Shell	78-120-002	1969	DYNAMITE	553 - 1148 (entire line)	11.3
Shell	78-120-021	1978	DYNAMITE	595 - 839; 888 - 1346 (available line)	10.0
Shell	78-120-022	1978	Unknown	601 - 1631 (entire line)	19.5
Shell	78-264-002	1978	DYNAMITE	601 - 1895	24.5
Shell	79-120-043	1979	DYNAMITE	576 - 920 (entire line)	6.5
Shell	79-120-045	1979	DYNAMITE	600 - 1061 (entire line)	8.8
Shell	79-120-049	1979	DYNAMITE	600 - 1279 (entire line)	12.9
Shell	79-120-051	1979	DYNAMITE	600 - 2117 (entire line)	28.8
Shell	79-466-004	1979	VIBROSEIS	232 - 1134 (entire line)	24.2
Shell	80-120-073	1980	DYNAMITE	600 - 1172 (entire line)	10.9
Shell	80-120-075	1980	DYNAMITE	552 - 989 (entire line)	8.3
Shell	80-120-077	1980	Unknown	603 - 1048 (entire line)	8.4
Shell	80-266-115	1980	VIBROSEIS	631-1094 (entire line)	8.8
Shell	80-266-116	1980	DYNAMITE	600 - 1142 (entire line)	10.3
Shell	81-468-108	1981	DYNAMITE	200 - 977 (entire line)	14.7
Target Geophysical	TAR-PARADOX-204	1982	DYNAMITE	1150 - 2209	33.1
Target Geophysical	TAR-PARADOX-208A	1982	DYNAMITE	1300 - 1692	12.3
Target Geophysical	TAR-PARADOX-209B	1982	DYNAMITE	2203 - 2828 (entire line)	19.6
Target Geophysical	TAR-PARADOX-211	1982	DYNAMITE	1040 - 2113	33.6
Target Geophysical	TAR-PARADOX-7	1982	DYNAMITE	1400 - 2000	18.8

Target Geophysical	TAR-PARADOX-8	1984	DYNAMITE	1300- 2050	23.4
Target Geophysical	TAR-PARADOX-9	1981	DYNAMITE	1900 - 2229	10.3
Texaco	6634-211A	1974	VIBROSEIS	2 - 463 (entire line)	28.9
Texaco	6634-213E	1985	VIBROSEIS	1-107 (entire line)	5.9
Unocal	UNO-NYSMESA-2	1970	DYNAMITE	1 – 87 (entire line)	5.4
Unocal	UNO-NYSMESA-3	1970	DYNAMITE	1 – 53 (entire line)	3.3

4.1.3 Results

Structural interpretations were provided for all of the 39 seismic reflection lines and are included as attachments to Arestad (2016), with some lines modified in Arestad (2017); only a few interpreted lines are reproduced here to provide examples of the level of structural complexity in the area (Figure 4-2, Figure 4-3, and Figure 4-4).

Figure 4-2 is not publicly available because it contains proprietary data from private sources.

Figure 4-2. Interpreted line 367-4 from southwest to northeast, which shows major structural and salt features across the project area. Figure taken from Arestad (2016).

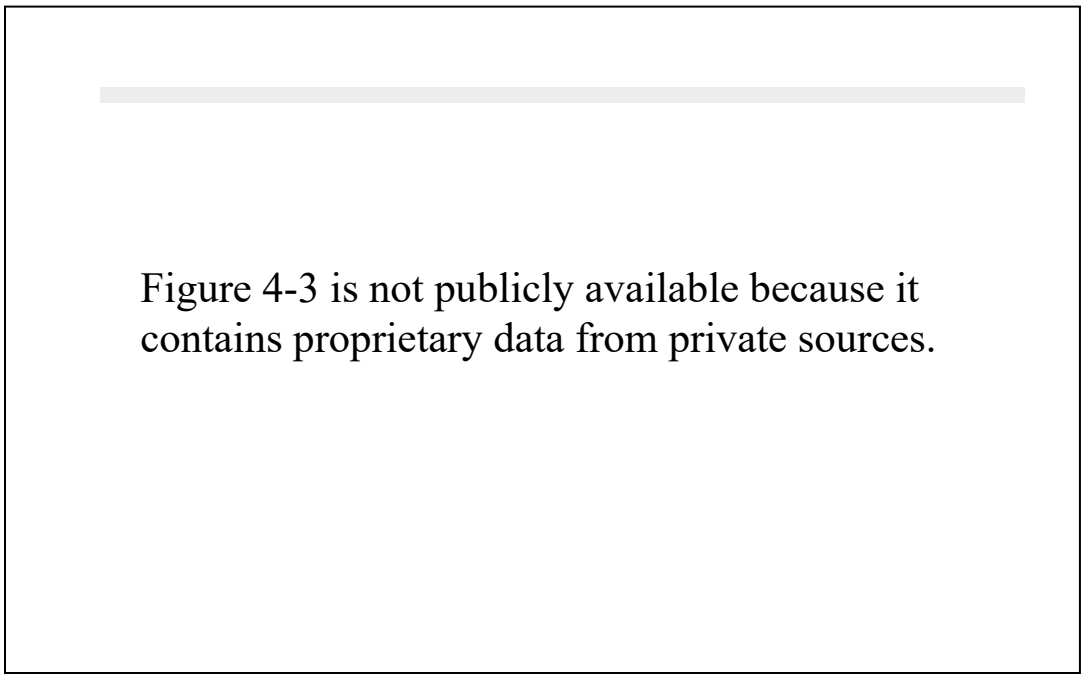

Figure 4-3. Interpreted line 91-AJ in the northwestern part of the study area. Figure taken from Arestad (2016).

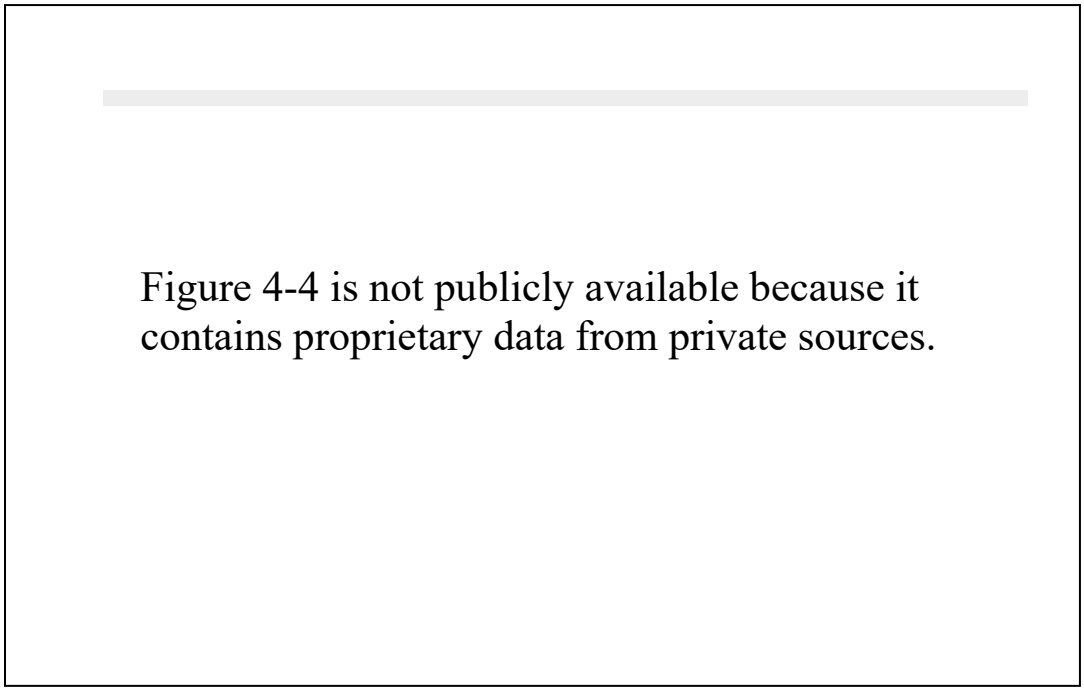

Figure 4-4. Interpreted line 77-120-035 across Big Gypsum Valley salt diapir and salt pillows as well as Andy's Mesa Field. Figure taken from Arestad (2016).

The tops of the Paradox salt and Leadville formation were converted from time to depth and contoured to produce structural maps of these units (Figure 4-5; Figure 4-6). An isochore map was also produced showing the thickness from the top of the Paradox salt to the top of the Leadville formation (Figure 4-7). The structural map of the Leadville formation was used to

identify fault segments with vertical offsets of at least 500 feet, which we assumed to be impermeable for the purposes of geomechanical modeling (Section 5.2).

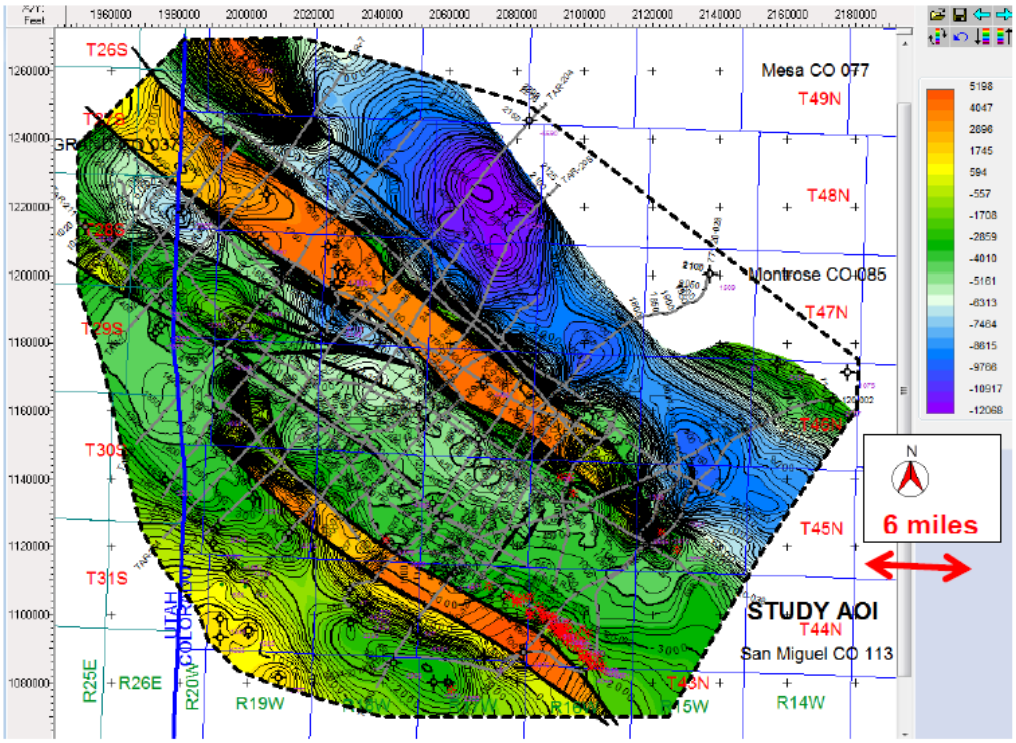

Figure 4-5. Structure map of top of Paradox salt (elevation in feet). Figure taken from Arestad (2016).

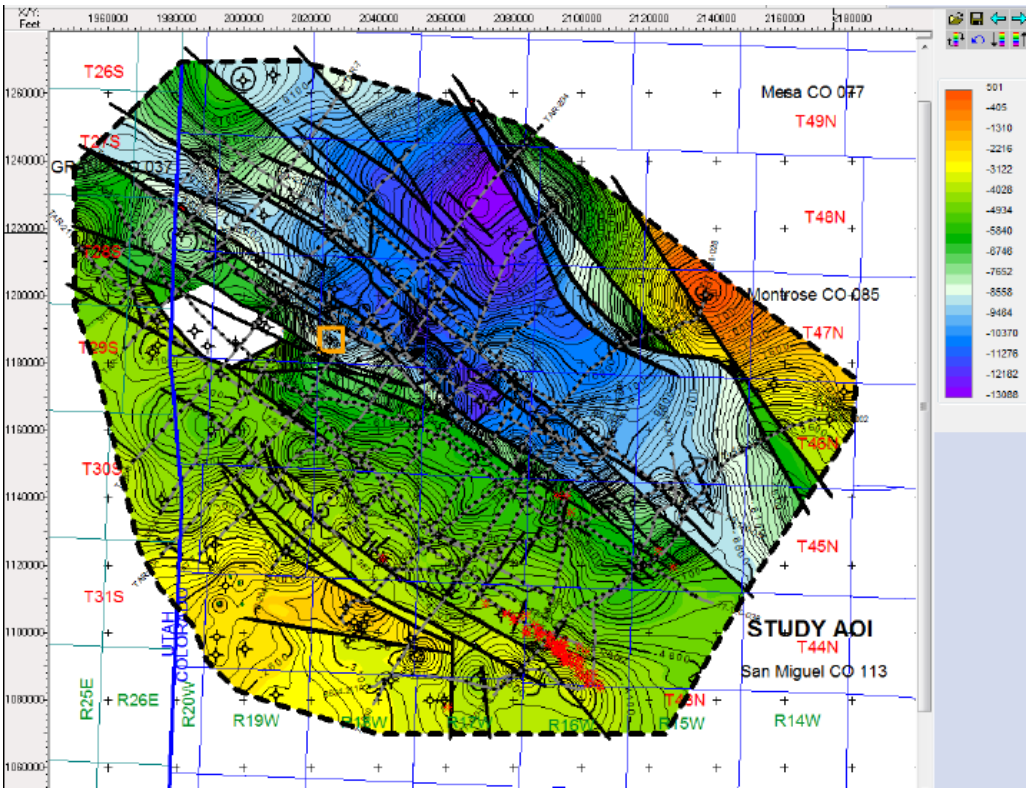

Figure 4-6. Structure map of top of Leadville formation (elevation in feet). Note area of missing Leadville in the Wray Mesa area. Figure taken from Arestad (2017).

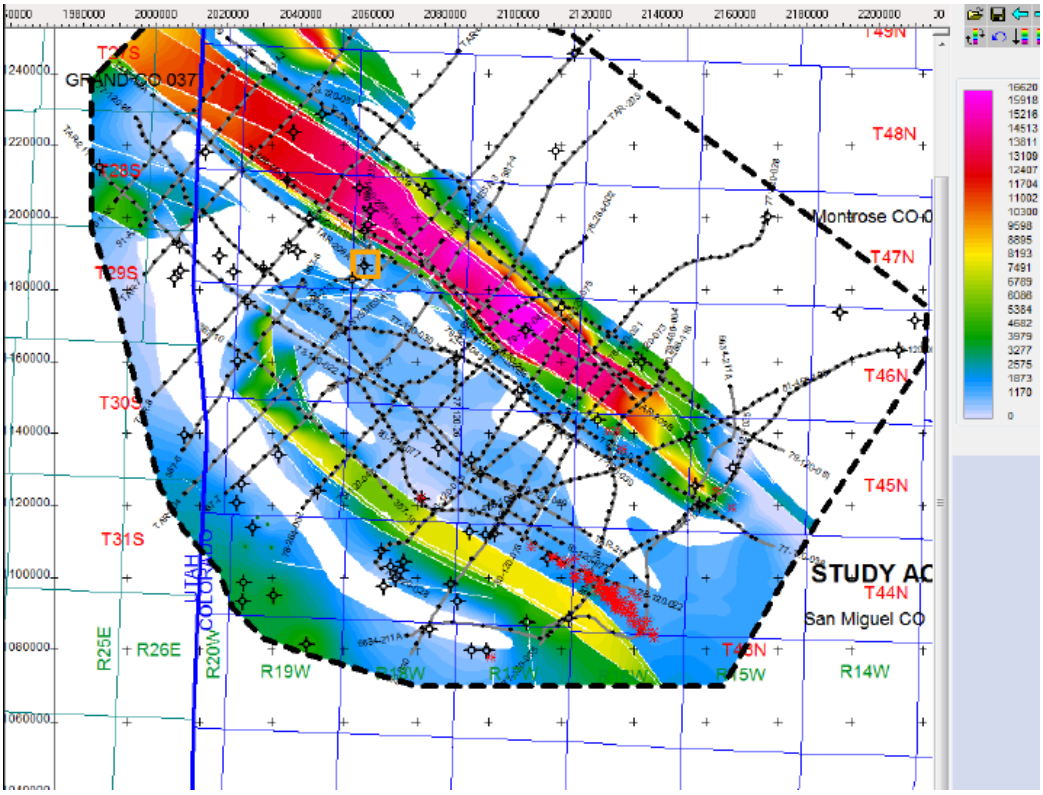

Figure 4-7. Isochore map of top of Paradox salt to Leadville formation (feet). Figure taken from Arestad (2017).

Note the large variations in salt thickness in the interpreted lines shown in Figure 4-2 through Figure 4-4 and in the isochore map in Figure 4-7. The salt thickness ranges from 0 or nearly 0 (thinner than the resolution of the seismic reflection data) to more than 14,000' thick. Salt thickness is a significant factor in siting a second injection well, with both very thin and very thick salt being undesirable, so a map showing salt pillows/diapirs (very thick areas of salt) and salt welds (very thin areas of salt) was also created (Figure 4-8).

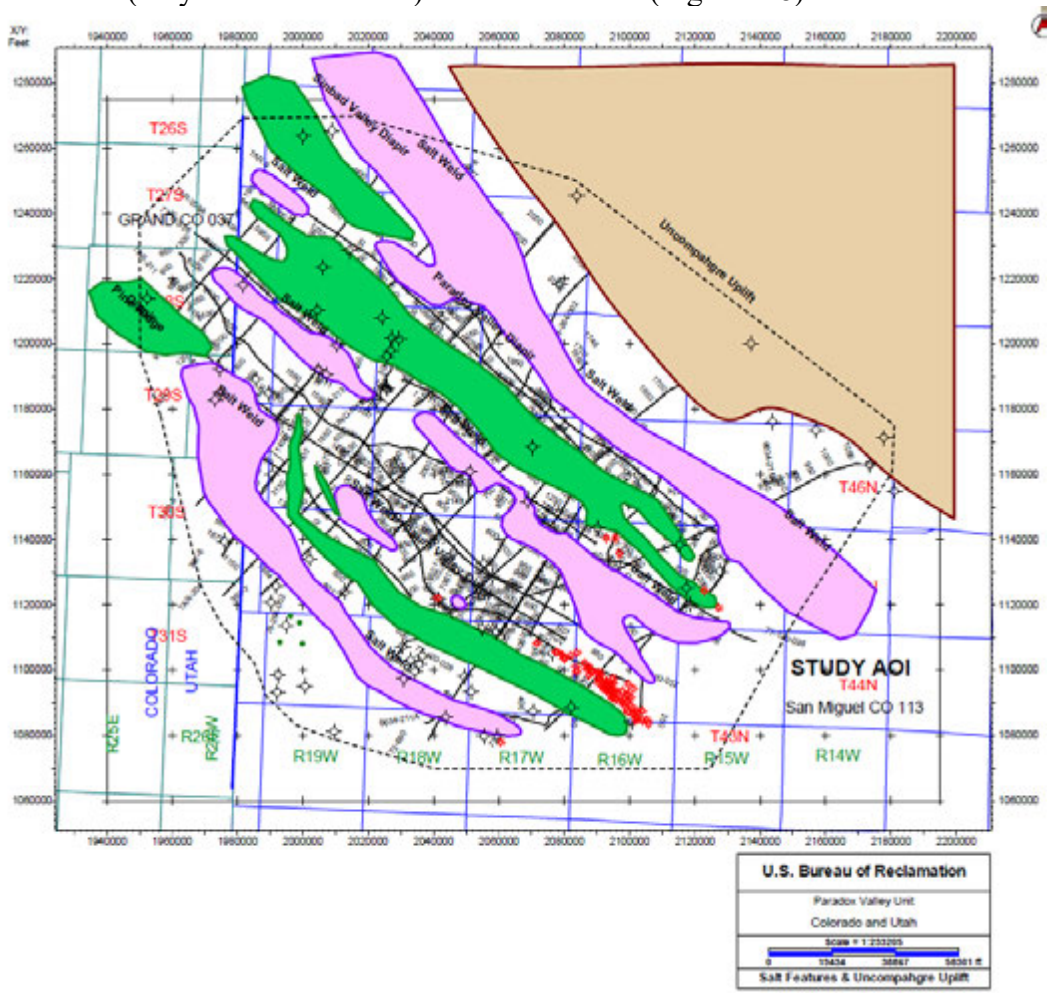

Figure 4-8. Salt diapirs (green) and salt welds (pink). Brown polygon shows the location of the Uncompahgre uplift. Figure taken from Arestad (2016).

4.2 Well log data

4.2.1 Method

Analysis of well log data has two primary purposes. The first purpose is to aid in the interpretation of seismic reflection data. When interpreting seismic reflection data, it is often impossible to tie seismic reflectors to the geologic layers they represent without auxiliary information. If one or more wells are situated directly on a seismic reflection line, sonic logs acquired in those wells can be used, in conjunction with the interpreted formation tops, to tie seismic reflectors to specific formation interfaces. Otherwise, it is necessary to either project a

well onto the seismic reflection line, reducing accuracy, or tie the seismic reflectors to those on an intersecting line, which is prone to errors.

The second purpose of well log data analysis is to provide information about the properties of the formation(s) of interest, which is generally not available through any other method. One important characteristic in siting an injection well is the porosity of the injection target formation. The porosity can be measured by a neutron porosity tool, or it can be calculated from sonic or density logs. While calculating the porosity from sonic or density logs is less accurate than using a neutron porosity tool, these logs tend to be more readily available.

4.2.2 Data

Digital well logs were obtained from 90 oil and gas wells in the area. These wells are described in detail in a separate report (King, 2017). While sonic logs were of primary interest, other types of logs were also acquired, including gamma ray and density logs. Digital logs from 43 wells were purchased from IHS Energy Lognet. Digital logs were obtained from the Colorado Oil and Gas Conservation Commission (COGCC) database for three wells. For the remaining 44 wells, we obtained free raster images from the databases maintained by the Colorado Oil and Gas Conservation Commission (COGCC) and Utah Division of Oil, Gas, and Mining (UTDOGM), and had the rasters digitized by LogDigi. These wells were divided into Phase I and Phase II, in accordance with the phases of seismic reflection interpretation, with 41 wells in Phase I and 49 wells in Phase II (Figure 4-9).

The majority of the well logs from the PVU Injection Well #1 existed only in one or two hardcopies, so these logs were also scanned and digitized.

Formation tops were obtained for these wells from five different sources. The sources include the databases maintained by the COGCC and UTDOGM, an internal government report (Harr, 1988), a database of formation tops purchased from Don Rasmussen of Paradox Basin Data, and formation tops obtained from well log correlation by the seismic interpreter on this project, John Arestad of International Reservoir Technologies (IRT), and David List, a structural geologist who consulted for IRT on this project.

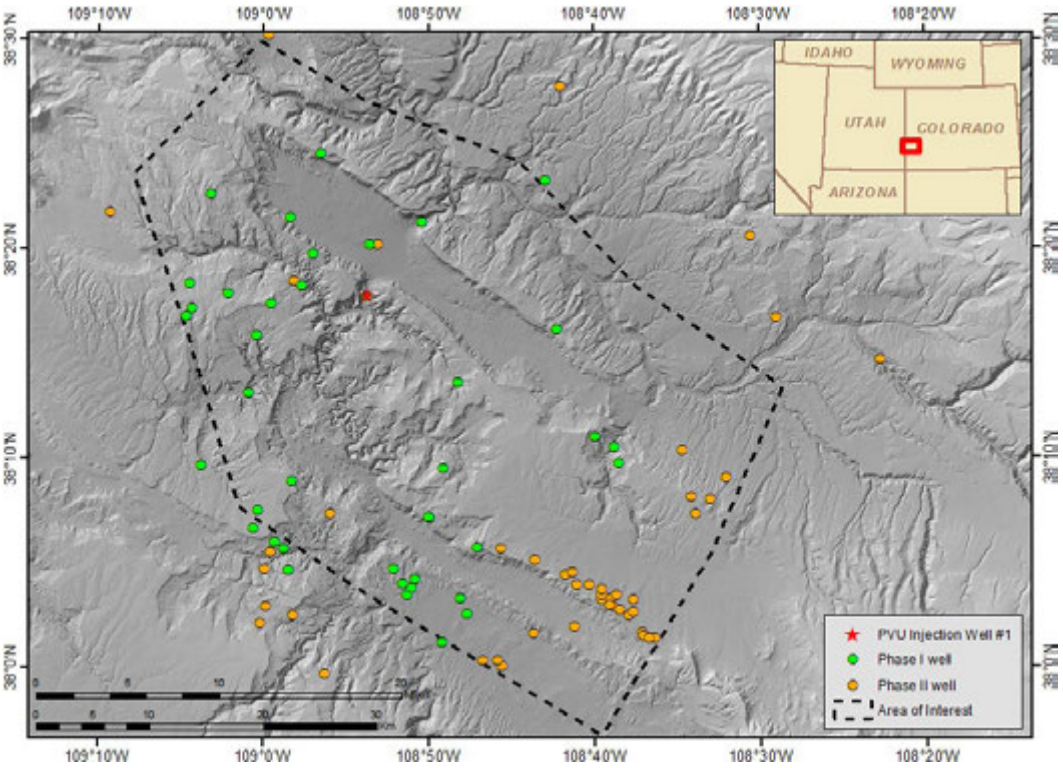

Figure 4-9. Locations of oil and gas wells for which well logs were obtained.

4.2.3 Results

In addition to supporting the seismic reflection interpretation discussed in Section 4.1, several additional products were also derived from the well log data. An advantage to the well log data is that pure salt can be distinguished from salt that is interfingered with siliciclastics, which is discussed in Section 5.3.1.2. Figure 4-10 shows the salt isochore map from Figure 4-7, annotated to show the location where the pure salt transitions into a siliciclastic wedge.

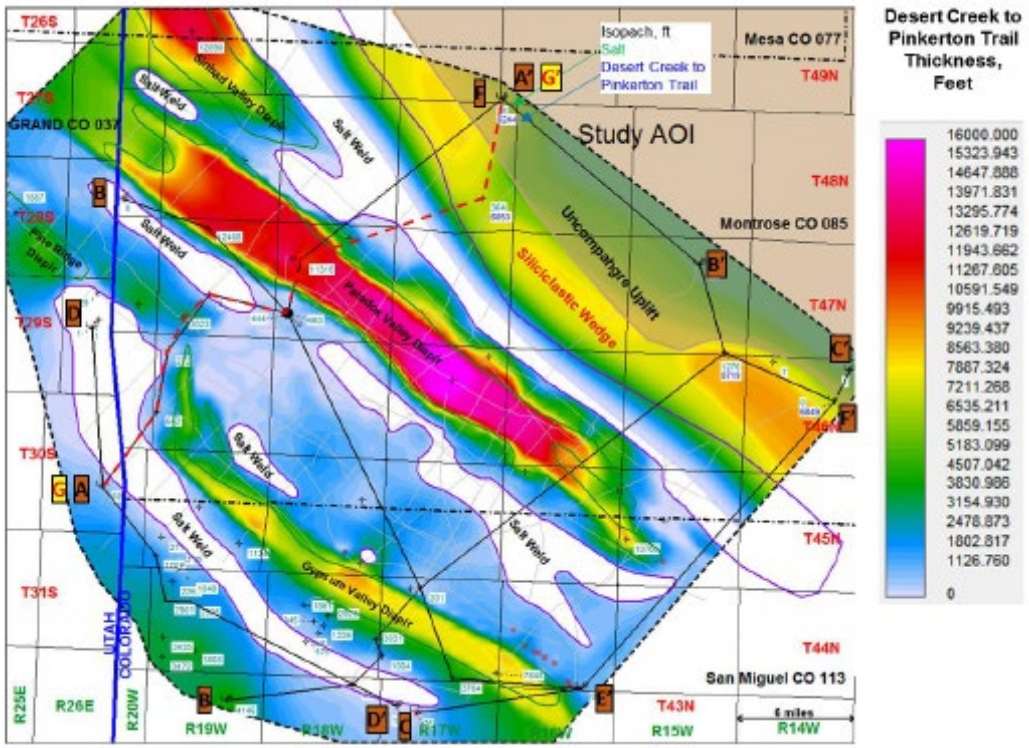

Figure 4-10. Combined isopach of Desert Creek, Akah, and Barker Creek members of the Paradox formation. Figure taken from List (2016).

The tops of the Leadville formation and underlying Ouray formation were used to create a Leadville isopach map (Figure 4-11). As the Ouray formation typically cannot be identified on the seismic reflection data, this provides additional information that supplements the seismic reflection interpretation.

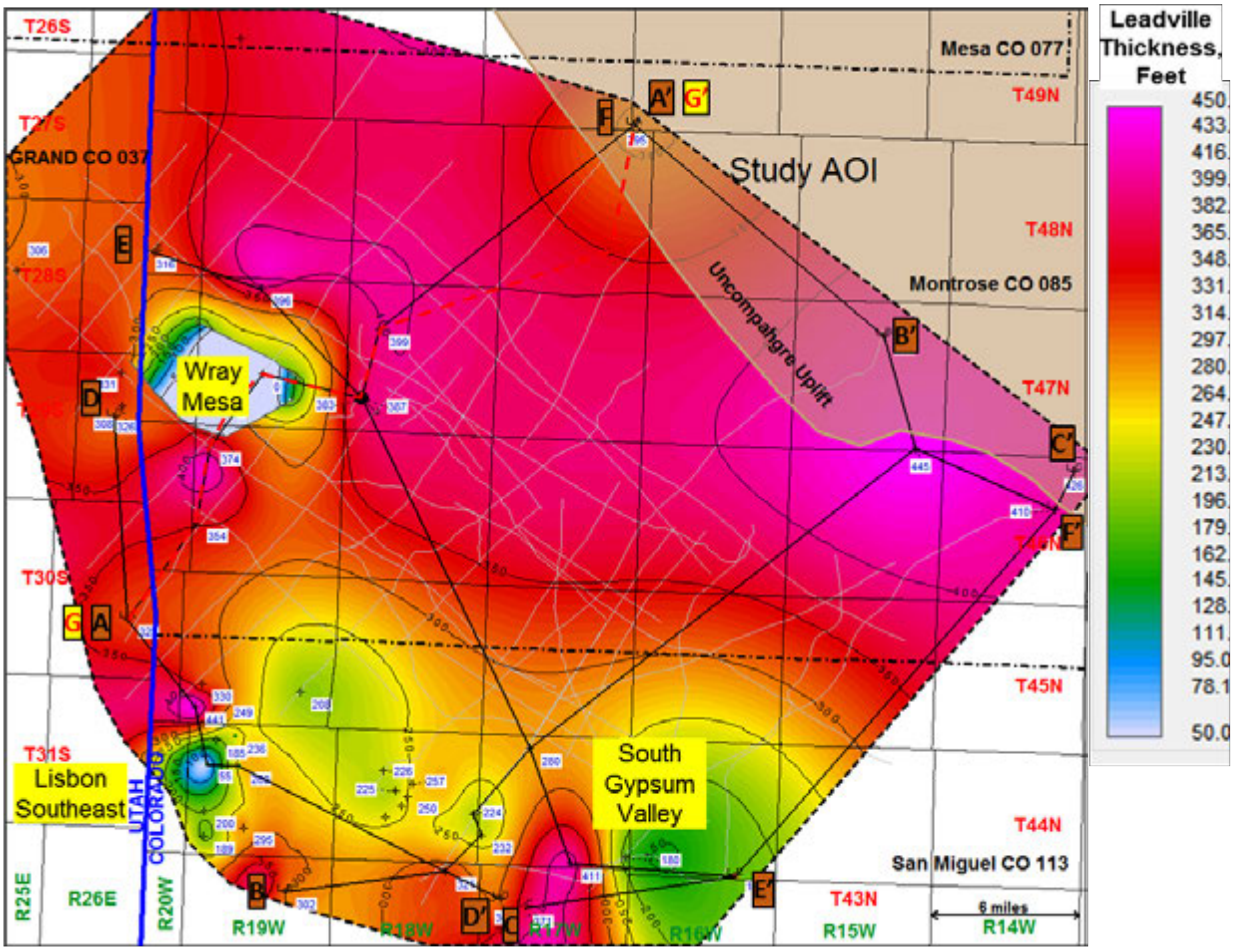

Figure 4-11. Leadville Limestone isopach derived from well control showing two major areas of significant erosion. It is completely eroded on the Wray Mesa structure and only 55' remains on the crest of the Lisbon southeast structure. Figure taken from List (2016).

Drill stem tests in the Leadville formation were used to map a potentiometric surface (Figure 4-12), which can provide information about the direction of fluid flow and the locations of impermeable faults. However, due to the sparseness of the data, it is difficult to draw many definitive conclusions from this map. The regional trend is consistent with fluid recharge being along the west flank of the San Juan Mountains and the west flank of the Uncompahgre uplift. The 1052’ potentiometric difference calculated between the two wells in T47N R15W may indicate the faults along the leading edge of the Uncompahgre uplift may be at least partially sealing. The relatively high potentiometric surface in T44N R18W as compared to the regional trend may indicate an area of increased permeability within the Leadville toward the northeast. The distribution of tight and permeable tests indicates that reservoir development is heterogeneous and needs further study (List, 2016).

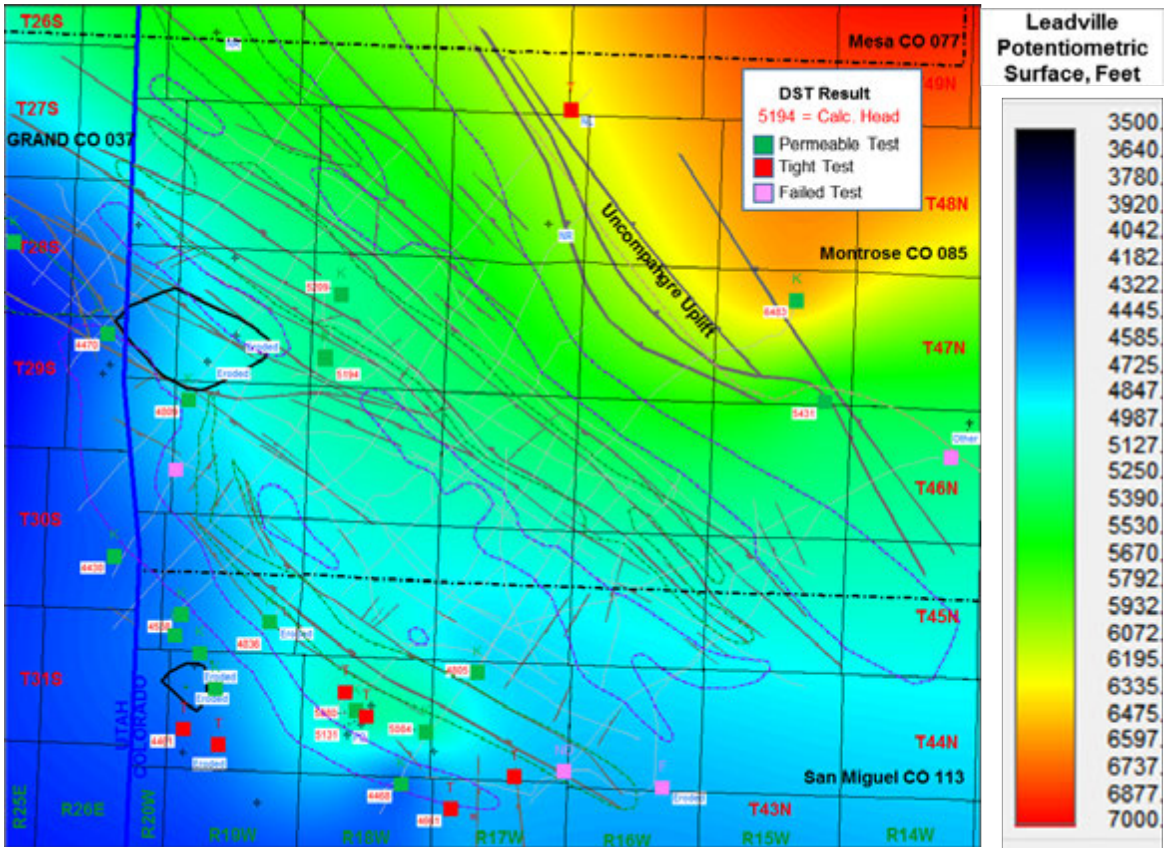

Figure 4-12. Leadville limestone potentiometric surface displayed with faults interpreted from 2D seismic reflection. Fluid flow would be from northeast to southwest. The large gradient observed between the two wells in T47N R15W may indicate a partially sealing fault exists between them. The distribution of tight and permeable DST tests indicates the sporadic nature of reservoir development. Faults were provided by Arestad (2016). Figure taken from List (2016).

Additionally, porosities of the Leadville formation were calculated for all well logs that had sonic logs extending at least to the base of the Leadville formation (King, 2017). A map of the average porosity is shown in Figure 4-13. This map shows that the porosity is highly variable and shows no obvious spatial correlation. However, the results are somewhat promising for the purposes of siting a second injection well, as the majority of wells have average porosity values higher than that found in PVU Injection Well #1.

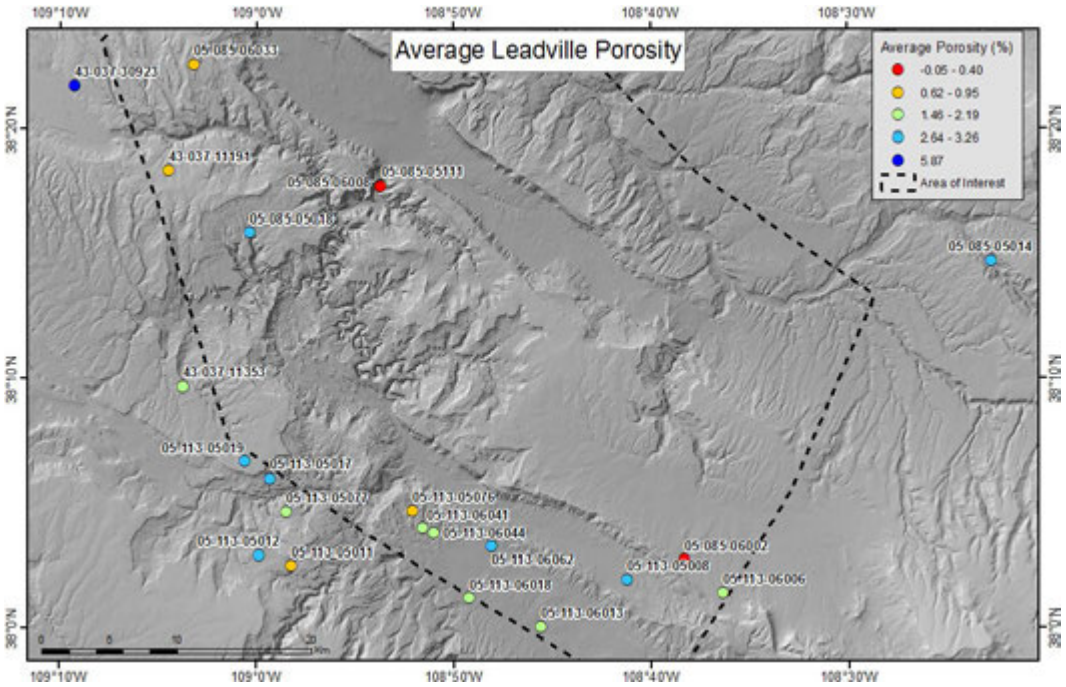

Figure 4-13. Average porosity of Leadville formation, calculated from sonic logs. A negative porosity was calculated in one well, indicating that the average measured velocity is faster than the average assumed matrix velocity.

4.3 Aeromagnetic and gravity data

4.3.1 Method

Magnetic surveying is a geophysical method in which the total magnetic intensity is measured by a magnetometer. The International Geomagnetic Reference Field (IGRF) and other corrections are then subtracted from the total magnetic intensity. The IGRF is a mathematical model of the expected value of the magnetic intensity at a given time and location, based on fitting all observed data from approved sources. Once the expected value is removed and other corrections are made, the remaining signal, referred to as a magnetic anomaly, represents the effect of the magnetization of the crustal geology (Reeves, 2005). Magnetic surveying is commonly performed using an aircraft (airplane, helicopter, or unmanned aerial vehicle), which is known as an aeromagnetic survey.

Gravity surveying is a geophysical method by which the acceleration due to gravity is measured by a gravimeter. After correcting for latitude (because the earth is not a perfect sphere), the height at which the gravity is measured, and the attraction of terrain, the remaining signal is known as the Bouguer anomaly. The Bouguer anomaly provides information about the density of subsurface materials, with low-density material producing a negative anomaly and high-density material producing a positive anomaly.

The interpretations of both gravity and magnetic data are non-unique, as an infinite number of combinations of the depth, size, and density or magnetic susceptibility of subsurface anomalies can produce identical gravity and magnetic anomalies. However, through careful interpretation and integration with other sources of data, gravity and magnetic data can provide important

constraints on the subsurface geology. For the purposes of this model, the most important constraints provided by these data are on the basement geology, which is difficult to image with the seismic reflection data.

4.3.2 Data

An aeromagnetic survey was flown by EDCON-PRJ from February 17 to March 5, 2016. The survey consisted of 149 survey lines on 400-meter spacings and oriented at a heading of 30° relative to true north, with 18 tie lines on 2000-meter spacings oriented at a heading of 120° relative to true north. The prescribed drape was 150 meters, which means that the airplane maintained an elevation of 150 meters above the ground surface whenever possible. In some cases the actual elevation was higher due to steep topography (EDCON-PRJ, 2016). The gridlines are shown in Figure 4-14. Note that a small portion of the AOI was not included in the aeromagnetic survey, as the AOI was expanded after the survey contract was awarded.

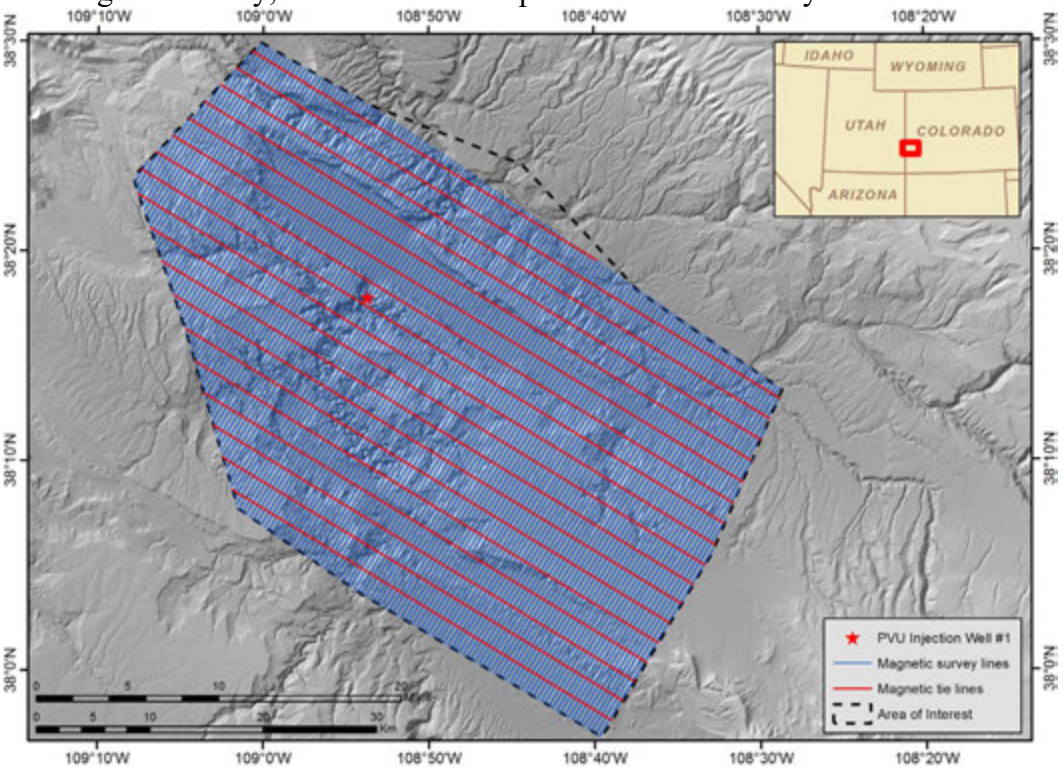

Figure 4-14. Magnetic grid. Survey lines are shown in blue and tie lines are shown in red.

New gravity data were not collected. However, the public domain gravity data were integrated into the interpretation of aeromagnetic data. These data are relatively sparse, but do show some of the major features in the AOI, such as negative anomalies associated with the low-density salt diapirs underlying Paradox Valley and Gypsum Valley (Wintermoon Geotechnologies, 2016). Figure 4-15 shows the Bouguer gravity anomaly and the locations of gravity stations.

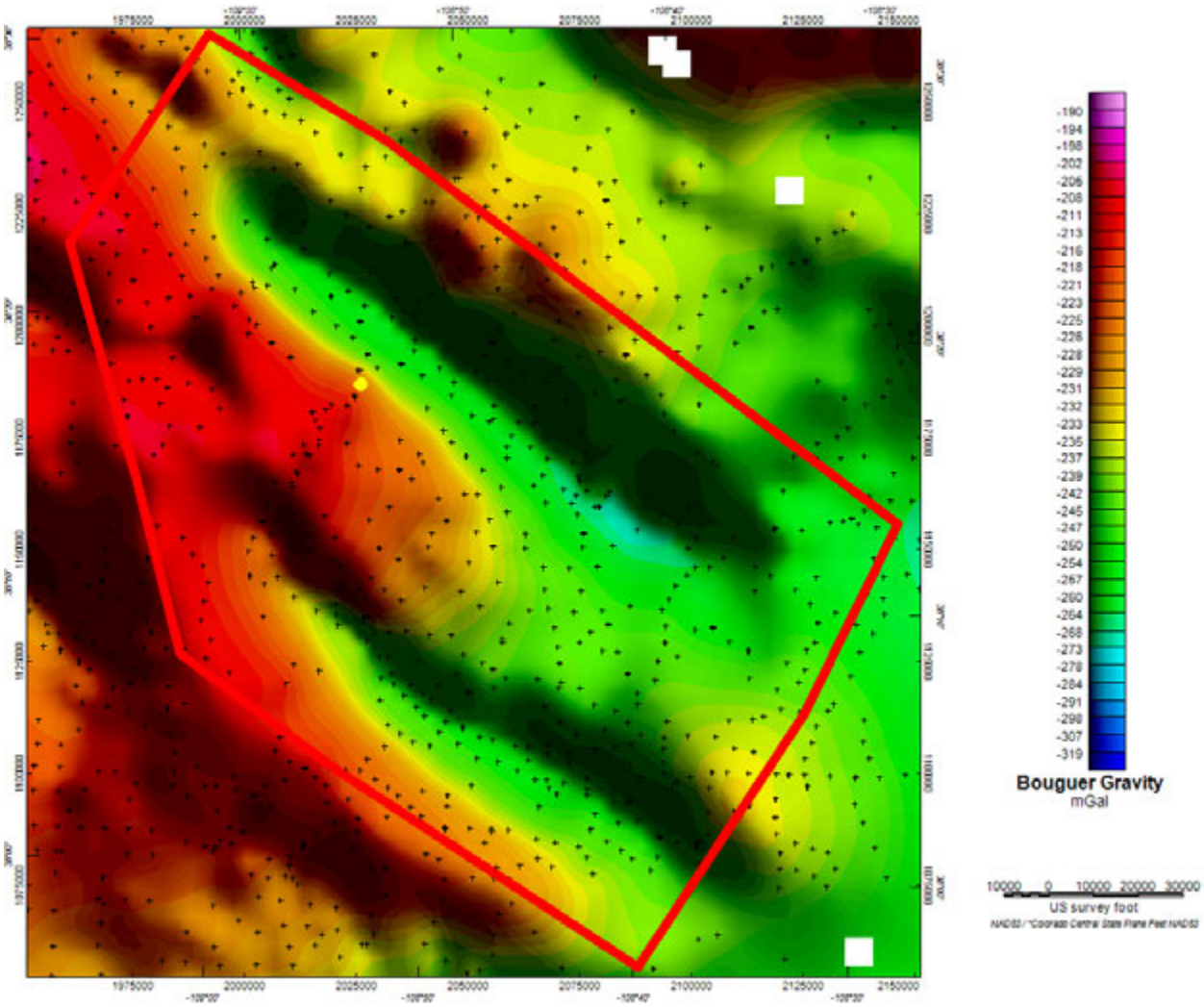

Figure 4-15. Public domain Bouguer gravity (Bouger correction density 2.67 g/cc) and gravity station locations in the area of interest. Figure taken from Wintermoon Geotechnologies (2016).

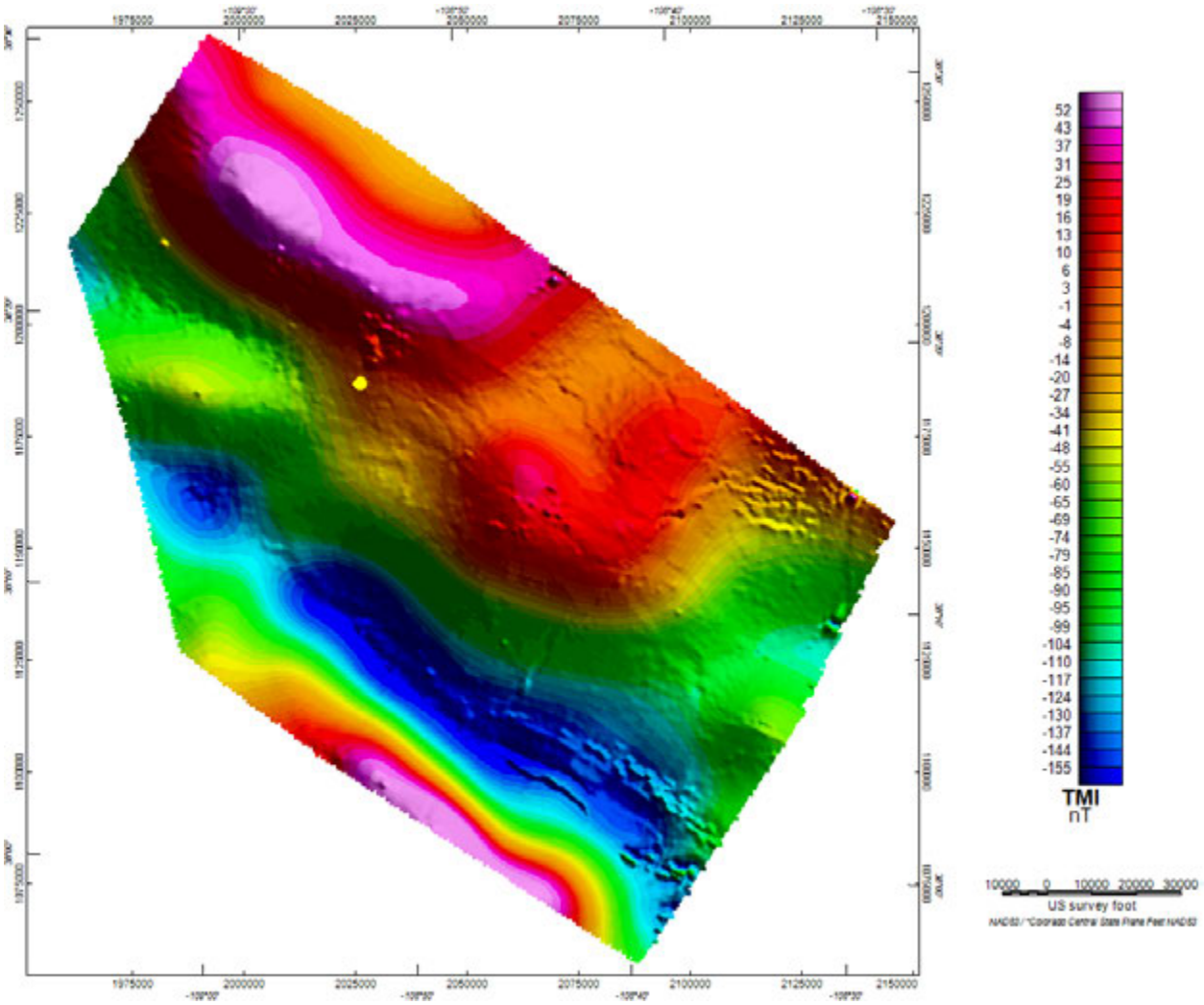

Figure 4-16. Final total magnetic intensity (TMI) grid of 2016 high-resolution aeromagnetic survey of the area of interest. The location of the PVU Injection Well #1 is marked in yellow. Figure taken from Wintermoon Geotechnologies (2016).

4.3.3 Results

The interpretation of the aeromagnetic data was divided into two phases. The first phase included three main tasks: data enhancement, map-based interpretation, and integrated 2D modeling along five seismic reflection lines, which incorporated gravity data and formation tops from the seismic reflection interpretation. The second phase included 3D modeling of the entire survey area.

4.3.3.1 Data Enhancements

A large number of data enhancements are included in Wintermoon Geotechnologies (2016); only three of these figures are reproduced here. The first image (Figure 4-17) shows the TMI anomaly with a reduction-to-pole (RTP) filter applied. The RTP algorithm accounts for local magnetic inclination and declination and recomputes the local crustal magnetic field as it would appear at inclination = 90° and declination = 0°, which has the effect of shifting magnetic anomalies to lie directly over their geologic sources (Wintermoon Geotechnologies, 2016).

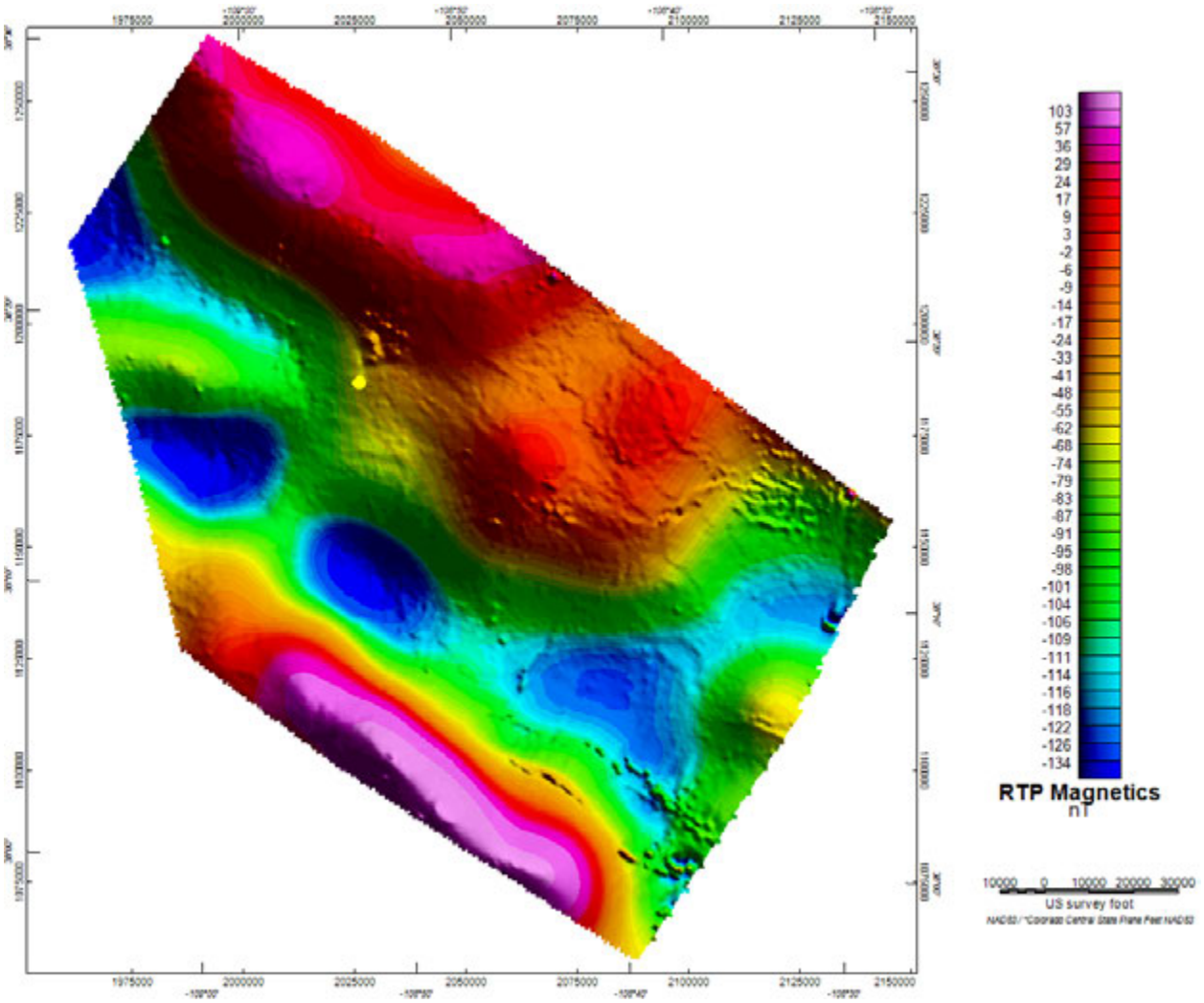

Figure 4-17. RTP grid of 2016 high-resolution aeromagnetic survey of the area of interest. Note the slight shift in anomaly position relative to the TMI grid in Figure 4-16. Figure taken from Wintermoon Geotechnologies (2016).

Figure 4-18 shows the first-vertical derivative (FVD) of the RTP magnetic field. The first-vertical derivative maps the vertical rate of change of the RTP magnetic field. The zero-contour of the FVD should map directly over the edge of the geologic source of the anomaly, and thus this enhancement highlights the edges of anomalies. However, this image shows significant short-wavelength character, which is most effected by shallow sources, while we are more interested in the long-wavelength anomalies basement sources.

To highlight the long-wavelength anomalies, the FVD was upward-continued by 500 meters (Figure 4-19). This algorithm computes the magnetic anomaly that would have been recorded had the survey been flown 500 meters higher. Upward continuation has the effect of attenuating the short-wavelength features and highlighting long-wavelength, likely basement-sourced features.

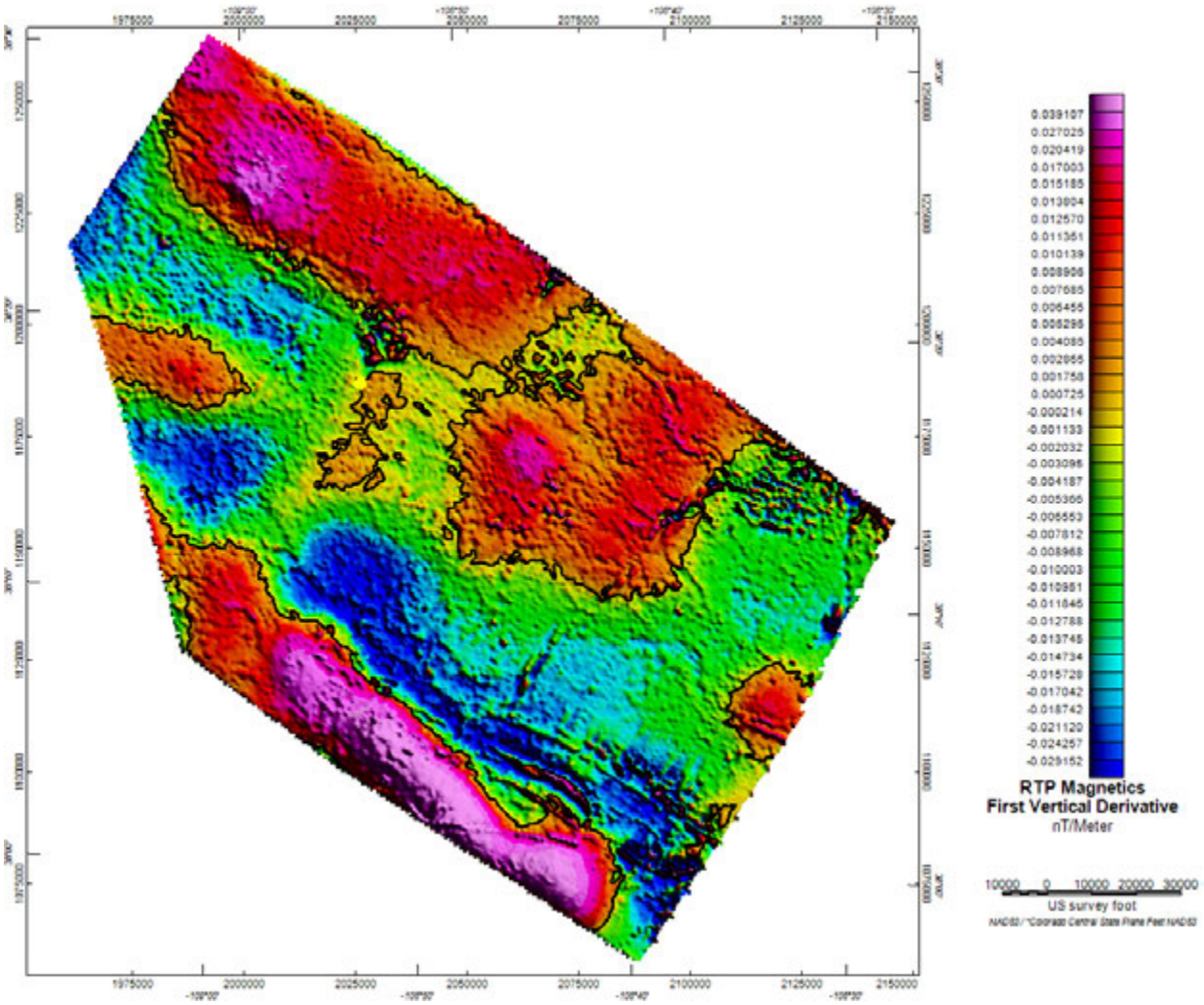

Figure 4-18. FVD of the RTP magnetic field. The zero contour is plotted in black. Note the presence of short-wavelength character in this enhancement. Figure taken from Wintermoon Geotechnologies (2016).

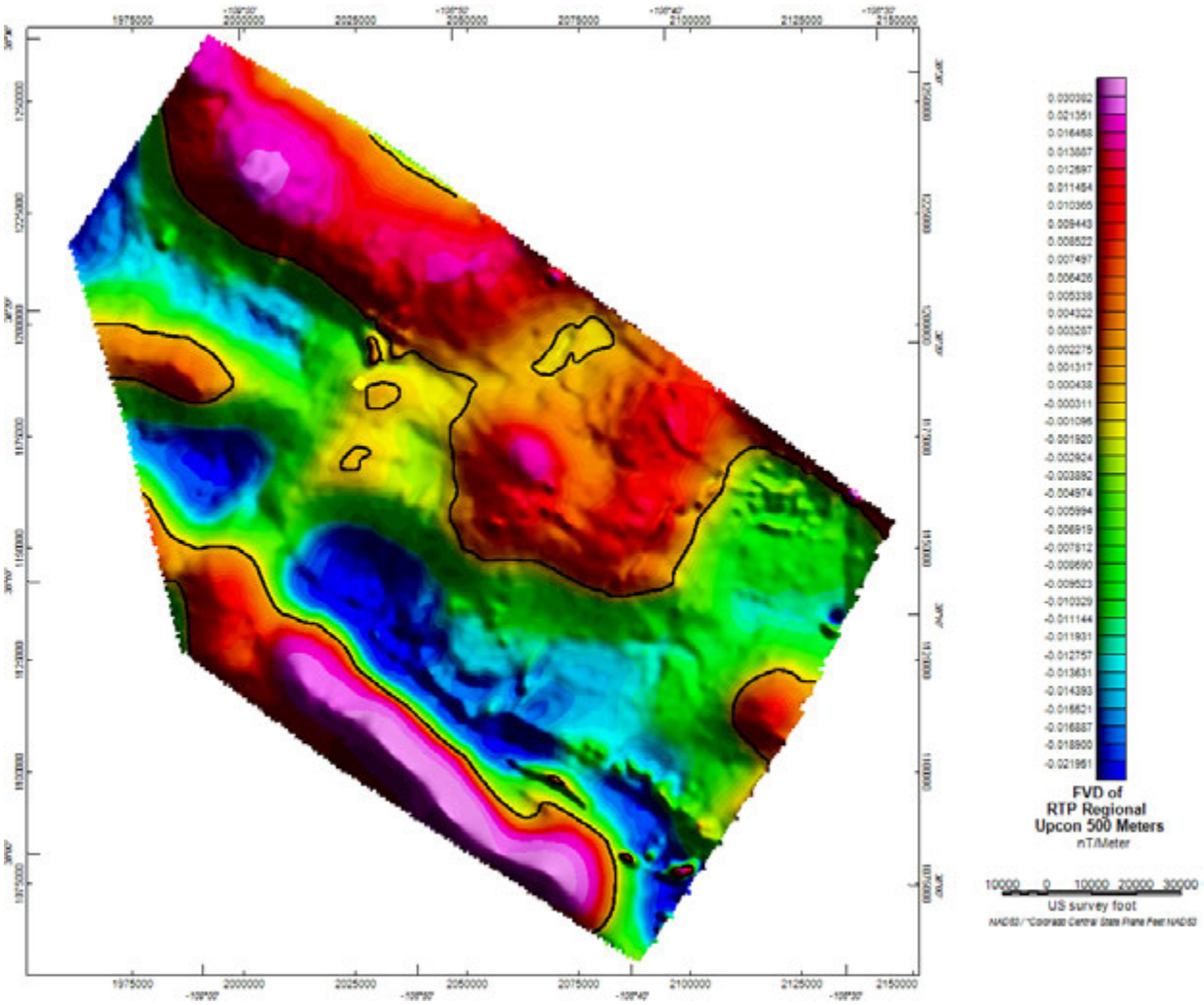

Figure 4-19. FVD of RTP regional upward continued by 500 meters (1640 feet). The zero contour is plotted in black, outlining the proposed edges of basement-sourced magnetic anomalies. Figure taken from Wintermoon Geotechnologies (2016).

4.3.3.2 Map-based interpretation

Three types of lineaments were identified from the aeromagnetic data: first-order lineaments (associated with basement structure and composition), second-order lineaments (associated with magnetic sources in the shallow basement), and third-order lineaments (associated with magnetic sources in the sedimentary section) (Figure 4-20). While the lineaments are plotted on the map of the FVD of RTP regional upward continued by 500 meters, a variety of map enhancements were used to interpret these lineaments.

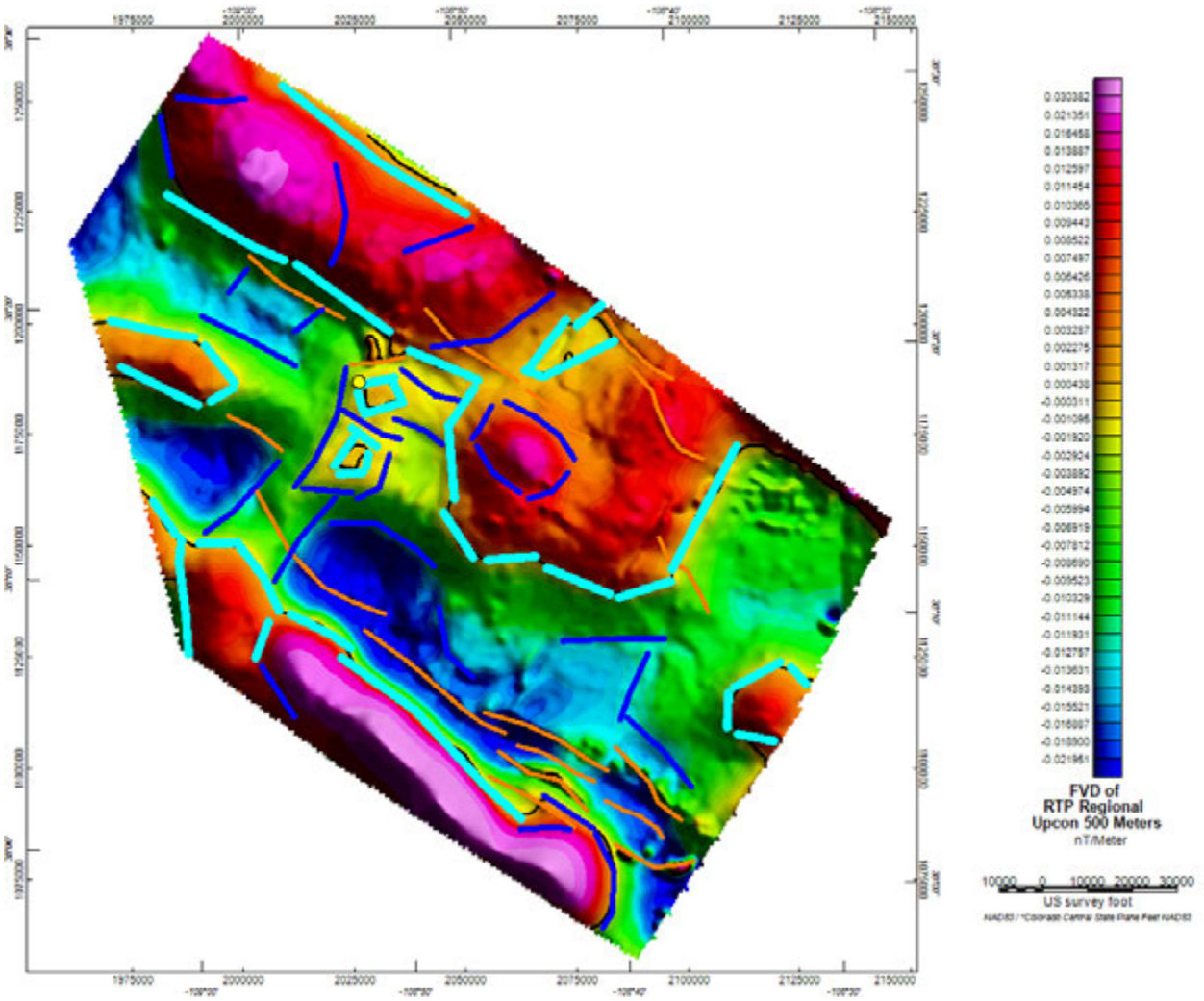

Figure 4-20. First-order crustal lineaments mapped in cyan, second-order lineaments mapped in blue, and third-order lineaments mapped in orange on the FVD of RTP regional upward continued by 500 meters map. Figure taken from Wintermoon Geotechnologies (2016).

4.3.3.3 Iterative forward 2D gravity and magnetics modeling

To quantify the interpretation of basement discontinuities and heterogeneous composition among various basement blocks, 2D forward gravity and magnetics models were constructed along five key seismic lines, with their locations shown in Figure 4-21.

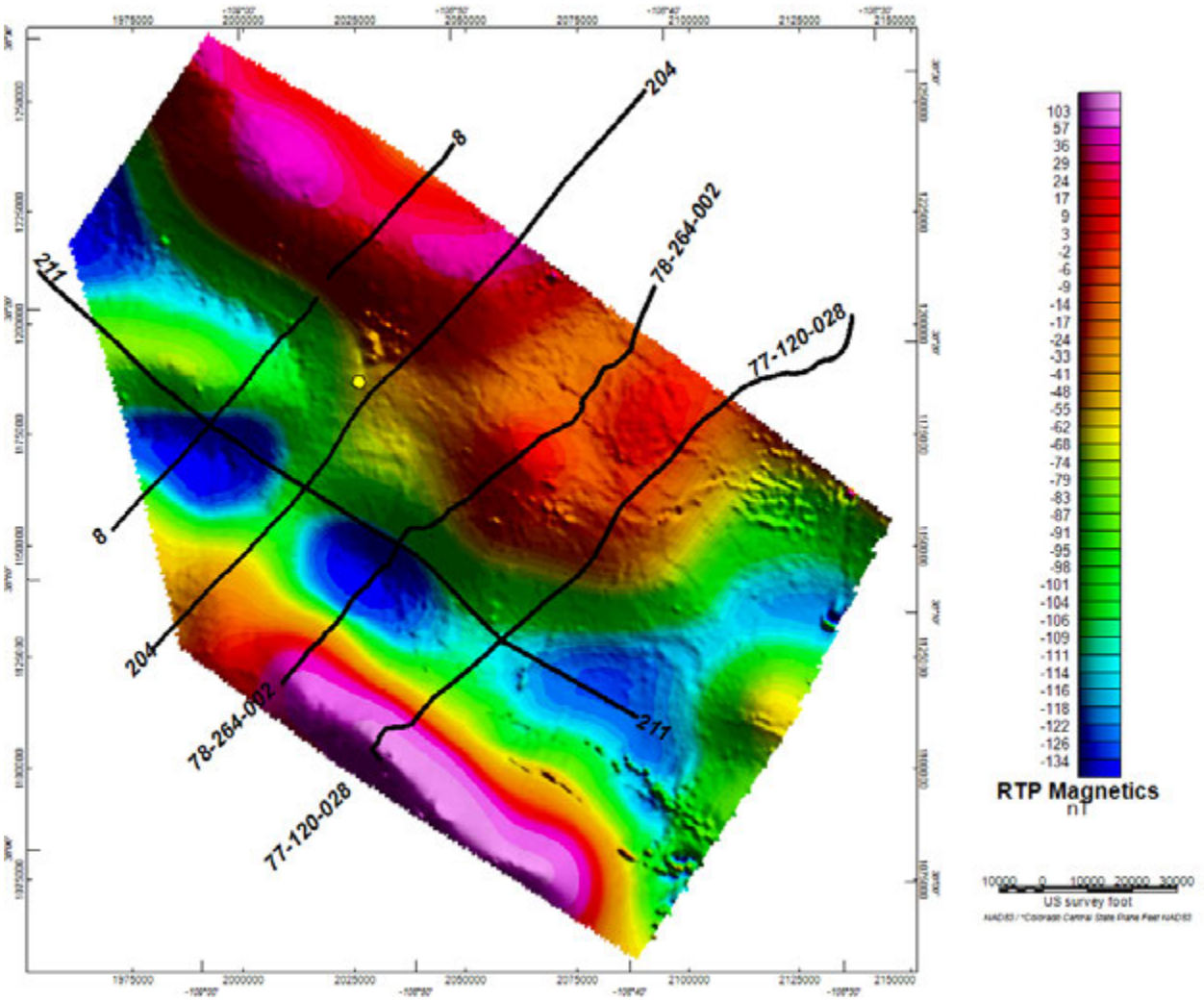

Figure 4-21. Locations of seismic lines used in 2D gravity and magnetics modeling. Profiles are plotted on the RTP magnetics anomaly map. PVU Injection Well #1 is plotted in yellow. Figure taken from Wintermoon Geotechnologies (2016).

The final models are shown in Figure 4-22 through Figure 4-26. The models use the top of the basement and the tops of the Paradox salt and Leadville formations from the preliminary seismic interpretation. The basement is divided into vertical prisms, and the magnetic susceptibilities and densities are varied between prisms to match the magnetic and gravity anomalies. These models are non-unique; there are many other configurations of basement structure and magnetic susceptibility whose responses will match the observed data. However, this model is constrained by seismic information (Wintermoon Geotechnologies, 2016).

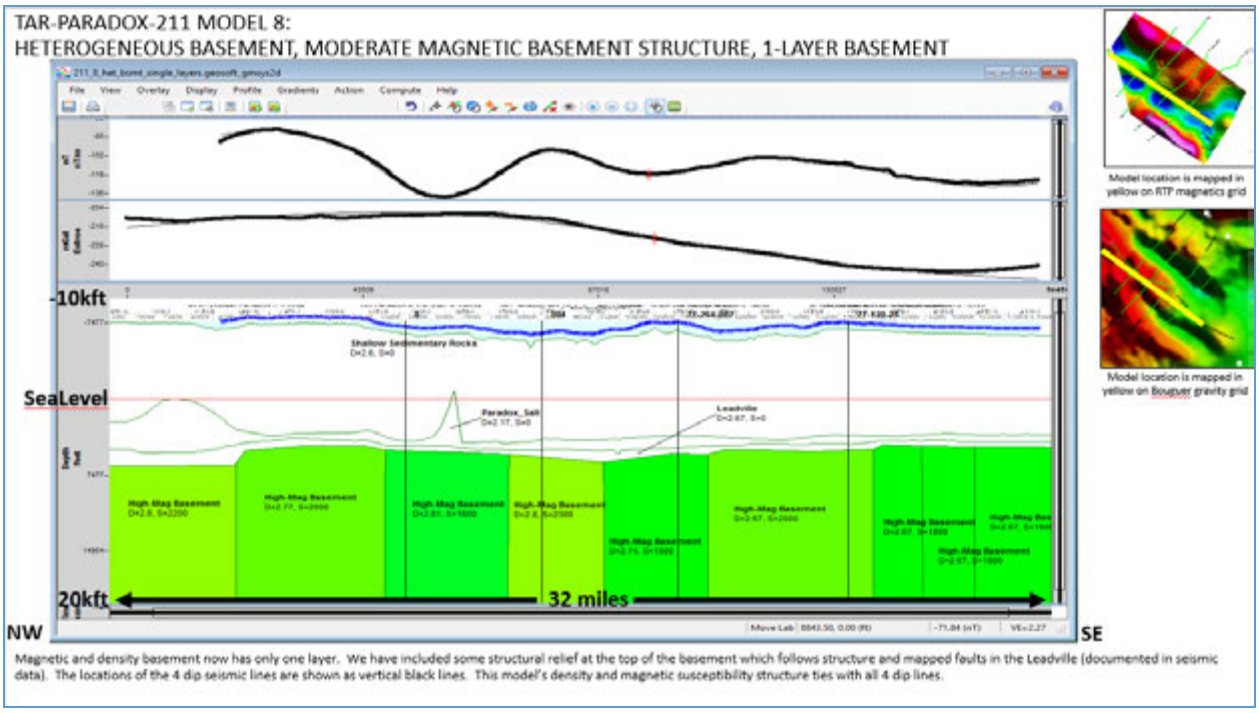

Figure 4-22. Final heterogeneous basement prism model for strike line TAR-PARADOX-211. Note the excellent agreement between the computed responses and observed signal for both gravity and magnetics. Figure taken from Wintermoon Geotechnologies (2016).

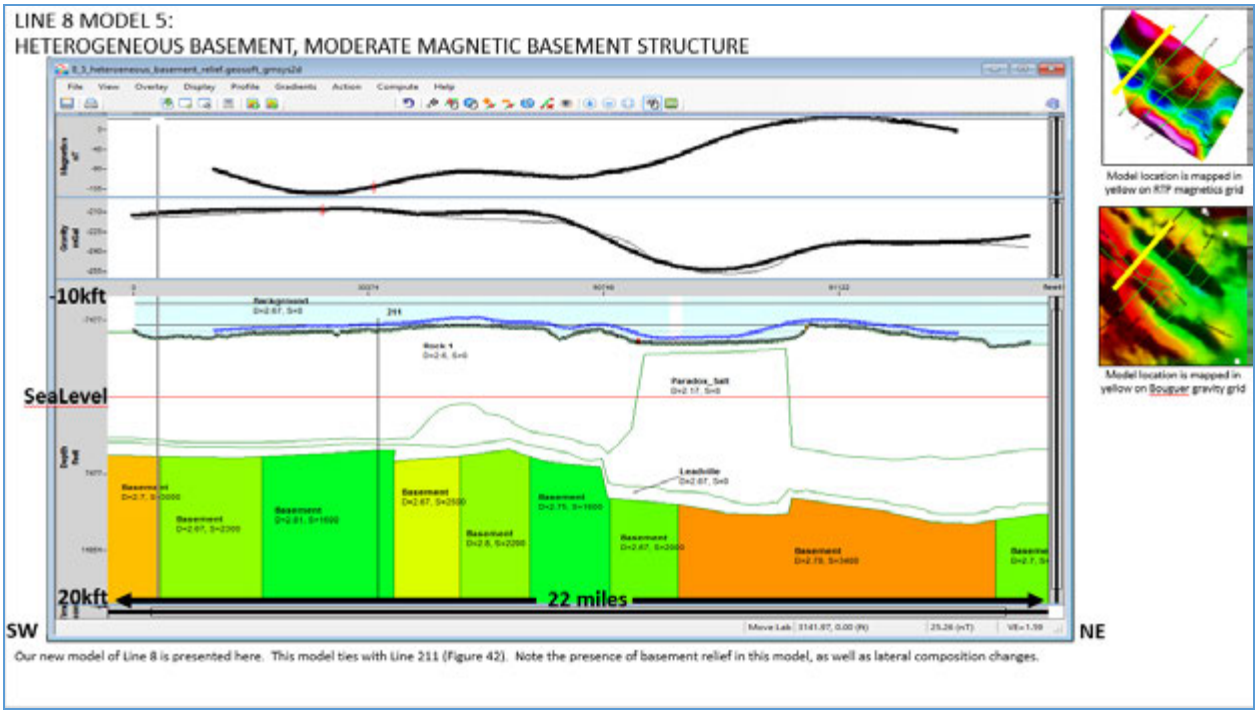

Figure 4-23. Final heterogeneous basement prism model for dip line TAR-PARAROX-8. Again very good agreement is seen between the computed responses and observed signals for both gravity and magnetics. Figure taken from Wintermoon Geotechnologies (2016).

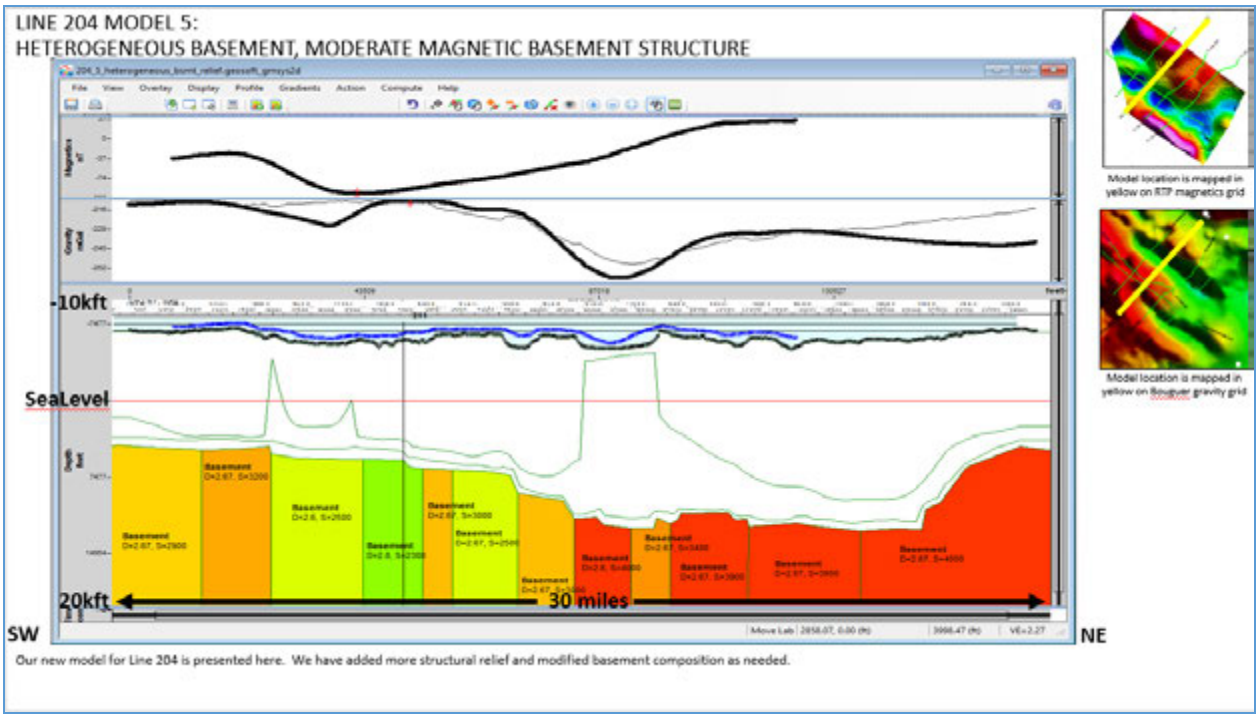

Figure 4-24. Final heterogeneous basement prism model for dip line TAR-PARADOX-204. Very good agreement is seen between the computed response and observed signal for RTP magnetics. Gravity shows more divergence, however. Figure taken from Wintermoon Geotechnologies (2016).

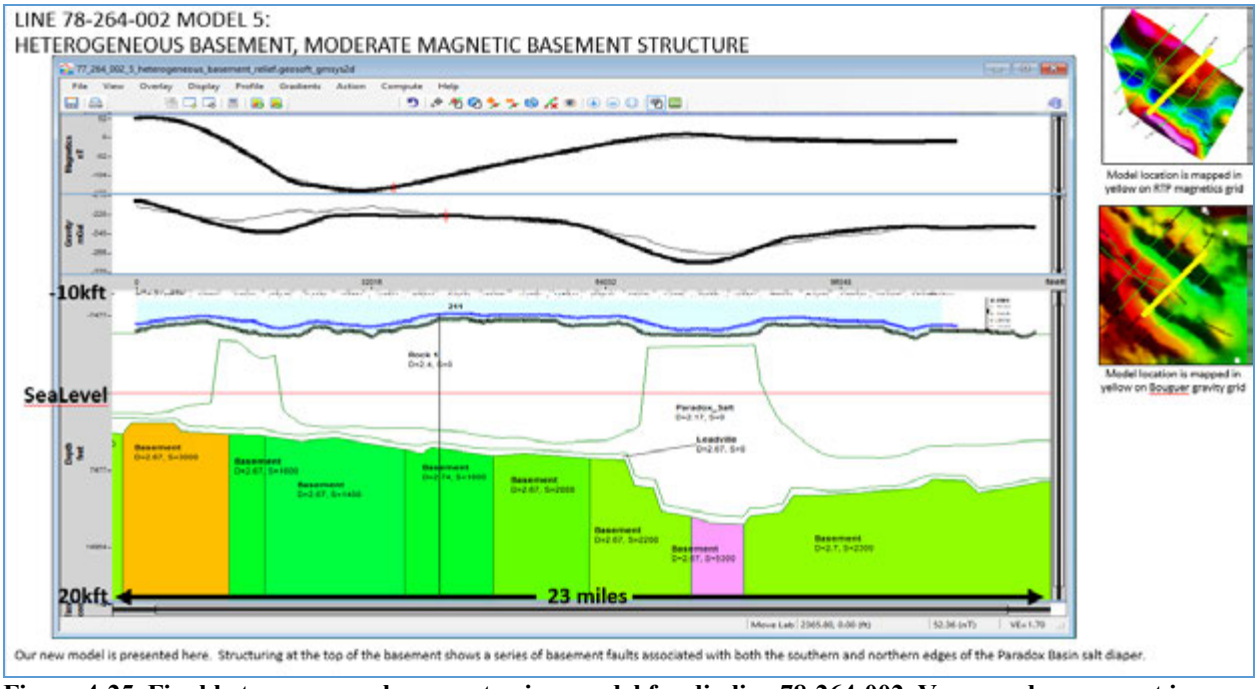

Figure 4-25. Final heterogeneous basement prism model for dip line 78-264-002. Very good agreement is seen between the computed response and observed signal for RTP magnetics. Gravity does not fit so well. Figure taken from Wintermoon Geotechnologies (2016).

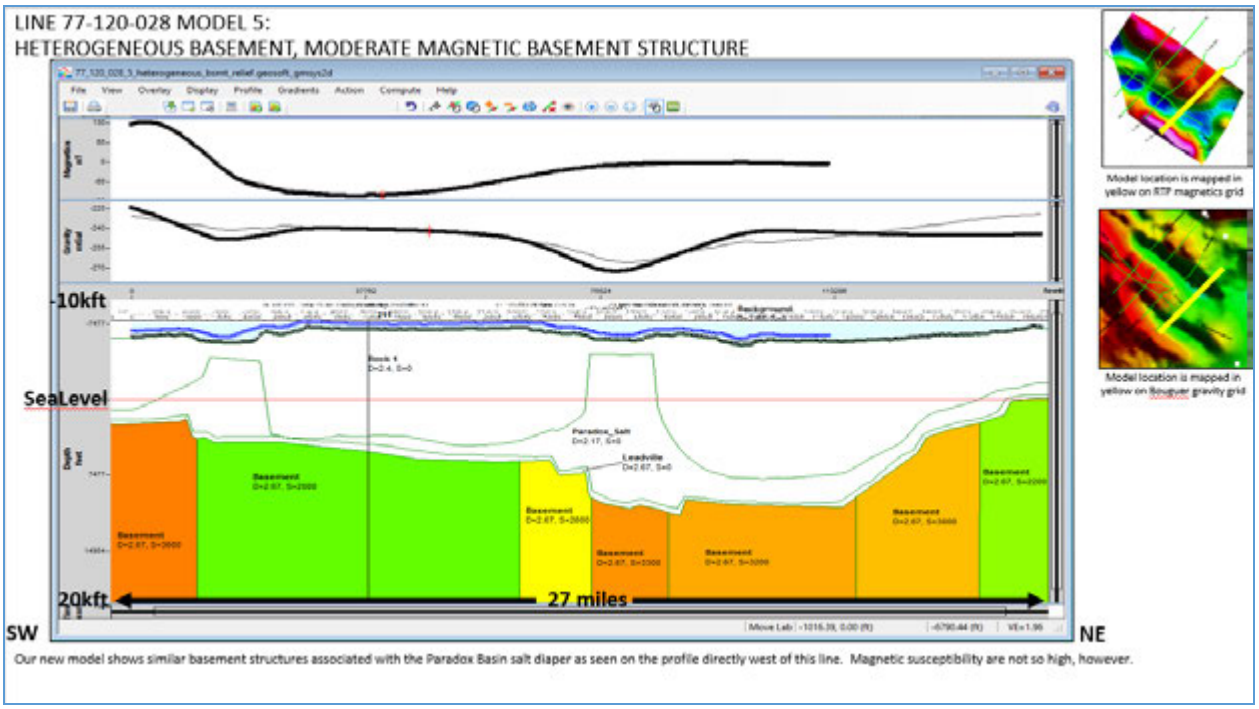

Figure 4-26. Final heterogeneous basement prism model for dip line 77-120-028. Very good agreement is een between the computed response and observed signal for RTP magnetics and only fair agreement for gravity. Figure taken from Wintermoon Geotechnologies (2016).

4.3.3.4 3D modeling

3D modeling of the magnetic basement was used to identify basement blocks of felsic and intermediate composition. The boundaries between basement blocks could then be compared to the locations of Precambrian faults.

The depth to the magnetic basement was calculated using Werner deconvolution (Wintermoon Geotechnologies, 2017). The depth to the Precambrian basement, taken from the seismic reflection interpretation, was used to constrain the minimum depth to the magnetic basement.

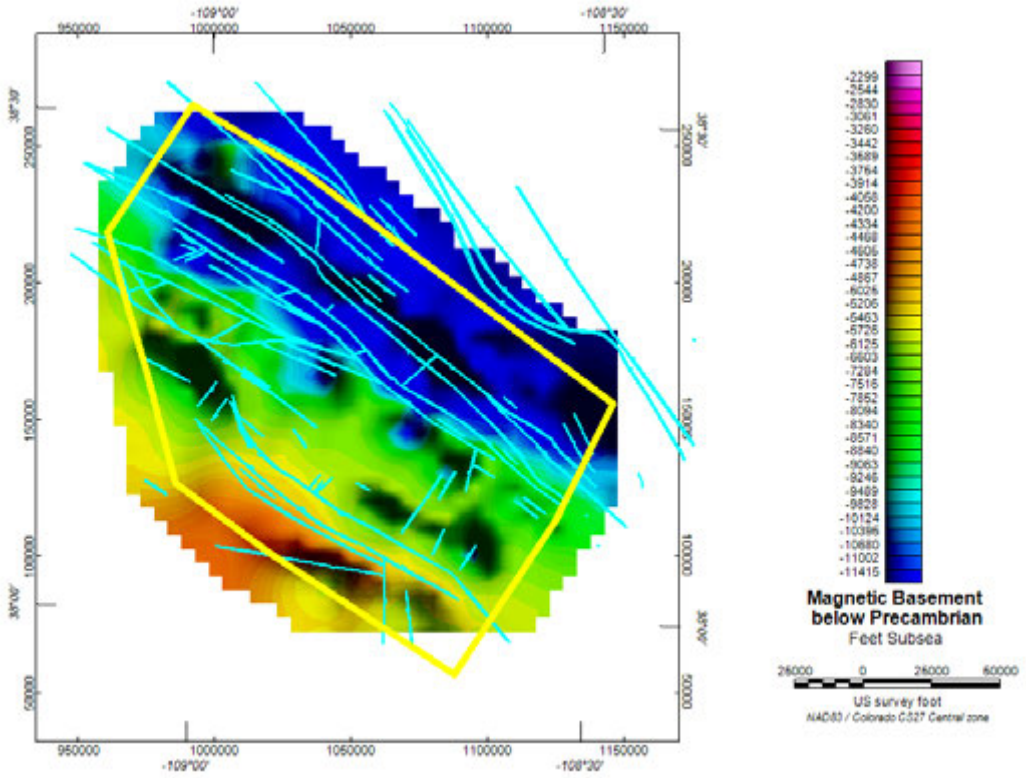

Figure 4-27. Magnetic basement depth surface interpreted from Werner deconvolution depth solutions. Cyan lines represent the basement faults interpreted from the seismic reflection lines. Figure taken from Wintermoon Geotechnologies (2017).

One key result from the 3D modeling of the aeromagnetic data is that the observed magnetic anomaly cannot be fit by forward modeling using only structural relief on the magnetic basement; variation in magnetic susceptibility is also necessary. The grid of magnetic susceptibility inverted using the magnetic basement depth surface in Figure 4-27 is shown in Figure 4-28. The Precambrian faults are plotted on the grid of magnetic susceptibility. Some of the fault locations closely correlate with the basement composition boundaries (Wintermoon Geotechnologies, 2017).

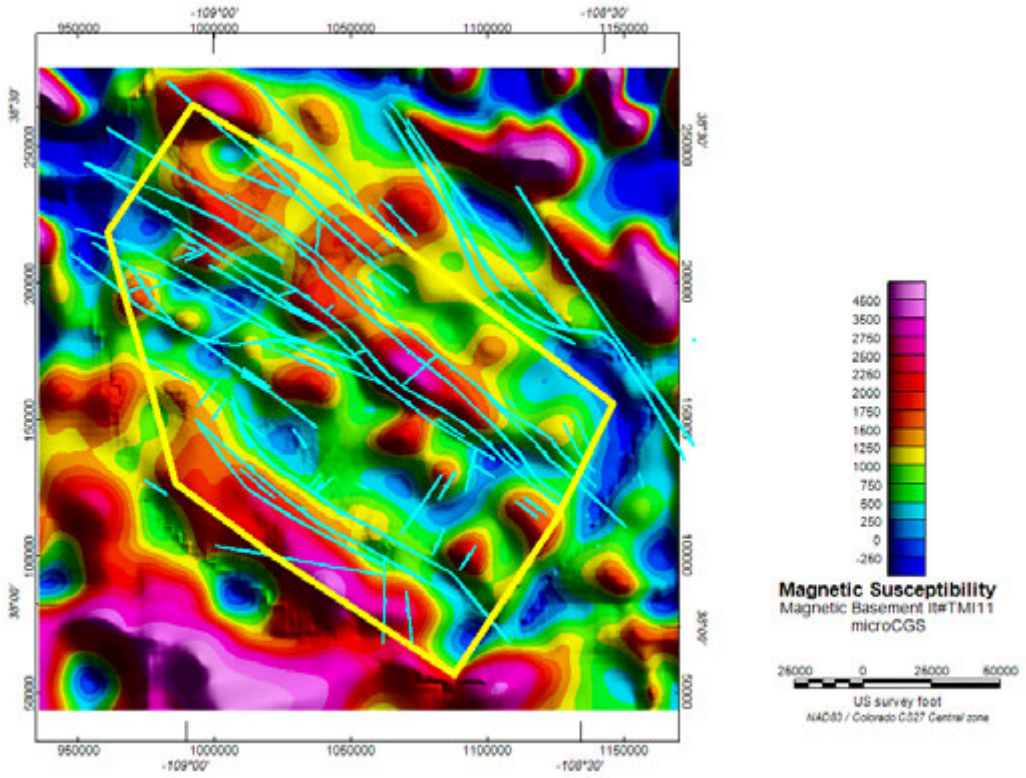

Figure 4-28. Grid of lateral magnetic susceptibility for magnetic basement derived from inversion of the TMI upward continued to 10,000'. The blue and green areas have relatively low magnetic susceptibility and are probably felsic composition. The warmer colors represent more iron-rich basement, probably with intermediate composition. Figure taken from Wintermoon Geotechnologies (2017).

4.4 Earthquake Data

4.4.1 Method

Earthquake hypocenters can be used to illuminate the subsurface geology, if the hypocenter locations are sufficiently accurate. Hypocenter lineations can illuminate the locations and orientations of subsurface faults. If one can assume that the majority of earthquakes occur within a particular geologic layer, the locations of hypocenters can also be used to map the structure of that layer. For example, an abrupt change in the depths of hypocenters may indicate a fault offsetting the layer in which those hypocenters occur.

The orientations of focal mechanisms can also provide information about the subsurface, particularly the preexisting stress field. In particular, slip is more likely to occur in favorably oriented directions.

4.4.2 Data

Seismic monitoring of the Paradox Valley area began in 1983, with installation of the first stations of the Paradox Valley Seismic Network (PVSN). Network installation was timed to provide a pre-injection baseline of naturally occurring background seismicity. The network has been continuously operated since 1985, and has been expanded and updated over the years to

respond to changing seismicity patterns. The current configuration consists of a surface array of 20 digitally recorded, broadband, three-component sensors. PVSN has recorded more than 6000 shallow earthquakes in the vicinity of Paradox Valley since injection tests began in 1991 (Figure 4-29). In contrast, only one earthquake was recorded for the six years prior to injection, and it occurred about 19 km from PVU Injection Well #1.

Several distinct groups, or clusters, of induced seismicity have developed over the history of PVU injection (Figure 4-29). By the end of the injection tests in 1995, earthquakes were occurring up to 3-4 km from the well. We refer to this area of induced seismicity immediately surrounding the injection well as the near-well region. In 1997, about 1 year after the start of long-term injection, earthquakes began occurring 6-8 km northwest of the injection well. We identify this group of induced seismicity as the northwest (NW) cluster. In mid-2000, PVSN first detected earthquakes 12-14 km from the injection well, along the northern edge of Paradox Valley. Several distinct clusters of earthquakes have occurred along the northern edges of the valley since 2000. We refer to the earthquakes in all of these groups as northern-valley events. An earthquake was first detected about 6 km southeast of the injection well in 2004, and the seismicity rate in this area markedly increased beginning in 2010, leading to the development of a distinct earthquake cluster. We identify this compact group of earthquakes as the southeast (SE) cluster. In recent years, earthquakes have been detected in previously aseismic areas, including: toward the southeast to a distance of ~18 km from the injection well, east toward Uravan to a distance of ~17 km from the well, west to a distance of ~14 km from the well, and at several locations within northern Paradox Valley.

Absolute event hypocenters are initially computed using manually-determined arrival times and a 3D velocity model. These hypocenters are subsequently refined using a relative relocation method and precise time differences derived from waveform cross-correlation, which improves the accuracy of the relative event hypocenters. Approximately 87% of all induced earthquakes and 93% of induced earthquakes with duration magnitude ≥ 0 occurring within 10 km of PVU Injection Well #1 were relocated. We refer to the hypocenters relocated using relative relocation as ‘a-quality’ hypocenters, and those not relocated as ‘b-quality’ hypocenters. Preliminary analysis of the relocated events indicate that the location uncertainty of an individual earthquake with respect to the other earthquakes to which it is tied is generally less than 50 meters horizontally and 100 meters vertically (Block and others, 2015).

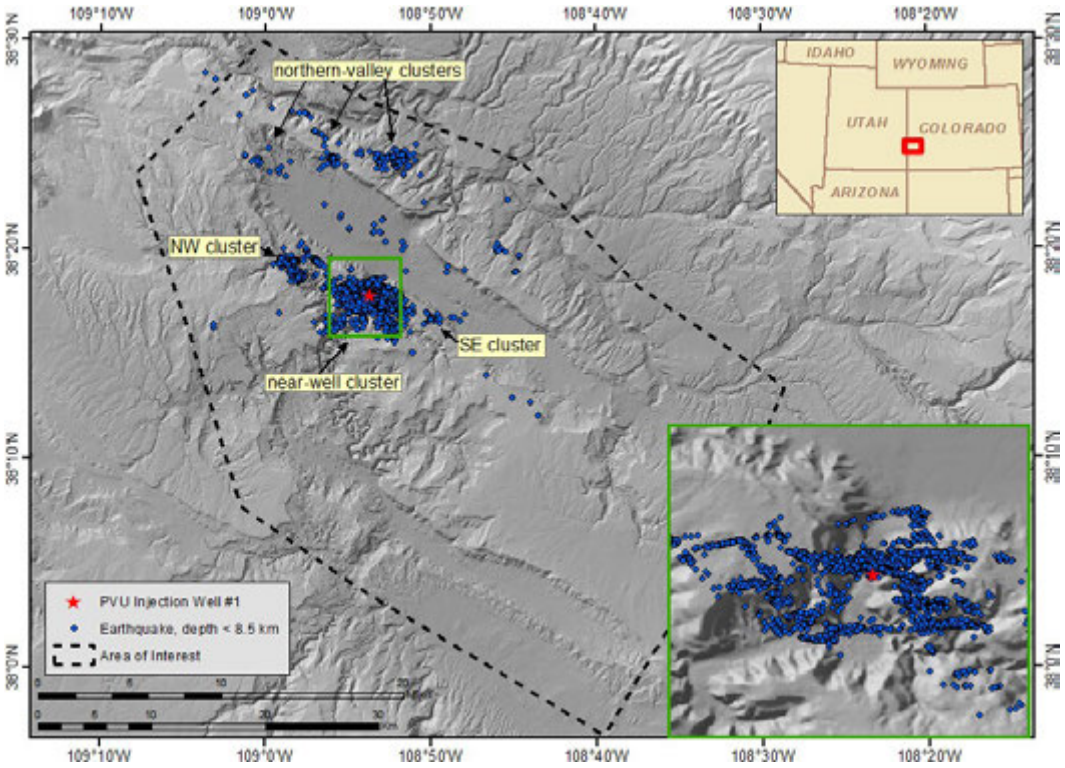

Figure 4-29. All shallow earthquakes (depth < 8.5 km) recorded by PVSN since the beginning of injection tests in 1991. Green rectangle shows the location of the inset map (bottom right). To better observe lineations in the earthquakes, the inset map includes only those events that were relocated using a relative relocation algorithm.

4.4.3 Results

The spatiotemporal pattern of precise relative-relocated hypocenters of induced earthquakes was used to modify the subsurface geological model developed in the 1980s (Section 3). First, the relative elevations of clusters of hypocenters were analyzed and the abrupt lateral changes in their relative elevations were used as an indicator of the locations of major fault block boundaries, assuming that hypocenters occur preferentially within the subhorizontal target injection formations. Based on distinct vertical offsets of nearby earthquake clusters and lateral variations in hypocenter elevations, the locations of two northwest-striking faults were inferred near the well (Faults 1 and 2, Figure 4-30). Three fault blocks are created by these two normal faults (Blocks 1, 2, and 3, Figure 4-30) (Block and others, 2015).

The near-juxtaposition of Blocks 1 and 3 at location Y (Figure 4-30) may be explained by either a lateral offset of Faults 1 and 2 by a northeast-trending strike-slip fault (Figure 4-31, model 1) or a merging of normal Faults 1 and 2 into a single normal fault southeast of the injection well (Figure 4-31, model 2). In both fault models, an additional normal fault northeast of the injection well is included (Fault 3). The inferred existence and location of this fault is based on the 1980s seismic reflection data interpretations (Figure 3-2) and the geographic extent of epicenters east of the injection well (Block and others, 2015). Bremkamp and others (1984) interpreted the presence of a northwest-striking normal fault very close to this location, with sufficient vertical offset to act as an impermeable barrier to fluid flow through the Leadville formation. The lack of induced seismicity east of Fault 3 supports this conclusion.

The scarcity of induced seismicity more than 600 m southwest of Fault 1 suggests the presence of an impermeable barrier to the southwest. The geological log of the Wray Mesa Unit #1, drilled in 1961 to a depth of 3434 m, indicates the absence of the Leadville formation (King and others, 2014). This well is in Block 1, at the southwest edge of the NW cluster of induced seismicity (Figure 4-31). The Mississippian Leadville and underlying Devonian formations underwent extensive weathering and erosion on structural highs during late Mississippian to early Pennsylvanian time (Campbell, 1981; Bremkamp and Harr, 1988). In addition to thinning and removal of the Leadville, the weathered interval has significantly decreased reservoir potential due to infilling of previously porous zones with clay. If weathering and erosion occurred along a structural high parallel to Fault 1, then the absence or degradation of the primary target injection formation may inhibit fluid flow toward the southwest and explain the scarcity of induced seismicity in this region (Figure 4-31). Alternatively, there could be another northwest-trending normal fault in this location with sufficient vertical offset to inhibit lateral fluid flow through the target injection formations (Campbell, 1981; Block and others, 2015).

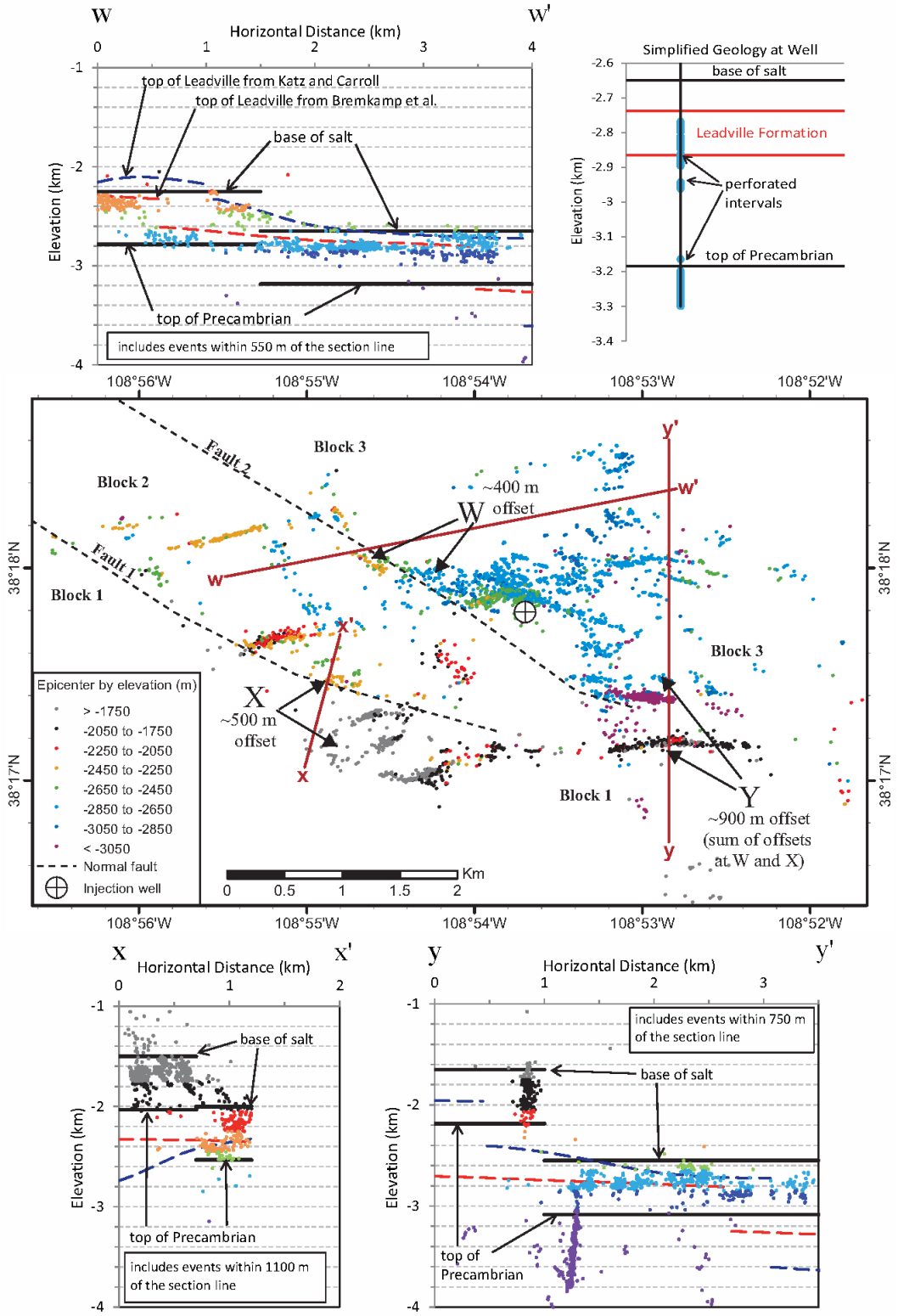

Figure 4-30 Map showing epicenters of earthquakes occurring in the near-well region of induced seismicity, color-coded by hypocenter elevation (center), and cross sections showing distinct vertical offsets of hypocenters (top and bottom). Only a-quality hypocenters from the event relative location are included. The labels 'W', 'X', and 'Y' on the map identify abrupt lateral changes in hypocenter elevations. Two northwest-striking normal faults interpreted from the hypocenter elevation patterns are shown. Our interpreted base of

the Paradox salt and top of the Precambrian (solid black lines) and the interpreted top of the Leadville formation from Katz and Carroll (1984) (dashed purple line) and Bremkamp and others (1984) (dashed red line) are shown in each cross-section. A simplified geological section at the PVU wellbore is included at upper right for reference. Figure taken from Block and others (2015).

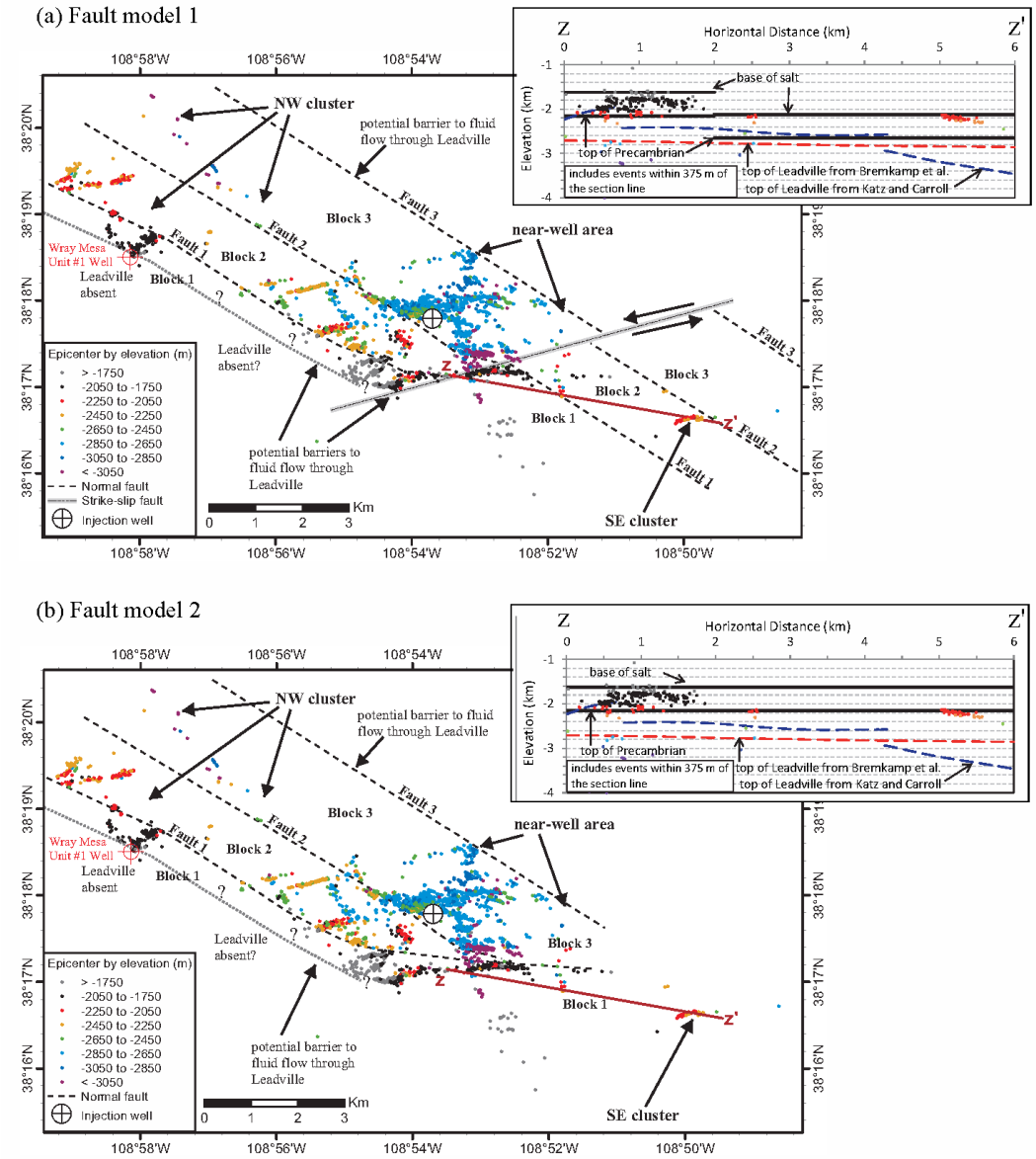

Figure 4-31. Maps showing epicenters of earthquakes occurring in the near-well, northwest, and southeast clusters, color-coded by hypocenter elevation, with interpreted faults: (a) fault model 1 (b) fault model 2. The inset cross sections show simplified interpreted geological structure between the near-well area and the SE cluster in each model. Only a-quality hypocenters from the event relative location are included. The normal faults and the fault blocks delineated are labeled for purposes of discussion (see text). The primary injection target formation, the Leadville, is absent in the Wray Mesa Unit #1 well shown. Figure taken from Block and others (2015).

The second course of analysis was to examine the spatial distribution and temporal evolution of linear patterns of earthquake epicenters, leading to the identification of two orientations of large-scale near-vertical faults, which were interpreted to have developed as a conjugate fracture set, and were denoted as fault orientations *A* and *B*. Epicenter lineations along a third direction, denoted as *C*, were observed near the injection well (Block and others, 2015). The spatial distribution of seismicity along the inferred fault orientations is illustrated with the map of near-well seismicity shown in Figure 4-32.

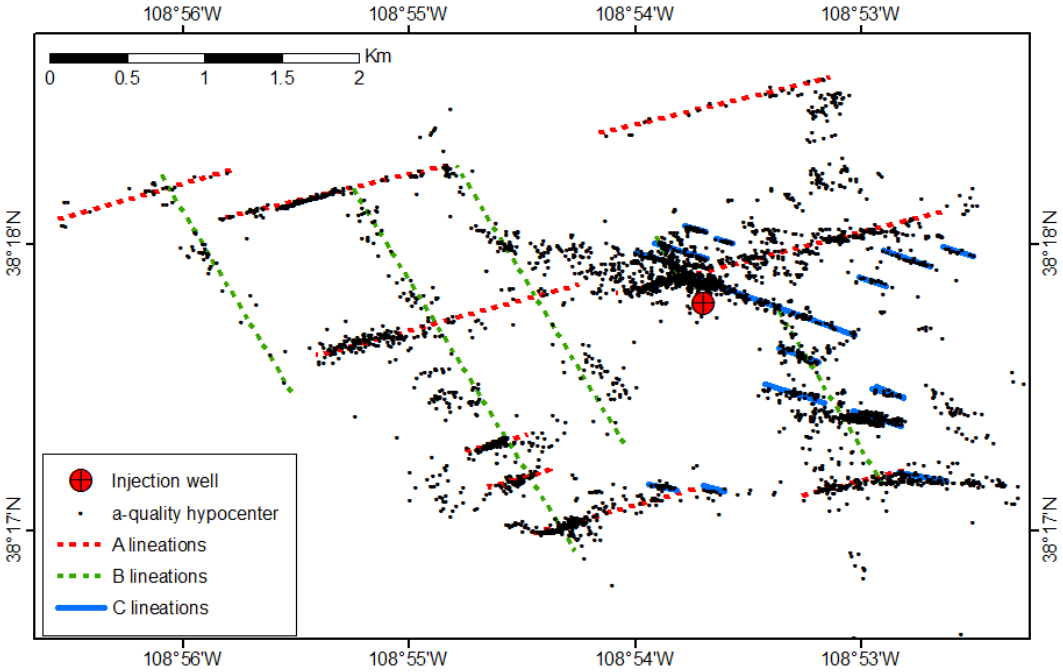

Figure 4-32. Map showing epicenters of shallow a-quality earthquakes in the near-well area, with lineations in the *A*-direction (N77°E), *B*-direction (N31°W), and *C*-direction (N71°W) overlaid.

The focal mechanisms of approximately 600 earthquakes with a-quality hypocenters were analyzed in the near-well area, the northwest cluster, and the southeast cluster. This analysis found that most focal mechanisms are strike-slip (83 per cent), have a *P*-axis oriented to the northwest, have a *T*-axis oriented to the northeast, and have one fault plane consistent with the orientations of the epicenter lineations on which the events occur (Block and others, 2015) (Figure 4-33). These results are consistent with an earlier focal mechanism analysis by Ake and others (2005).

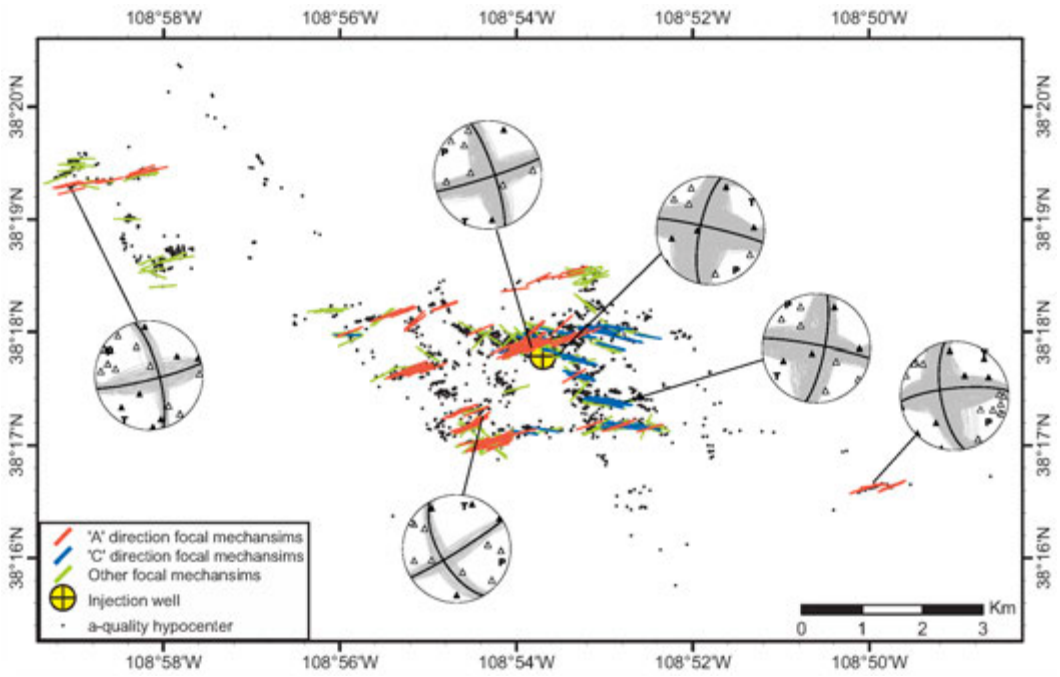

Figure 4-33. Strikes of favored fault planes classified by direction, including 'A' direction events (red), 'C' direction events (blue) and unclassified events (green). Example focal mechanisms include all possible solutions (gray lines), and preferred mechanisms (black line). Black triangles denote compressional first motion picks and white triangles denote tensional first motion picks. Preferred mechanisms' *P*- and *T*-axes are labeled. Figure taken from Block and others (2015).

4.5 Stress data

4.5.1 Method

Detailed log data necessary to determine *in situ* stress and pore pressure are generally unavailable for the Paradox Valley area. In order to estimate the regional-scale *in situ* stress magnitudes, we use simple models that relate the maximum to minimum effective stress ratio to various physical parameters, constrained by the few measurements that are available.

From Anderson faulting theory, the following condition applies for a critically oriented, cohesionless fault at the frictional limit:

$$(S_1 - P)/(S_3 - P) = \left(\sqrt{1+\mu^2} + \mu\right)^2 \qquad (4.1)$$

where $S_1 \geq S_2 \geq S_3$ are the total principal stresses, P is pore pressure, and μ is the coefficient of internal friction (Jaeger and others, 2007; Zoback, 2007). This condition is appropriate for crustal stresses that are in equilibrium with the frictional strength of pre-existing faults, which we will assume to be the case for the Paradox Valley area. For $\mu = 0.6$, the ratio of effective stresses predicted by equation (4.1) is about 3.1.

If the principal stress directions are assumed to be oriented approximately in the vertical and horizontal directions, then a normal faulting stress environment is defined by the condition $S_1 = S_{vertical}$ and $S_3 = S_{H\min}$, where $S_{Vertical}$ is the lithostatic load, and $S_{H\min}$ is the minimum compressive stress in the horizontal direction. The stresses at depth z are given by $S_1(z) = S_{Vertical}(z) \approx \bar{\rho} g z$, and $S_3(z) = S_{H\min}(z)$, where $\bar{\rho} = \frac{1}{z}\int_0^z \rho(\xi)\, d\xi$ is the average crustal rock density, and g is gravity. The lithostatic load can be estimated from density logs, while the minimum horizontal stress can be estimated from leak-off tests. For a critically-stressed normal faulting environment subject to hydrostatic pore pressure, and assuming typical crustal values of density and internal friction, it can be shown that equation (4.1) results in $S_{H\min} \approx 0.6\, S_{Vertical}$ (Zoback, 2007).

A strike-slip faulting environment is defined by $S_1 = S_{H\max}$ and $S_2 = S_{Vertical}$, where $S_{H\max}$ is the maximum compressive stress in the horizontal direction. In this case, $S_{H\max} \geq S_{Vertical} \geq S_{H\min}$. A stress environment that is transitional from normal to strike-slip faulting is described by $S_{H\max} \approx S_{Vertical} > S_{H\min}$.

The ratio of maximum and minimum effective stresses for a normal-faulting environment can be estimated from

$$\left(S_{Vertical} - P\right) / \left(S_{H\min} - P\right) = \left(1 - \nu_{eff}\right) / \nu_{eff} \qquad (4.2)$$

where ν_{eff} is an effective Poisson's ratio (Eaton, 1969; Zoback, 2007). In this case, it is assumed that $S_H = S_{H\max} = S_{H\min}$, i.e., the horizontal stresses are isotropic. If $\nu_{eff} = 0.25$, then the ratio of effective stresses predicted by equation (4.2) is 3.0, similar to the value of 3.1 predicted using equation (4.1) for $\mu = 0.6$.

Equation (4.2) was used as the basis for many of the Paradox Valley Unit reports from the 1980s (e.g., Dewan, 1988) that computed a fracture closure pressure, aka $S_{H\min}$, assuming that $\nu_{eff} = \nu$, where ν is the value of Poisson's ratio obtained from sonic logs, and $S_{Vertical}$ was computed from density log data. There are significant issues in using equation (4.2) this way (e.g., Zoback, 2007; Wang and others, 2015), and its application to Paradox Valley may be unrealistic for several reasons: (1) it describes the instantaneous horizontal stress change due to an increase in the vertical stress, rather than the long-term accumulation of stress; (2) it assumes that the horizontal stress is the same in all directions, in contrast to focal mechanism and hypocenter lineation data suggesting that induced earthquakes are occurring on fractures with a consistent orientation; and (3) it may require an ν_{eff} that needs to be determined for different depths.

Wellbore breakout widths and tensile fractures potentially observable in televiewer logs can provide additional constraints on the *in situ* stress magnitudes. For example, Zoback (2007)

showed that drilling-induced tensile fractures in vertical wellbore walls can occur in a strike-slip faulting environment when the following condition is satisfied:

$$\left(S_{H\max} - P\right)/\left(S_{H\min} - P\right) = 3 \qquad (4.3)$$

assuming negligible tensile rock strength, thermal effects, and minimal difference between mud weight and formation pore pressure. The value of the effective stress ratio predicted by equation (4.3) is similar to the value of 3.1 obtained from equation (4.1) for $\mu = 0.6$. Wellbore breakout widths provide additional constraints, however available televiewer data for the Paradox Valley area generally are of insufficient quality to reliably identify tensile fractures or accurately measure wellbore breakout widths.

In a porous, isotropic, and laterally infinite reservoir, a change in pore pressure ΔP due to injection leads to a change in horizontal stress

$$\Delta S_{H\max} = \Delta S_{H\min} = \alpha \frac{(1-2\nu)}{(1-\nu)} \Delta P \qquad (4.4)$$

where α is Biot's coefficient, and ν is Poisson's ratio (Zoback, 2007). For $\alpha = 1$ and $\nu = 0.25$, eqn. (4.4) becomes $\Delta S_{H\max} = \Delta S_{H\min} = \frac{2}{3}\Delta P$.

Principal stress directions potentially can be determined from caliper and televiewer logs, and from earthquake focal mechanisms. Elongation of vertical boreholes in the $S_{H\min}$ direction can be observed in the caliper and televiewer data, however, extensive borehole washouts or key seats can limit the utility of this data. While the P and T axes of earthquake focal mechanisms do not necessarily coincide with the S_1 and S_3 directions (McKenzie, 1969), it may be possible to invert for those directions from a group of focal mechanisms having the same stress environment but different fault orientations (Martínez-Garzón and others, 2014).

4.5.2 Data

Results from drill stem tests (DST) provide information on pore pressures in the Paradox Valley area. An analysis of DST data for the entire Paradox Basin by Allis and others (2009) yields a composite pressure gradient for the Leadville formation of 0.47 psi/ft over an elevation range of +4000 to -10,000 feet above sea level (Figure 4-34). That gradient is about 10% greater than hydrostatic for fresh water, but is consistent with the density of brines. The head elevation is about 3900 ft, coinciding with the elevation of the lower Green River and Cataract Canyon section of the Colorado River where the rivers traverse the Leadville formation. Allis and others (2009) conclude that the Mississippian and older reservoirs across most of the Paradox Basin are in good hydrological communication with the Colorado River system. List (2016) also compiled DST results in the Leadville formation near Lisbon and Paradox Valley to map a potentiometric surface, assuming a fresh water pressure gradient of 0.43 psi/ft (Figure 4-12).

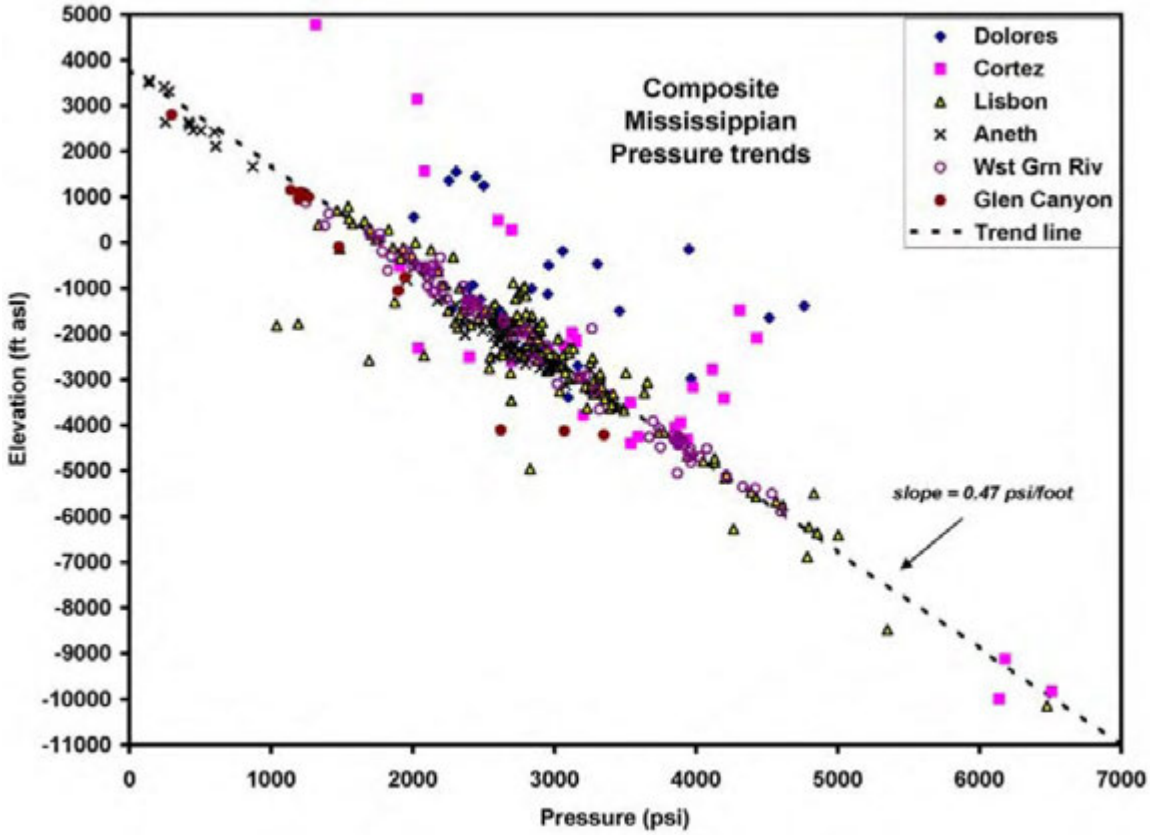

Figure 4-34. Composite pressure trend in the Leadville formation from DST results throughout the Paradox Basin. Data from the Paradox Valley and Lisbon Valley areas are shown as open triangles. The composite pore pressure gradient is 0.47 psi/ft, consistent with brines, and the head (zero-pressure intercept) is at elevation 3,900 ft, consistent with the elevation where the Leadville outcrops along the Colorado River. Figure and data from Allis and others (2009).

The least-compressive principal stress S_3 can be measured from leak-off tests, although such data has been found only for PVU Injection Well #1, and that data is of limited quality. Leak-off tests for PVU Injection Well #1 were conducted for the top of the Leadville formation on June 21 and June 22, 1987, and the results reported in Dunn (1987). The 10.98" OD intermediate casing was first pressure tested to 5,000 psi during cement clean-out operations to a depth of 14,053 ft. An 8-1/2" hole was then drilled 18 feet below the casing to perform the leak-off test, and the open hole had about 10 feet of fill. Equipment failures prevented the June 21st test from achieving full pressure. The test was restarted on June 22nd, and the drill pipe was pressurized to 5075 psi (according to the gauge on the choke manifold) or 4610 psi (according to the gauge on the drill pipe). A hand-drawn plot of pressure vs. pump strokes for the June 22nd test is provided as Figure 3 of the Dunn (1987) report, and suggests a leak-off pressure of about 4400-4600 psi using the choke manifold gauge data, and 4020-4090 psi using the drill pipe gauge data. Formation breakdown pressure was not reached in this test. Using the recorded drilling fluid density of 8.5 lb/gal, the measured leak-off pressures result in a fracture closure pressure gradient of 0.76 psi/ft (choke manifold gauge) and 0.73 psi/ft (drill pipe gauge) for the top of the Leadville formation. Corresponding $S_3 = S_{H\min}$ values are 10,700 psi (choke manifold gauge) and 10,300 psi (drill pipe gauge), at a depth of 14,060 ft.

The PVU #1 mechanical properties log provides an overburden pressure of 16,500 psi at a depth of 14,050 ft, and a pore pressure of 6140 psi (Dewan, 1988). Using the leak-off test $S_{H\min}$ value and this overburden pressure value, the $S_{H\min}/S_{vertical}$ ratio is 0.65 (choke manifold gauge) and 0.62 (drill pipe gauge). If a normal faulting environment is assumed, and the pore pressure and overburden from the mechanical log is used, then equation (4.1) predicts an $S_{H\min}/S_{vertical}$ ratio of 0.57, which is somewhat smaller than value obtained from the leak-off test. The discrepancy could be the result of assuming too high a value of internal friction for equation (4.1), or could result from uncertainty in the recorded leak-off pressure values.

An analysis of the PVU#1 televiewer and caliper logs was performed by Steve Hickman and his colleagues at USGS (Hickman, 2003) to determine $S_{H\max}$ directions. Although the televiewer image quality was reported as "not very good," an average $S_{H\max}$ direction of N84°W ±5° was obtained over the depth interval from 14100 to 15300 feet below the wellhead, which includes most of the Leadville formation. Hickman also examined caliper data from the dipmeter logs, and found that the direction differed from the breakout data by about 30° ($S_{H\max}$ direction of N55°W), which was attributed to possible damage to the dipmeter logging tool, or uncertainty in whether the long axis of the borehole was correctly tracked. Dewan (1987) reports that the quality of these logs "was not up to par" because of wellbore washouts.

Earthquake focal mechanisms also can provide constraints on the direction of the principal stresses, and on the faulting environment. Block and others (2015) analyzed focal mechanisms from 600 induced earthquakes and found that about 83% of the mechanisms were strike-slip, with many of the rest normal or oblique-normal. Similar results were obtained by Ake and others (2005). A stress inversion of the focal mechanism data from Block and others (2015) yielded an $S_{H\max}$ direction of N55°W. Data from the World Stress Map (Heidbach and others) within 150 km of Paradox Valley indicates an $S_{H\max}$ direction of N78°W. An analysis of near-vertical shear fractures inferred from lineations of precise hypocenters by Block and others (2015) indicated that the N78°W direction from the World Stress Map provided greater consistency with the data than did the direction determined from the stress inversion.

4.5.3 Results

The regional *in situ* stress state for the Paradox Valley area is inferred from earthquake focal mechanisms, hypocenter lineations, well log data, and an assumption that the crust is critically stressed. Under these assumptions and interpretations, we infer that the regional *in situ* total principal stresses are oriented in the vertical and horizontal directions, with the maximum horizontal stress $S_{H\max}$ direction approximately N78°W. The magnitude of the total vertical stress $S_{Vertical}$ is approximately equal to the lithostatic load, which can be estimated from density logs. Assuming a hydrostatic pore pressure gradient throughout the crust, and a transitional strike-slip to normal faulting stress state, the magnitudes of the total horizontal stresses are estimated by $S_{h\min} \approx 0.6\, S_{H\max}$, $S_{H\max} \approx S_{Vertical}$.

Long-period stresses within the Paradox salt are assumed to be isotropic, and equal to the overburden stress, because the salt is assumed to behave plastically for large time scales. The salt

should provide a good confining layer for injection into the Leadville formation because the minimum horizontal stress in the salt will be equal to the overburden pressure, while the minimum horizontal stress in the Leadville will be about 60% of the overburden pressure. The base of the salt is typically 400 to 500 ft above the top of the Leadville, and topography is not flat lying, so the actual overburden stress in the salt likely will differ somewhat from this simple model.

4.6 InSAR

4.6.1 Method

Interferometric Synthetic Aperture Radar (InSAR) is a technique for mapping ground deformation using radar images of earth collected by orbiting satellites. Two radar images, or scenes, of the same area that were collected at different times from similar vantage points in space can be compared to each other. Any movement of the ground surface toward or away from the satellite can be measured and portrayed as an image of how the ground surface moved during the time between images (USGS, 2016). This image is known as an interferogram.

We expect uplift of the ground surface to have occurred near the injection well due to the volume of fluid that has been injected. While the injection is occurring at a depth of ~4.5 km, since the overlying layers are mostly rigid, some of the deformation will propagate to the surface. If this uplift can be detected with InSAR, it can provide constraints on the spatial extent of the area that has been pressurized by injection into the existing injection well.

4.6.2 Data

For this study, Synethic Aperture Radar (SAR) images were collected from UNAVCO's WInSAR consortium and National Aeronautics and Space Administration's (NASA) Alaska Satellite Facility archives. SAR scenes from various agencies like European Remote Sensing (ERS) satellites, ERS1 and ERS2, European Space Agency's Environmental Satellite (ENVISAT) and Japan Aerospace Exploration Agency's Advanced Land Observing Satellite "Daichi" (ALOS-1) were also collected. At least 143 SAR scenes were collected that span from 1992-2000 for ERS1, 1995-2011 for ERS2, 2004-2012 for ENVISAT, and 2006-2011 for ALOS-1. Data were processed using GMTSAR, an open source InSAR software (Besana-Ostman, 2016)

4.6.3 Results

Unfortunately, we have been unable to detect a signal that appears to be related to injection. On interferograms with good coherence (Figure 4-35), the displacement shows a strong correlation with topography, which suggests that it is related to seasonal variations, particularly seasonal rainfall variations which could cause soil to expand and contract. However, this result is not without value, as it constrains the maximum surface deformation to be less than the resolution of the InSAR data, accounting for the "noise" caused by these seasonal variations. The "noise" had a maximum amplitude of 2-10 cm (Besana-Ostman, 2016), thus it can be concluded that the uplift caused by PVU injection is less than 10 cm.

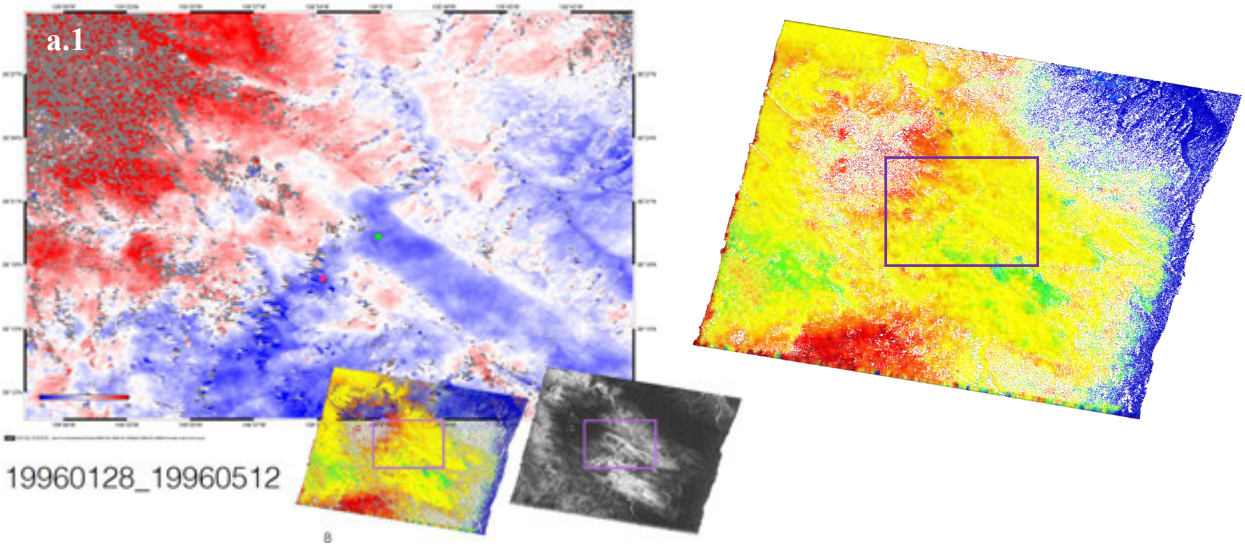

Figure 4-35. An example of a displacement map (a.1) with good coherence produced for Paradox Valley Unit (red dot) for ERS-2's 184_2835 scenes and its associated interference (a.2). Right inset in (a.1) shown as white pixels correspond to high coherence and gray/black pixels indicate low or no correlation. Middle inset shows unwrapped fringes of the line of sight shown in a.2. The area shown in a.1 is indicated by the rectangles in a.2 and the inset maps. Figure taken from Besana-Ostman (2016).

5 Integrated geologic model

5.1 Comparisons between different data sets

5.1.1 Seismic reflection and earthquake hypocenter data

Depths to the target injection formations and the locations of faults that offset those formations were interpreted using both the seismic reflection and earthquake hypocenter data (sections 4.1 and 4.4). In addition, both data sets were used to infer the presence of boundaries that inhibit lateral fluid flow through those formations. Here we compare the interpretations from these two data sets and discuss their consistencies and discrepancies.

The epicenters of most shallow earthquakes recorded since the start of PVU fluid injection lie northeast of one of the major NW-SE trending faults interpreted from the seismic reflection data, labeled *Fault A* in the map in Figure 5-1. This map includes earthquakes that are ≤ 10 km deep, relative to the ground surface elevation at the PVU injection well, and that occurred between the start of fluid injection in July 1991 and the end of 2016. The comparatively much smaller number of earthquakes more than 10 km deep that have been recorded are considered naturally occurring and are therefore excluded from the map. Epicenters computed with the relative event location method using precise time differences (a-quality events) and those computed using an absolute location method and manually-determined arrival times (b-quality events) are included. To eliminate earthquakes with the most poorly-constrained hypocenters, b-quality events with arrival times at less than six seismic stations or with a ratio of the distance to the closest seismic station divided by the focal depth more than two are excluded. Based on experimentation, these criteria eliminate hypocenters with the most poorly-constrained hypocenters, especially those with poorly-constrained depths, without introducing a spatial bias to the earthquake distribution. Eighty percent of the events eliminated have magnitude < M 0.5. No criterion for maximum azimuthal gap is included because this would eliminate a considerable number of earthquakes near the edges of the seismic network and bias the spatial distribution of epicenters.

The scarcity of seismicity southwest of *Fault A* is consistent with our interpretation of this fault as impermeable to lateral fluid flow through the primary target injection formation (the Leadville). This interpretation is based on a criterion of at least 500 ft (152 m) of vertical offset across the fault, as indicated by the structure map of the Leadville formation interpreted from the seismic reflection data. Fault segments that meet this criterion are represented by the thick black lines in Figure 5-1 and are referred to here as barrier faults. An impermeable boundary southwest of the injection well was also interpreted previously from the spatial distribution of a-quality hypocenters. During that analysis, the impermeable boundary was speculated to be due either to erosion of the Leadville formation or to an unidentified fault with large vertical offset (section 4.4.3 and Block and others, 2015). Hence, the presence of an impermeable NW-SE trending fault at this location is consistent with both the hypocenter analysis and the seismic reflection interpretations.

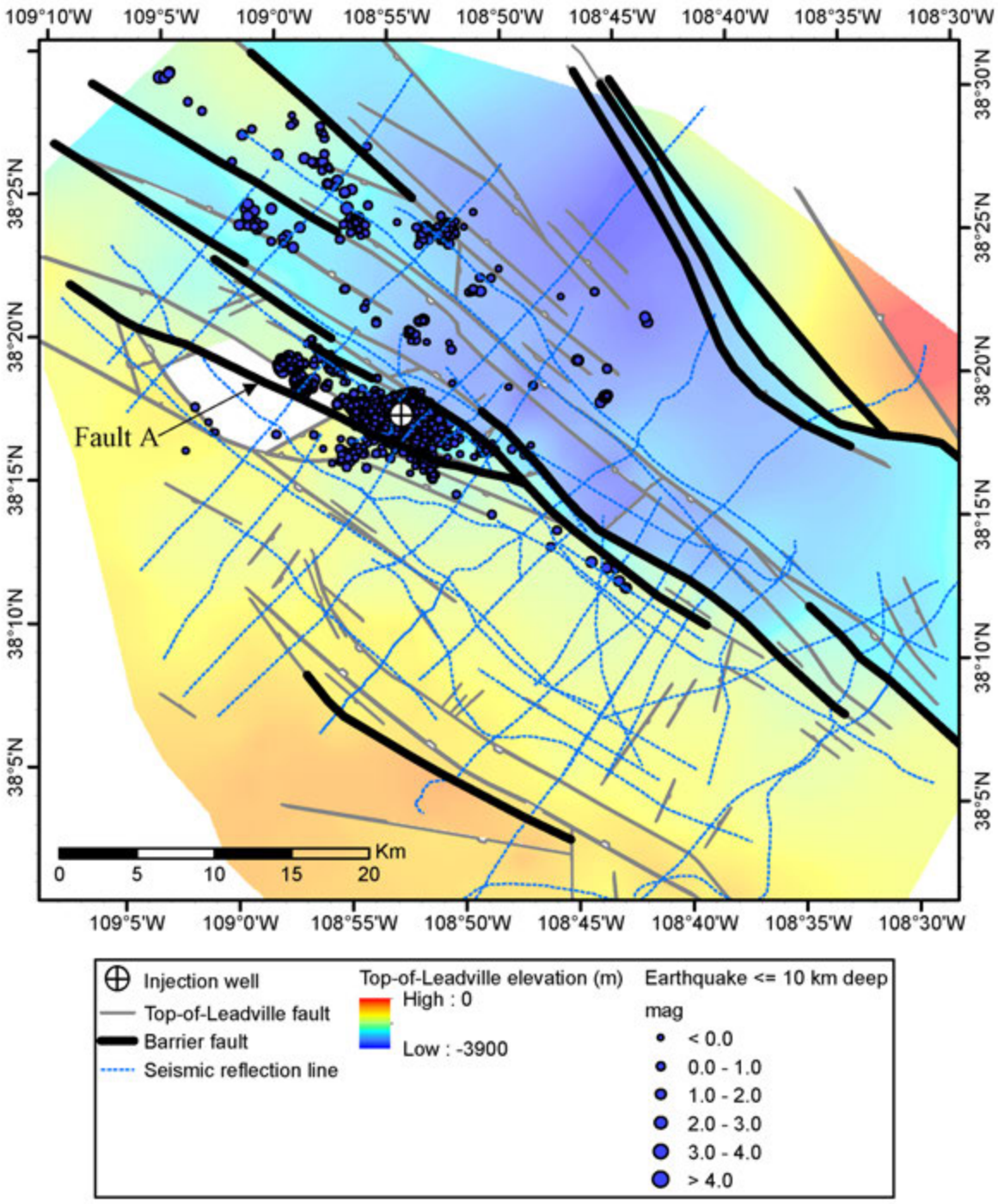

Figure 5-1. Epicenters of shallow earthquakes (≤ 10 km deep) recorded between 1991 and 2016 overlaid on the structure map of the Leadville formation interpreted from the seismic reflection data. The white area represents a region where the Leadville formation is absent due to erosion. The thick black lines indicate fault segments that we have interpreted as impermeable to lateral fluid flow through the Leadville formation, based on a vertical offset ≥ 500 ft.

The correspondence between the impermeable fault barriers interpreted from the seismic reflection data and the spatial distribution of earthquakes is clearer if we consider only those earthquakes whose hypocenters lie within the depth range of the target injection formations. This is because the earthquakes that occur within the target injection formations are more likely to be induced by injection-related pore pressure perturbations than those that occur in over-lying or under-lying formations, which may be triggered by strain-related stress changes. Similarly, earthquakes that occur beyond impermeable fault barriers are more likely to be due to strain-related stress changes than pore pressure increase.

The map in Figure 5-2 shows epicenters of earthquakes that occur within or near the depth range of the target injection formations, as indicated by the interpreted seismic reflection horizons. The target injection formations at PVU Injection Well #1 range from the upper Leadville formation to the upper ~100 m of the Precambrian. Because of uncertainty in the interpolation of seismic reflection horizons between the 2D seismic lines and uncertainty in the time-to-depth conversion, we consider a depth range that includes a 200-m uncertainty in both the upper and lower limits. Hence, the injection interval for these purposes is considered to include depths from 200 m above the top of the Leadville formation to 300 m below the top of the Precambrian. This uncertainty is arbitrary, as no depth uncertainty analysis has been performed. In reality, the uncertainty also varies spatially, with the depths being more accurate in fault blocks with deep wells providing data on depths to formation tops than in fault blocks without well control.

When considering only those earthquakes that lie within our defined depth interval of the target injection formations, the earthquake cloud surrounding the injection well abruptly ends at the location of *Fault A* (Figure 5-2). Extremely few earthquakes have occurred within the target injection formation depth interval southwest of *Fault A*. This observation provides further support for the presence of a barrier fault at this location.

The majority of earthquakes southwest of *Fault A* occur shallower than our defined depth interval of the target injection formations, and some of the earthquakes occur deeper than this interval. This can be observed in the map presented in Figure 5-3. The earthquakes in this map are color-coded by their relation to the target injection formations. The white symbols represent earthquakes shallower than the defined depth interval, the blue symbols represent earthquakes that lie within the target injection formations depth interval, and the red symbols represent earthquakes below the defined depth interval.

The spatial relation of the earthquake hypocenters on either side of *Fault A* is shown more clearly by the cross sections presented in
Figure 5-4 and Figure 5-5. The formation tops labeled in the cross sections (top of Paradox salt, Leadville, and Precambrian) are taken from the seismic reflection interpretations. Hypocenters of earthquakes occurring within 2 km of each profile are projected onto the cross sections. The thick black line represents *Fault A*. These cross sections clearly show that virtually all of the earthquakes south of the interpreted barrier fault occur either much shallower than the target injection formations (above the Paradox salt) or within the basement. Our preliminary interpretation is that these earthquakes are triggered by deformation-related stress changes outside of the boundary of the pressured reservoir. At this time we cannot exclude the possibility that pore pressures are migrating vertically along *Fault A* and intruding

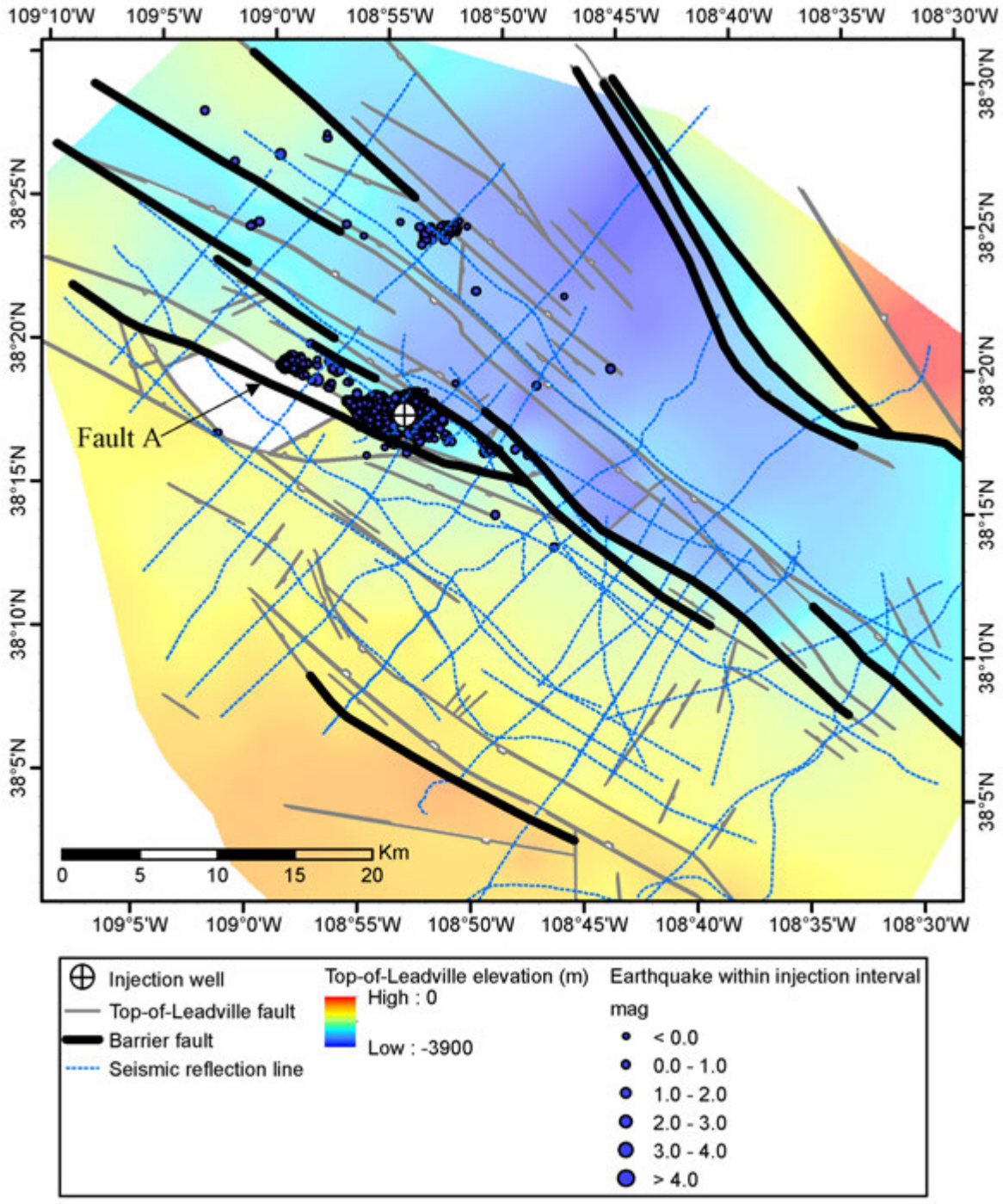

Figure 5-2. Epicenters of shallow earthquakes (≤ 10 km deep) within or near the target injection formations overlaid on the structure map of the Leadville formation interpreted from the seismic reflection data. The white area represents a region where the Leadville formation is absent due to erosion. The thick black lines indicate fault segments that we have interpreted as impermeable to lateral fluid flow through the Leadville formation, based on a vertical offset ≥ 500 ft.

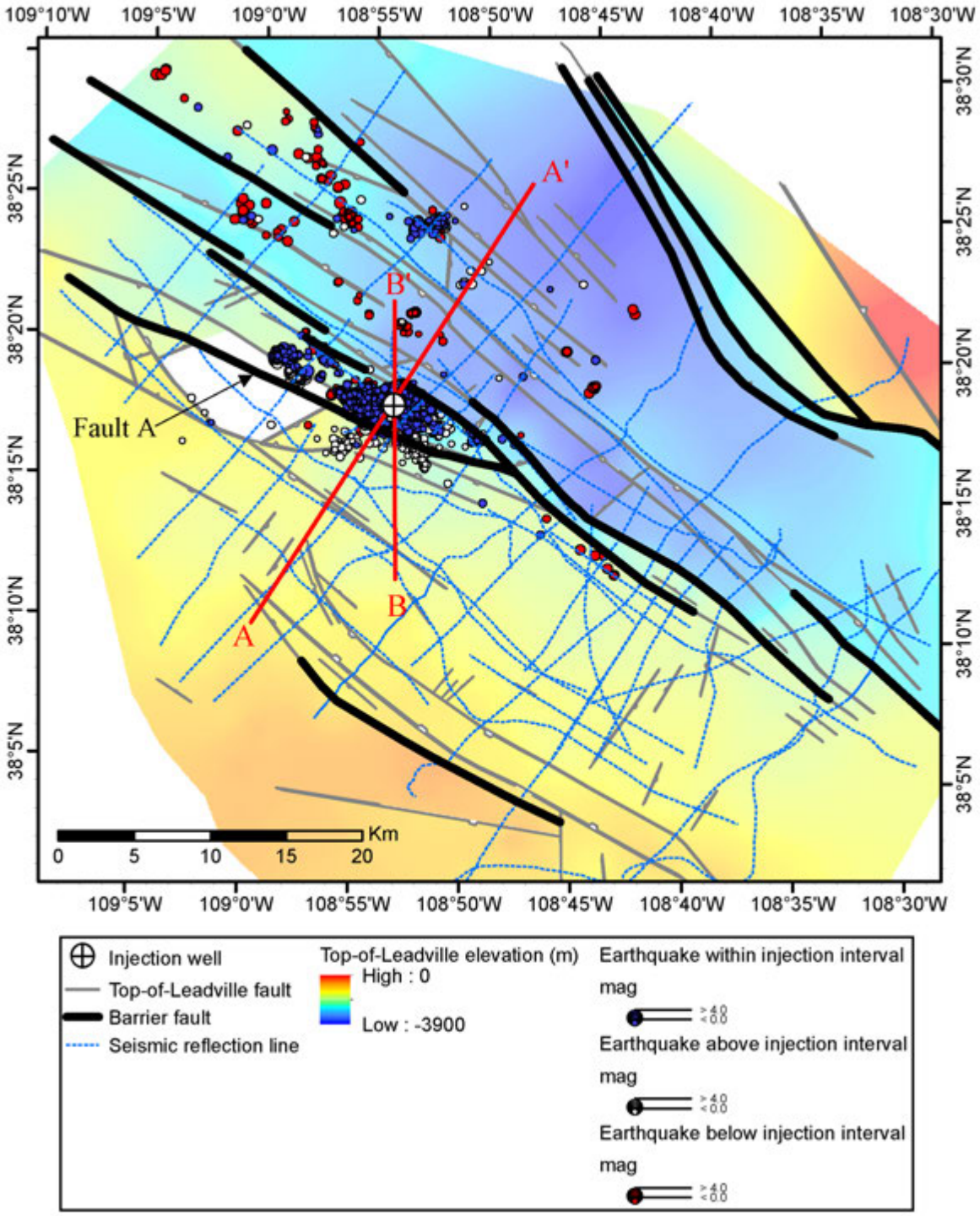

Figure 5-3. Epicenters of earthquakes (≤ 10 km deep) color-coded by their relation to the target injection formations depth interval, overlaid on the structure map of the Leadville formation interpreted from the seismic reflection data. The white area represents a region where the Leadville formation is absent due to erosion. The thick black lines indicate fault segments that we have interpreted as impermeable to lateral fluid flow through the Leadville formation, based on a vertical offset ≥ 500 ft. The red lines indicate the locations of the cross sections presented in Figure 5-4 and Figure 5-5.

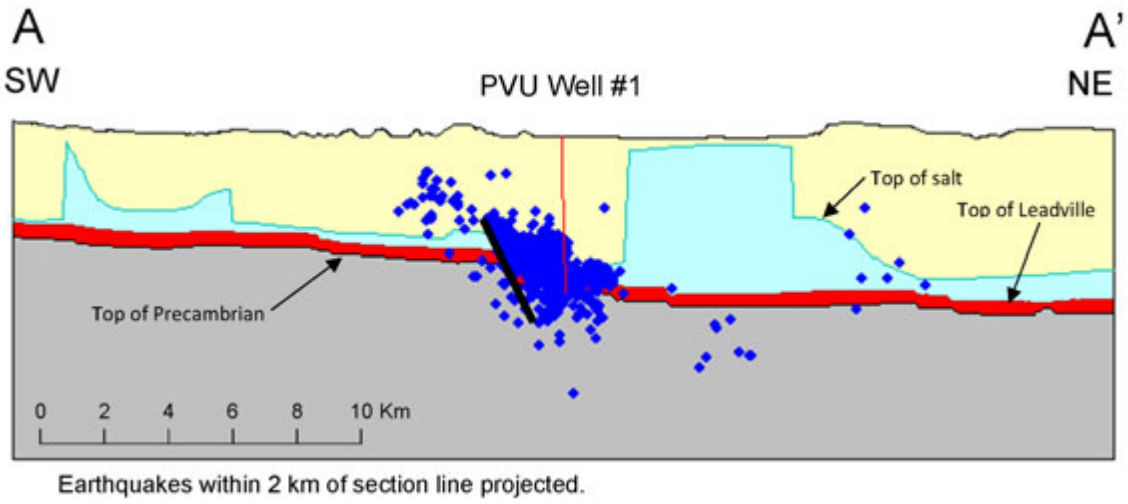

Figure 5-4. Vertical NE-SW trending cross section through PVU Injection Well #1, looking to the northwest (no vertical exaggeration). The location of the cross section is shown on the map in Figure 5-3. Hypocenters of earthquakes within 2 km of the profile are projected onto the cross section. The thick black line represents barrier *Fault A*, which was interpreted from the seismic reflection data based on a criterion of at least 500 ft of vertical offset.

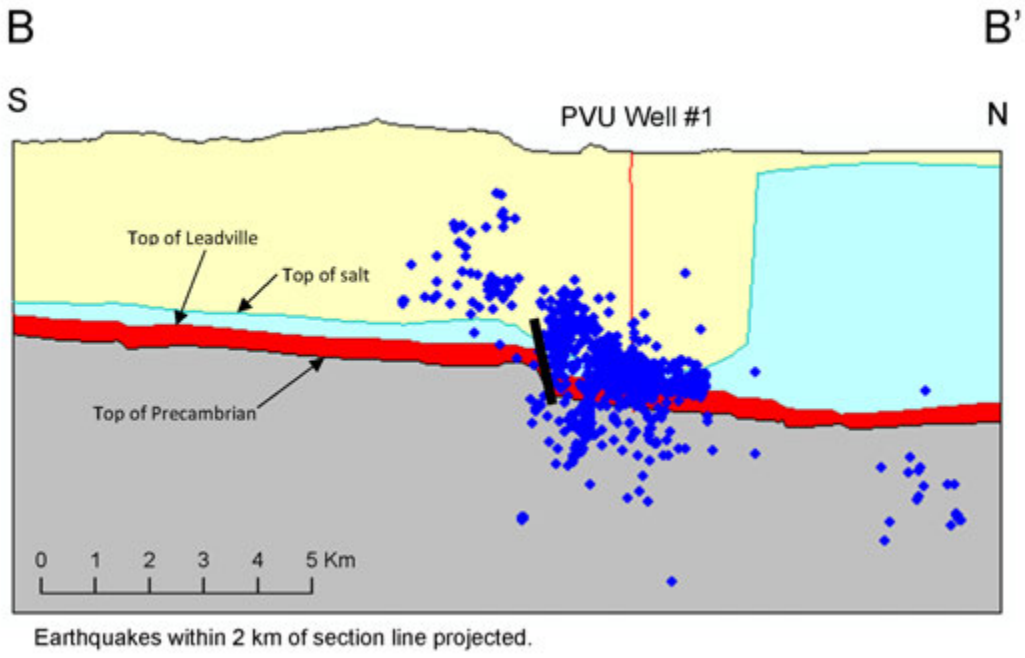

Figure 5-5. Vertical N-S trending cross section through PVU Injection Well #1, looking to the west (no vertical exaggeration). The location of the cross section is shown on the map in Figure 5-3. Hypocenters of earthquakes within 2 km of the profile are projected onto the cross section. The thick black line represents barrier *Fault A*, which was interpreted from the seismic reflection data based on a criterion of at least 500 ft of vertical offset.

into shallow and deeper formations. However, if that were the case, we would anticipate that the elevated pore pressures would also migrate into the Leadville formation on the south side of *Fault A* and trigger induced seismicity within that interval as well. The lack of seismicity within the target injection formations on the south side of *Fault A* lends support to the hypothesis of stress-related triggering of the shallower and deeper seismicity occurring there. More detailed geomechanical modeling may provide additional insights into the occurrence of the earthquakes on the southwest side of *Fault A*.

Leadville structures interpreted during the seismic reflection and hypocenter analyses are compared in more detail in Figure 5-6. The map in this figure shows the area immediately surrounding PVU Injection Well #1 to a distance of ~2 km and the area northwest of the well to a distance of ~9 km. Only earthquakes with a-quality hypocenters are included, since only a-quality hypocenters were used in the previous hypocenter analysis to infer fault locations. The earthquake symbols are color-coded by hypocenter elevation, using the same color scale as the maps and cross sections discussed previously in section 4.4.3. Leadville structures interpreted from the seismic reflection data are labeled in black; those interpreted from the hypocenter analysis are labeled in red. Comparison of the Leadville structures interpreted from the seismic reflection and hypocenter data show both similarities (consistencies) and differences (discrepancies), as discussed below. Features are discussed progressing from the northeast to the southwest.

The location of the barrier fault 1.7 km northeast of the injection well interpreted from the seismic reflection data (Fault B in Figure 5-6) corresponds closely to the location of the impermeable fault interpreted during the hypocenter analysis (Fault 3). This fault was also identified as an impermeable barrier during the seismic reflection analyses performed in the 1980s. The northwest continuation of Fault 3/B was assumed to be a barrier fault during the hypocenter analysis and during the 1980s seismic reflection analyses. In the recent seismic reflection analysis, however, the vertical offset across fault 3/B decreases to the northwest and falls below our 500-ft criterion for a barrier fault in some locations. Instead, the vertical offset is shifted to nearby Fault C. This fault was not identified during the seismic reflection studies performed in the 1980s or during the hypocenter analysis. The earthquakes that span Fault C show no distinct shift in hypocenter elevation (Figure 5-6). However, the seismic reflection interpretation indicates only ~40 m (130 ft) of vertical offset across Fault C near the injection well where most of the seismicity occurs. Extremely few earthquakes span the northwest segment of Fault C that is interpreted to be a flow barrier.

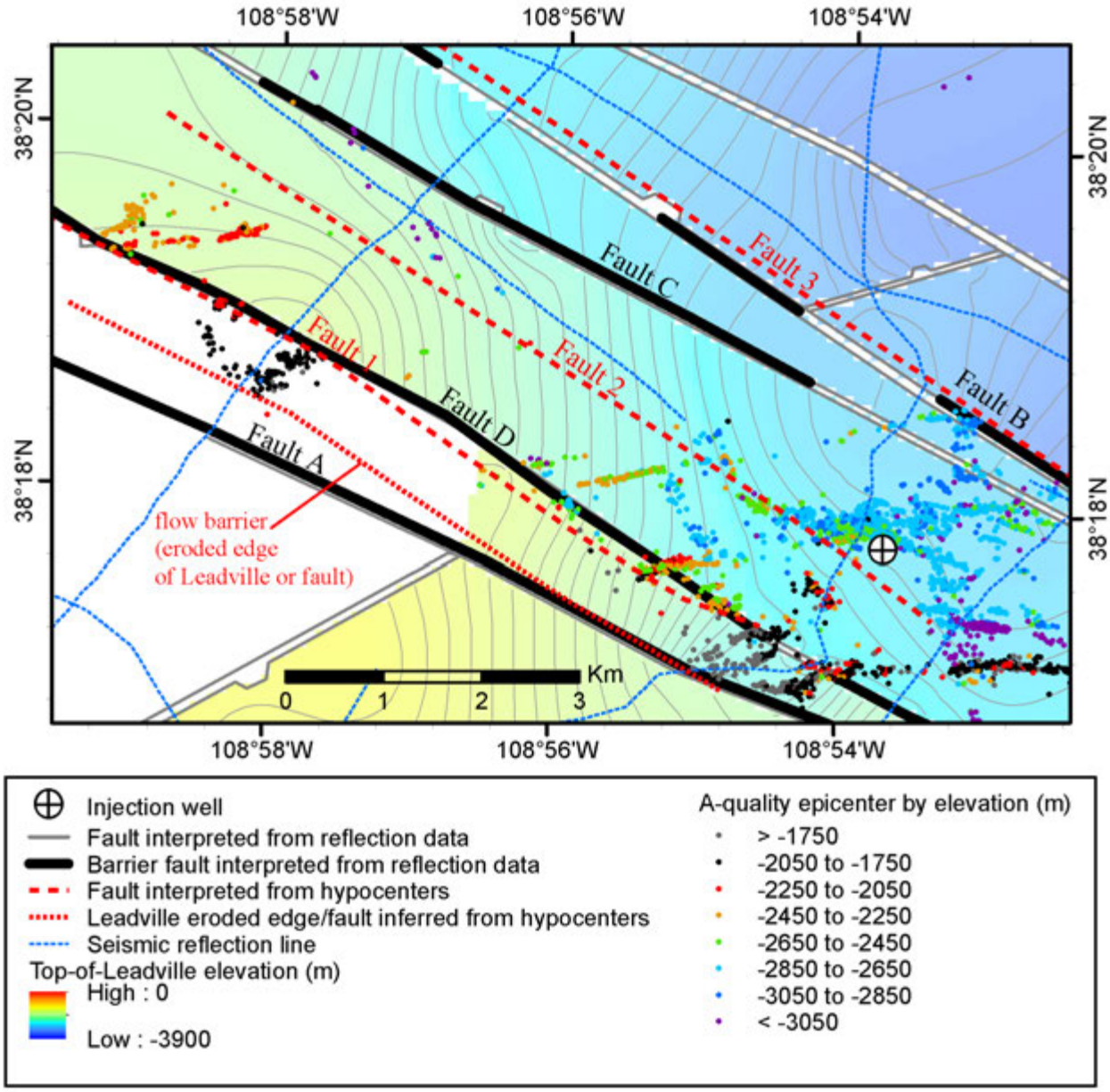

Figure 5-6. Map of the region near and to the northwest of PVU Injection Well #1 showing the structure of the Leadville formation interpreted from the seismic reflection data, earthquakes with a-quality hypocenters, and Leadville structures interpreted previously from these a-quality hypocenters. The thin gray lines are contours of the elevation of the top of the Leadville; the contour interval is 50 m. The white area represents a region where the Leadville formation is absent due to erosion. The thick black lines indicate fault segments that we have interpreted as impermeable to lateral fluid flow through the Leadville formation, based on a vertical offset ≥ 500 ft. The earthquake symbols are color-coded by hypocenter elevation.

No fault was identified during the recent seismic reflection analysis that corresponds to Fault 2 interpreted from the hypocenter analysis (Figure 5-6). The limited seismic reflection data in this area suggests that the change in hypocenter elevations across the interpreted Fault 2 is due to formation dip rather than structural offset. The vertical hypocenter offsets in this area are more gradual and less distinct than near other faults interpreted during the hypocenter analysis (section 4.4.3, Figure 4-30), so interpretation of formation dip rather than structural offset is a reasonable model for both data sets. However, two independent seismic reflection interpretations performed in the 1980s indicate a northwest-trending fault in this location (Figure 3-2; also see Block and others, 2015). Those analyses utilized a higher density of (mostly single-fold) seismic reflection lines within ~10 km of PVU Injection Well #1 than the most recent seismic reflection analysis. Hence, it is also possible that Fault 2 was not identified in the most recent seismic reflection study because of inadequate spatial coverage.

Fault 1 interpreted from the vertical offset of earthquake hypocenters coincides with Fault D from the recent seismic reflection interpretation (Figure 5-6). In the last phase of the seismic reflection interpretation, the location of this fault was adjusted slightly to better match the hypocenter offsets, since there was some uncertainty in the precise location of the fault based on the limited seismic reflection data alone. The vertical offset across Fault D, as indicated by the top-of-Leadville structure map interpreted from the seismic reflection data, is highly variable. Southwest of the injection well (at a radial distance of 1.4 km), in the region where a dense cluster of hypocenters occurs on the southwest side of Fault D, the vertical offset is ~130-150 m (426-492 ft), just below our criterion to be classified as a barrier fault. The vertical offset increases substantially toward the northwest, exceeding 500 m (1640 ft) in the area just south of the region where the Leadville is eroded. In this area, the epicenter lineations truncate at Fault D, with very few earthquakes occurring on the southwest side of the fault. Hence, the hypocenter patterns correlate with the relative vertical offset across Fault D. However, there is nothing in the current model that would prevent pore pressure perturbations in the Leadville formation that cross Fault D at the location where the vertical offset is relatively small from migrating toward the northwest. Hence, either the cluster of seismicity on the southwest side of Fault D is not pore-pressure induced, or there is an unidentified fault northwest of this cluster inhibiting pore pressure migration. The current model shows substantial shallowing of the Leadville formation toward the northwest accommodated by formation dip, but the limited seismic reflection data in this area does not preclude the possibility that some of this shallowing could instead be accommodated by faulting.

As discussed previously, a barrier to lateral fluid flow through the Leadville formation was identified ~2 km southwest of the injection well from the recent seismic reflection analysis (*Fault A*) and from the hypocenter analysis (edge of eroded Leadville or unmapped fault). The features interpreted from these two data sets coincide near the injection well but diverge slightly toward the northwest (Figure 5-6). During the hypocenter analysis, we inferred that the location of the eroded zone or the unmapped fault corresponded to the southwestern edge of the hypocenter cluster 6-7 km northwest of the well (cluster with black epicenters). The recent seismic reflection analysis puts the fault ~0.5 km farther southwest, and no structure in the model from the seismic reflection interpretation coincides with the southwestern edge of the seismicity cluster. Also, the seismic reflection interpretation indicates that this cluster of seismicity occurs

within the Precambrian basement, whereas during the hypocenter analysis it was assumed to occur within the Leadville formation.

During the hypocenter analysis, two alternative fault models were proposed for the area southeast of PVU Injection Well #1 (section 4.4.3, Figure 4-31). These models were proposed to explain a ~900 m vertical offset of hypocenters that occurs approximately 1.5 km southeast of the injection well (Figure 4-30). In one fault model this large vertical offset is explained by a strike-slip fault that juxtaposes two fault blocks with a 900-m difference in the depth to the top of the Leadville formation, and in the other fault model the large offset is explained by a bending and merging of two normal faults. These two fault models are compared to the new seismic reflection interpretation in Figure 5-7. The location of the 900-m vertical offset in hypocenters in labeled as point Y on these maps (blue vs black epicenters), following the nomenclature used previously. A cluster of anomalously deep hypocenters (purple) also occurs at this location.

The recent seismic reflection interpretation shows no faults offsetting the Leadville formation at point Y (Figure 5-7). The top-of-Leadville contours do show an abrupt bending at this location, with the Leadville becoming shallower to the southeast. However, the formation dip is gradual and does not indicate an abrupt change in the elevation of the top of the Leadville formation.

The dense cluster of induced seismicity which occurs near the well at the depths of the target injection formations ends at point Y and does not progress farther to the south. This trend is seen in the maps of a-quality epicenters presented in Figure 5-7 and is presented in cross sectional view in Figure 5-8. The map and cross section in Figure 5-8 include both a- and b-quality hypocenters. As seen in cross section C-C', the vast majority of the earthquakes that occur south of point Y occur shallower than the Paradox salt. This hypocenter pattern is very similar to those seen in the cross sections discussed previously (A-A' and B-B', Figure 5-4 and Figure 5-5), except that the earthquake cluster ends ~2.5 km before reaching the first identified barrier fault (Fault D). Hence, the hypocenter patterns (and the fault models based on them) suggest an impermeable boundary at point Y but the seismic reflection interpretation does not. This is the most substantial discrepancy between the geologic model interpreted from the seismic reflection data and those based on the hypocenter analysis.

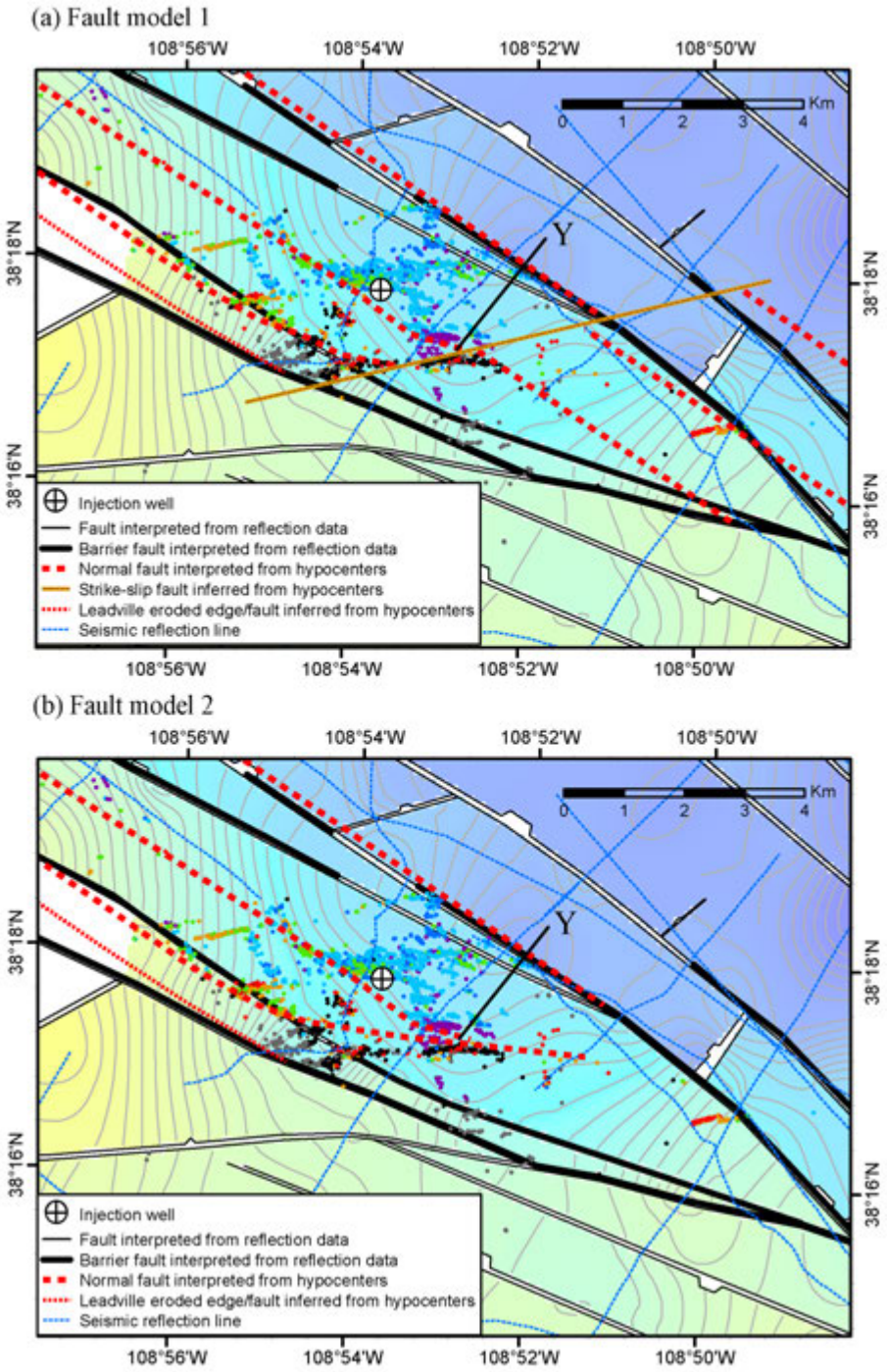

Figure 5-7. Maps of the region near and to the southeast of PVU Well #1 showing the structure of the Leadville formation interpreted from the seismic reflection data, earthquakes with a-quality hypocenters, and two proposed fault models based on the hypocenter patterns. The thin gray lines are contours of the elevation of the top of the Leadville; the contour interval is 50 m. The white area represents a region where the Leadville formation is absent due to erosion. The thick black lines indicate fault segments that we have interpreted as impermeable to lateral fluid flow through the Leadville formation, based on a vertical offset ≥ 500 ft. The earthquake symbols are color-coded by hypocenter elevation using the same scale as in Figure 5-6.

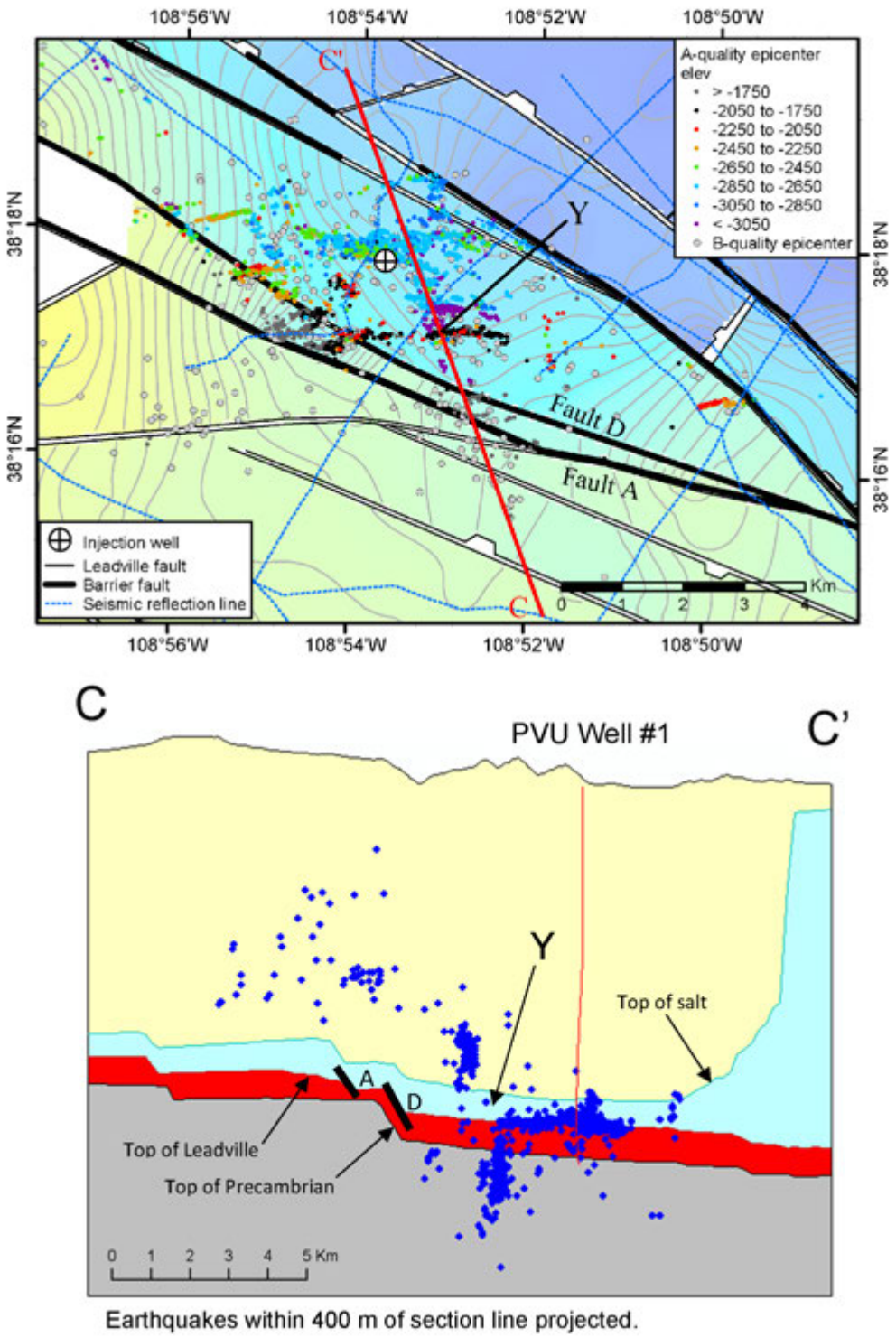

Figure 5-8. Vertical NW-SE trending cross section near PVU Well #1, looking to the southwest (no vertical exaggeration), with map above showing the location of the cross section. Earthquakes (with a- and b-quality hypocenters) within 400 m of the profile are projected onto the cross section. The thick black lines represent barrier faults, which were interpreted from the seismic reflection data based on a criterion of at least 500 ft of vertical offset.

5.1.2 Seismic reflection data and aeromagnetic/gravity data

In Phase 3 of the seismic reflection interpretation, the results of the seismic interpretation were compared to the results of the aeromagnetic interpretation. This comparison showed that both interpretations show predominantly northwest-striking lineations, and some of the major faults from the seismic reflection data are coincident with lineations from the aeromagnetic interpretation. However, many of the details of the two studies differ. This is expected, as the 3D modeling of the aeromagnetic data showed that much of the variation in the magnetic anomaly is caused by changes in basement composition, which cannot be imaged by seismic reflection data, while the seismic reflection data shows a greater level of structural detail than can be imaged by the aeromagnetic data.

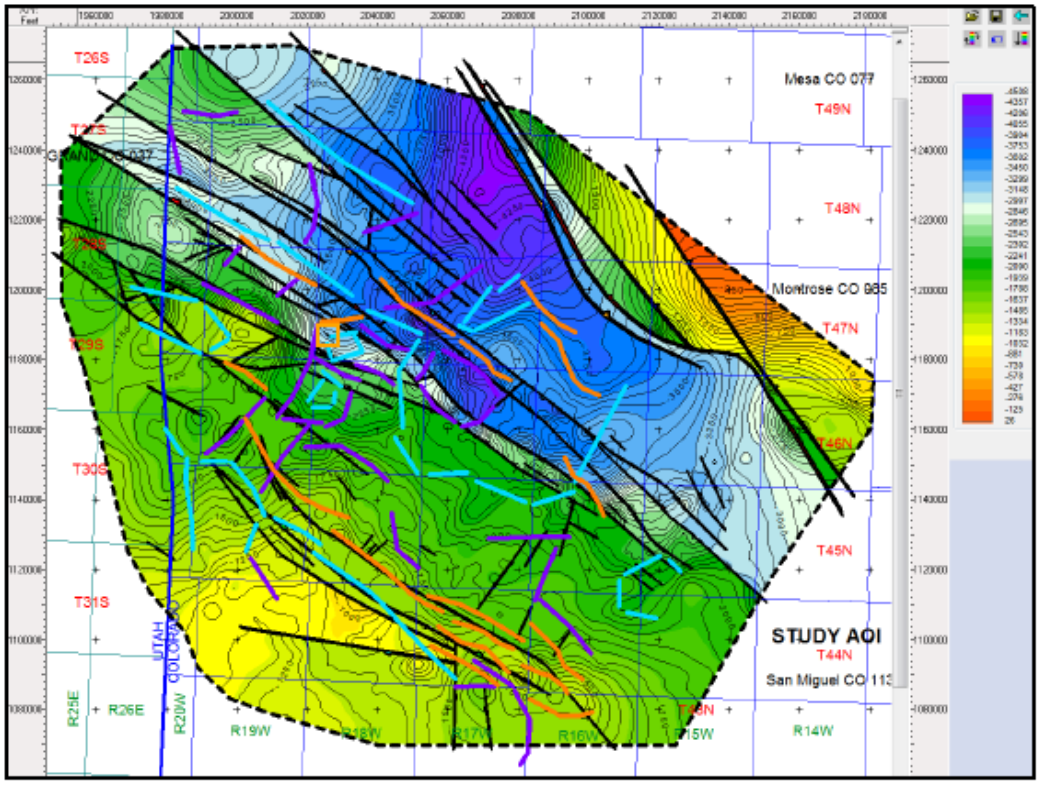

Figure 5-9. Aeromagnetic survey interpreted features overlain on Precambrian structure from seismic and well interpretations. See Section 4.3.3.2 and Figure 4-20 for descriptions of aeromagnetic survey interpreted features. Location of PVU Injection Well #1 is indicated by the gold square. Figure taken from Arestad (2017).

5.2 Geomechanical and flow modeling

A coupled 3D geomechanical and flow model of the area of interest was created using Itasca's commercial numerical code, *FLAC3D* (Detournay and Dzik, 2017) using a partially uncoupled approach. The primary purpose of the model was to compare the relative pressure response at potential second well sites. To validate the model, modeling was first done for injection at the site of PVU Injection Well #1, using the flow rate history and adjusting the model to match the

observed wellhead pressures. The model was then used to simulate injection at five potential second well sites.

The subsurface was modeled as a six-layer saturated porous medium with isotropic permeability in small strain mode. The grid size was 100 meters vertically and 400 meters horizontally. All fluid was injected into the Leadville, with the surface of the Leadville and the locations and throws of faults provided by the seismic reflection interpretation (Figure 5-10).

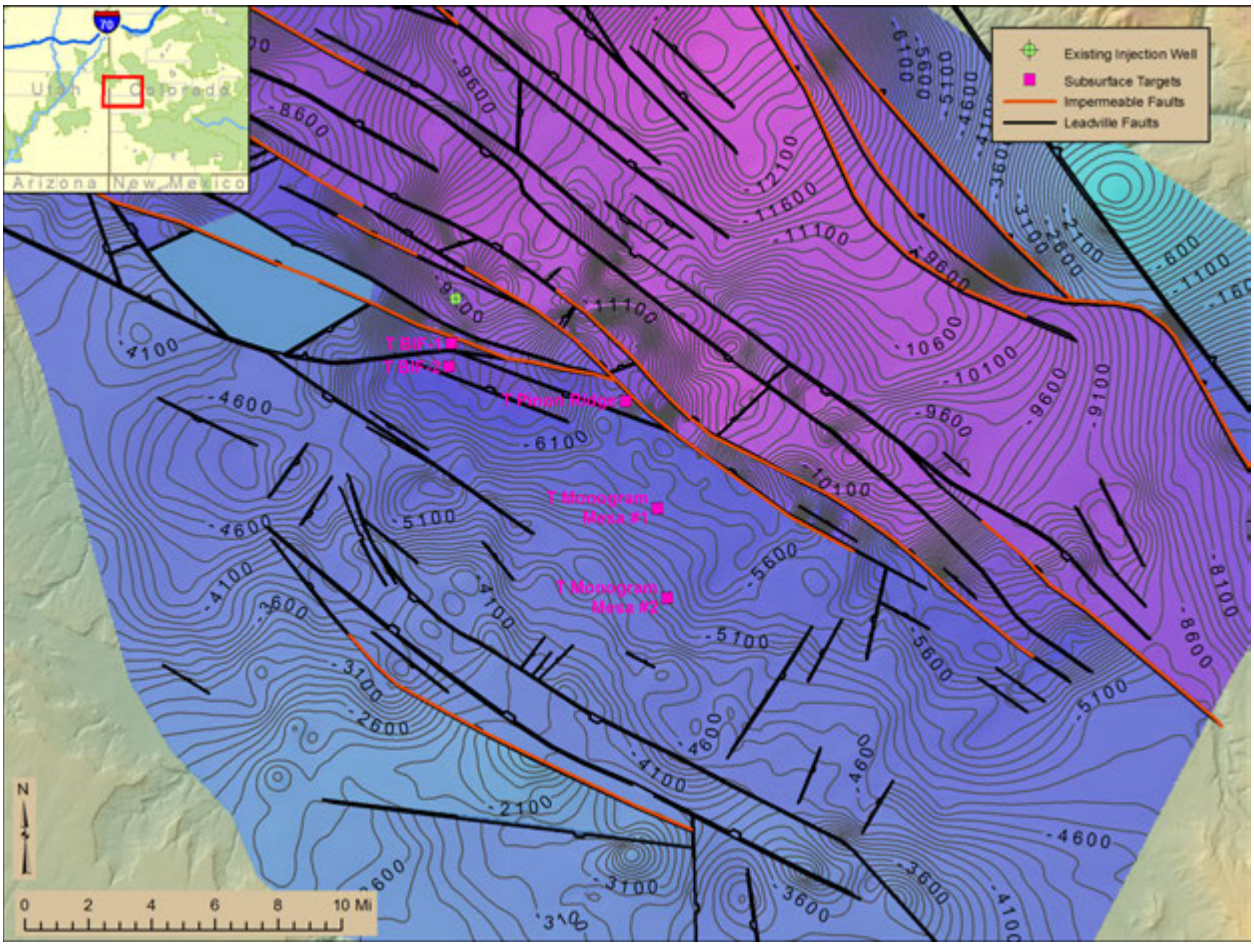

Figure 5-10. Leadville surface used for geomechanical modeling. The black lines show all faults identified by the seismic reflection interpretation, while the red lines show major fault segments with greater than 500 feet of vertical offset, which are interpreted as being potentially impermeable in the modeling. Contours represent elevations at the top of the Leadville, in feet. For the geomechanical modeling, vertical wells were assumed at each of the target sites (magenta squares).

5.2.1 Data

The depths and reservoir properties of six layers were provided to Itasca by Reclamation. The properties are listed in Table 5-1. The fluid was assigned a viscosity of 0.001348 Pa-sec and a density of 1.153 g/cm^3, based on an average of the measured densities for the 70:30 brine/freshwater mixture and the 100% brine, weighted by their injected volumes. However, for the purposes of flow modeling, the fluid was assigned a density of 1.0 g/cm^3.

Descriptions of the tops of each layer are also included in Table 5-1. The base of each layer is the top of the underlying layer. The Leadville formation and top layer of the Precambrian basement were both assigned constant thicknesses of 100 meters. While the actual Leadville thickness varies spatially, we have limited data to constrain the variations, and most of the variations are less than the model's vertical resolution of 100 meters. The thickness of the Precambrian basement that had significant permeability was 58 meters in PVU Injection Well #1. We have no other data points on the Precambrian basement permeability, but chose to assign a permeable layer of uniform thickness at the top of the Precambrian basement.

The densities were calculated from the well log of PVU Injection Well #1. Densities were only logged for depths below 14,043 feet; the remaining densities are calculated from the sonic logs (King, 2017).

Table 5-1. Formation properties used in the coupled geomechanical and flow modeling, along with a description of the top of each layer. Table modified from Detournay and Dzik (2017).

Layer	1	2	3	4	5	6
Layer description	Formations above salt	Salt	Leadville	Sedimentary layers below Leadville	Precambrian	Lower Precambrian
Density (g/cm^3)	2.53	2.16	2.69	2.56	2.65	2.65
Bulk modulus (GPa)	29.8	25.3	64.8	50.6	50.1	50.1
Young's modulus (GPa)	43.1	35.8	76.2	66.8	83.0	83.0
Shear modulus (GPa)	17.1	14.2	29.2	26.1	33.9	33.9
Poisson's ratio	0.260	0.264	0.304	0.280	0.224	0.224
Permeability (mD)	0.1	0	6	0.1	1.5	0
Porosity	0.06	0	0.05	0.01	0.03	0
Diffusivity (m^2/s)	0.0020	0	0.21	0.0044	0.053	0
Layer top	Surface	Top of salt[1]	Top of Leadville[1]	100 meters below top of Leadville	Top of Precambrian[1]	100 meters below top of Precambrian

[1]Surface taken from the seismic reflection interpretation

The shear modulus μ, bulk modulus K, Young's modulus E, and Poisson's ratio ν are calculated from the well logs using the following formulae:

$$\mu = \rho V_S^{\,2} \tag{5.1}$$

$$K = \rho\left(V_P^{\,2} - \frac{4}{3}V_S^{\,2}\right) \tag{5.2}$$

$$E = 2\mu(1+\nu) \tag{5.3}$$

$$\nu = \frac{3K - 2\mu}{6K + 2\mu} \tag{5.4}$$

The values of V_P and V_S for layers 3-6 were calculated from the well logs for PVU Injection Well #1. Because a shallow log of V_S was not available for PVU Injection Well #1, V_P and V_S values for layer 1 and layer 2 were taken from the logs of the well 05-085-06039, located about 13 km to the west of PVU Injection Well #1.

The value of diffusivity for the Leadville formation prior to 8 January 2002 was taken from the moveout of seismicity (King and Block, 2016). In the same report, average long-term permeability was calculated from pressure/flow modeling to be ~18 mD. Since we here used a layer thickness of 100 meters (which is slightly greater than the thickness of 90 meters that was determined to be the "prime reservoir" from petrophysical data and used in King and Block, 2016), we scaled the permeability down to 6 mD, since the pressure increase is dependent on the product of permeability and thickness, so for a given pressure increase, the permeability is inversely proportional to thickness. Porosity ϕ was then calculated using the formula:

$$\phi = \frac{k - D\mu C}{D\mu C_f} \tag{5.5}$$

where C is the rock compressibility, calculated as the inverse of the bulk modulus, and C_f is the fluid compressibility, calculated from the fluid temperature (assumed to be 37.8°C) and viscosity.

The salt was assumed to have a porosity, permeability, and diffusivity of 0. For the other layers, porosities were calculated from the sonic logs, using assumed matrix slownesses of 50.0 μs/ft for the Precambrian basement and 51.3 μs/ft for the other layers, and fluid slowness of 190 μs/ft. Since the matrix slowness is dependent on lithology, which is variable, these porosities are only approximate. From an early spinner survey, we know that the Leadville formation accepted ~80% of the fluid, and so a permeability value of the Precambrian was chosen to make the product of permeability and thickness of the Precambrian to be approximately 16% of that of the Leadville, assuming that some portion of the fluid is also accepted by the sedimentary layers below the Leadville. The permeabilities of the other layers (1 and 4) are qualitatively described as very low, but we have no numerical estimates for these values. Permeabilities of 0.1 mD were assumed for both layers. For layer 4, the product of permeability and thickness is calculated to be approximately 6% of that of the Leadville. Diffusivity for the layers other than the Leadville was then calculated from equation (5.5), rearranged as:

$$D = \frac{k}{\mu\left(C + \phi C_f\right)} \tag{5.6}$$

5.2.2 Results

To calibrate the model using pressure and flow data from PVU Injection Well #1, five modeling cases were considered:

(1) Layers above Leadville were impermeable; Leadville and underlying layers were permeable; transparent faults (meaning that the faults had no distinct properties, and their only effects were in offsetting the layers.

(2) Leadville was the only permeable layer; all faults were impermeable.
(3) All layers except salt were permeable (with values shown in Table 5-1); transparent faults.
(4) All layers except salt were permeable (with values shown in Table 5-1); salt had zero thickness at locations of salt welds shown on Figure 4-8; transparent faults.
(5) All layers except salt were permeable (with values shown in Table 5-1); salt had zero thickness at locations of salt welds shown on Figure 4-8; faults with throws of at least 500 feet (152 meters) were impermeable.

The addition to the modeling of salt welds with zero salt thickness was done to account for the simplification of considering the entire layer between the top of the salt and the top of the Leadville formation to be salt, when in reality there are sedimentary layers between the base of the salt and the top of the Leadville formation. The effect of adding the salt welds was to reduce the numerical wellhead pressure prediction by a quasi-uniform value in time of approximately 2 MPa (Detournay and Dzik, 2017).

The major conclusion from this model calibration was that a partially compartmentalized reservoir containing both permeable and impermeable faults (model 5) is the only one able to reproduce the major trends in the pressure history observed at PVU Injection Well #1 (Figure 5-11), particularly in Phases III-V (beginning at approximately 3×10^8 seconds; see King and Block (2016) for a description of the injection phases. While we cannot definitively distinguish whether individual faults are permeable or impermeable, the selection of faults was based on the subsurface geology, as determined from the seismic reflection interpretation, and produces a good fit to the trend in the pressure rise over the last 15 years. The locations of these barrier faults are shown in Figure 5-1.

The geomechanical and flow modeling calculated a maximum value of uplift caused by the volume that has been currently injected at PVU Injection Well #1 of 2.1-3.5 cm, depending on the assumed value of the Biot coefficient (Detournay and Dzik, 2017). This is consistent with the constraint provided by the analysis of InSAR data (Besana-Ostman, 2016), which found no coherent signal resulting from PVU injection, leading to an upper bound on the maximum uplift of approximately 10 cm.

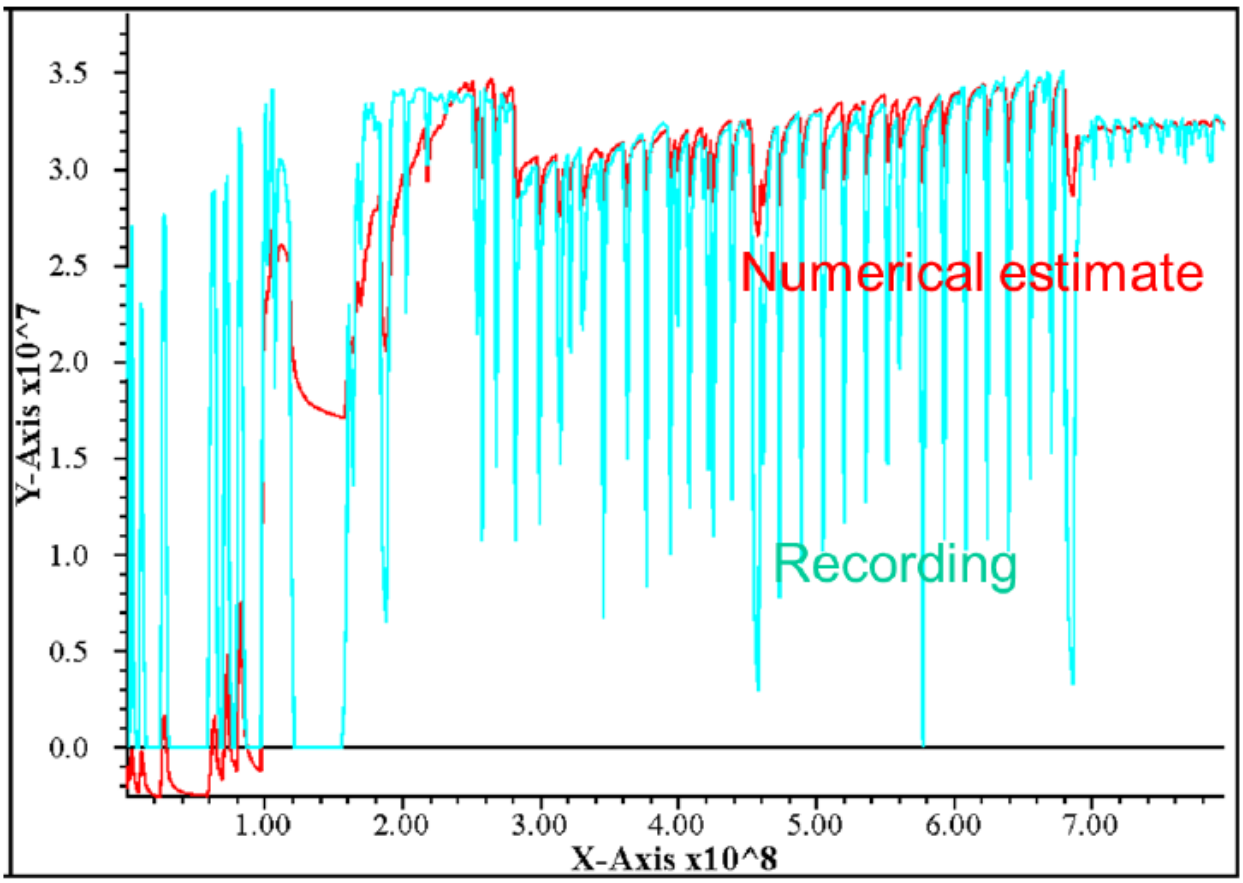

Figure 5-11. Wellhead pressure (Pascals) versus time (seconds) for PVU Injection Well #1. Blue line is the observed pressure; red line is the modeled pressure using Model 5 with a well pressure correction term adjusted to best fit the observed pressure. Figure taken from Detournay and Dzik (2017).

5.3 Formation Properties

5.3.1 Properties of confining layer

5.3.1.1 Salt thickness

Salt thickness is an important factor in siting a second injection well. Very thick salt may increase drilling costs and may make it more difficult to maintain a stable wellbore over the anticipated life of the well. Very thin salt, on the other hand, may not serve as an adequate confining layer to prevent the upward migration of the injectate. While the exact thickness of salt needed to serve as an adequate confining layer has not been determined, the studies in the 1980s used a minimum thickness of 250 feet (Bremkamp and others, 1984; Katz and Carroll, 1984). The salt thickness is highly variable in the study area, with thickness ranging from 0 or nearly 0 to more than 14,000’ thick.

5.3.1.1.1 Welds

Salt welds are defined as areas where the salt is too thin to be resolved on the seismic reflection data. In some cases the salt thickness may be 0 in that location; in other cases it might be up to a couple hundred feet thick. In the absence of well data, we are unable to distinguish between these

cases. There are several salt welds within the AOI, as shown on Figure 4-8, all of which are interpreted to be northwest-trending. Many of the salt welds are located near salt diapirs, and in cases where the seismic reflection lines are relatively sparse, the boundary between the welds and diapirs might not be well defined.

5.3.1.1.2 Diapirs

There are three major salt diapirs within the study area, beneath Paradox Valley, Sinbad Valley, and Gypsum Valley. While all of these diapirs were known prior to the start of this study, this study helped to better define their thickness and lateral extent. The salt diapir beneath Paradox Valley is more than 14,000' thick in the thickest part, and the salt diapir beneath Sinbad Valley is more than 13,000' thick. The salt diapir beneath Gypsum Valley is somewhat thinner, with a thickness ranging up to about 8000 ft.

Drilling through salt of considerable thickness is certainly possible, as evidenced by the Conoco Scorup Somerville Wilcox #1 well, which was drilled in 1958 to a depth of 15,000', through more than 11,000' feet of salt. However, drilling a well through this thickness of salt and maintaining a stable wellbore for the anticipated life of the well would create substantial complexities that should be carefully considered prior to selecting a well site in such an area.

5.3.1.2 Salt quality

The selection of the Paradox salt as a confining layer was determined by its impermeability (Bremkamp and Harr, 1988). However, in some places the salt is interfingered with clastic materials, which may call into question its adequacy as a confining layer. Near the Uncompahgre front, mud logs show that a facies change from dominantly salt to dominantly siliciclastics occurs over a distance of 5 miles (Figure 4-10). Figure 5-12 shows this facies change in cross-section view. Were an injection well to be sited in this area, more study would be needed to determine the suitability of the siliciclastic wedge or other materials overlying the Leadville formation to act as an adequate confining layer.

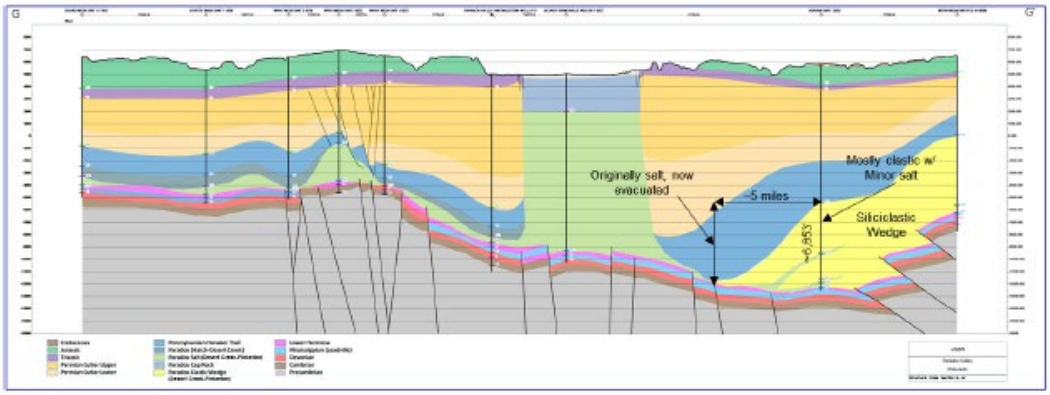

Figure 5-12. Structural cross section G-G' showing the location of rapid facies change from salt to siliciclastics near the Uncompahgre uplift. See Figure 4-10 for cross-section location. Figure taken from List (2016).

5.3.2 Characteristics of Leadville formation

5.3.2.1 Porosity and Permeability

The porosity and permeability of the Leadville formation are important characteristics in siting an injection well. These reservoir properties cannot be determined from seismic reflection data or other surface data, and thus the only data points we have are from wells. Specifically, we have calculated porosities from sonic logs. As shown in Figure 4-13, the porosity is highly variable and shows no obvious spatial correlation. The majority of wells have higher calculated Leadville porosities than PVU Injection Well #1, which is promising for the purposes of siting an injection well.

The only estimates of permeability are in PVU Injection Well #1. Injection testing showed approximately permeabilities of 4-8 mD (Harr, 1988; Envirocorp Services and Technology Inc., 1995). The permeability estimates obtained from analyzing the diffusion of induced seismicity with time range from 1-8 mD, depending on the value of diffusivity selected and whether the grains and pores are assumed to be incompressible (King and Block, 2016). Pressure-flow modeling using a radially symmetric model (King and Block, 2016) and geomechanical modeling (Detournay and Dzik, 2017) both showed consistency with the pressure history using a product of permeability and thickness of approximately 600 mD-m. The permeability determined from this modeling is dependent on the assumed value of the Leadville thickness, but is consistent with the estimates from injection testing and diffusion of induced seismicity for a Leadville thickness of approximately 100 meters.

Analysis of core samples from the Conoco-Scorup well located approximately 4.6 km to the northeast yielded permeabilities ranging from 0.03 to 1.3 mD (Harr, 1989). While it is expected that permeability measured from core samples will be lower than permeability calculated from injection testing, this may suggest significant regional variations in permeability.

The location of PVU Injection Well #1 was selected, in part, on its proximity to the northwest-trending Wray Mesa fault system (Bremkamp and Harr, 1988). Like most limestones, the Leadville formation has low primary porosity, and therefore we expect both the porosity and permeability to be dominated by pre-existing fractures and faults. While some large faults were imaged by the seismic reflection interpretation, the distribution of smaller pre-existing faults and fractures in the AOI is not well known.

5.3.2.2 Depth

The depth to the Leadville formation significantly influences the drilling cost. Drilling costs are often reported in dollars per foot, reflecting the tendency of drilling costs to scale approximately linearly with depth. The depth to the Leadville formation, in feet, is shown in Figure 5-13. The depth ranges from approximately 7,000 to 19,000 feet within the AOI. This map was created by subtracting the elevation of the Leadville determined from the seismic reflection interpretation from the ground surface elevation. In some cases where the topography is steep, directionally drilling from a place with a lower surface elevation might lead to a shorter path to the Leadville than drilling vertically from the surface.

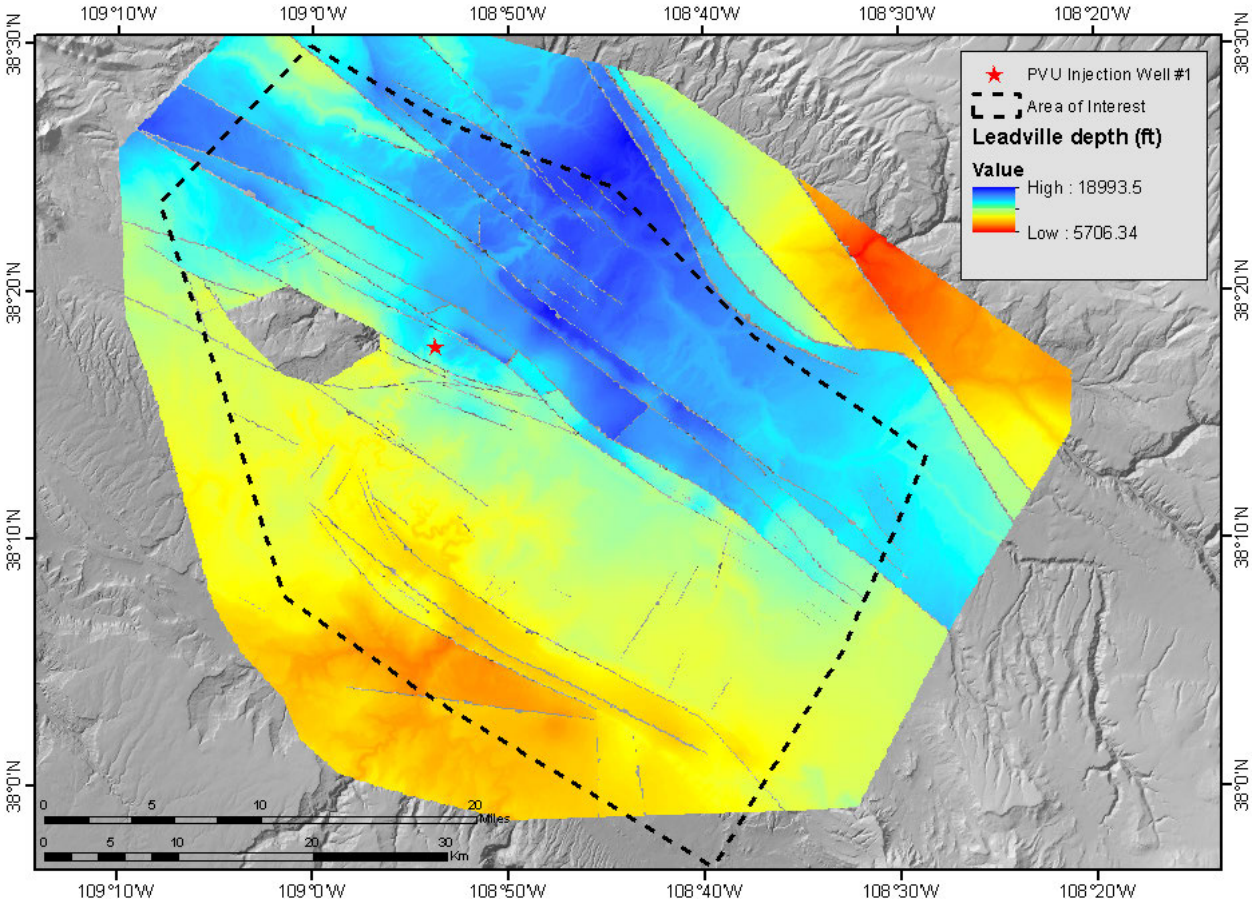

Figure 5-13. Depth to the Leadville formation, in feet, calculated from the Phase 3 seismic interpretation and the ground surface elevation. Red star shows the location of PVU Injection Well #1.

5.3.2.3 Thickness

Thick Leadville formation is a desirable characteristic for siting a second injection well, as it increases the reservoir volume. Unfortunately, the amount of information about the Leadville thickness is relatively limited, as it was not possible to reliably image the Ouray formation (the formation directly below the Leadville) on the seismic reflection data. Thus, the only direct information we have about the thickness of the Leadville formation is from well logs. There are 37 wells for which we have tops of both the Leadville and Ouray formations, from which the Leadville thickness can be calculated (not counting two wells for which well logs are unavailable, as we have no way to verify these tops). There were two additional wells that did not encounter the Leadville formation but did reach underlying layers, indicating that the Leadville is eroded in that area. These two wells are located in the Wray Mesa area (Figure 4-6). An isopach map created from well data is shown in Figure 4-11. Note that there is significant variation in the density of well data, with most of the wells that penetrated the Leadville formation located in the southern and western portions of the AOI. Outside the area where the Leadville is eroded, the Leadville thickness ranges from ~50 feet to ~450 feet.

5.3.2.4 Lateral extent of reservoir

The lateral extent of the reservoir influences the volume that can be injected while keeping the pressure increase at an acceptable level. If the reservoir is too small, the life of the injection well will be shortened. The only known area where the Leadville formation is eroded is on Wray

Mesa (Arestad, 2016), and thus the primary controls on the lateral extent of the reservoir are the locations of impermeable faults. The locations of fault segments with throws of at least 500 feet, which we consider to be impermeable, are shown in Figure 5-14. As discussed in Section 5.2.2, we cannot verify whether each of these faults are impermeable, but the geomechanical modeling results do suggest a partially compartmentalized reservoir with some impermeable faults surrounding PVU Injection Well #1. The impermeability of the fault southwest of PVU Injection Well #1 is also supported by the distribution of earthquake hypocenters (Section 5.1.1). The impermeability of the fault system on the southwest flank of the Uncompaghre Uplift is supported by the potentiometric surface determined from DST data (Figure 4-12). If our selection of impermeable fault segments is accurate, there are a few places where the reservoir is bounded on at least two sides by faults less than 3 km apart. These places include to the southeast of PVU Injection Well #1, on the northeast side of the AOI, and to the northwest of the AOI, where impermeable fault segments overlap. The locations are denoted by cross-hatching in Figure 5-14. Because the criteria used for selecting impermeable faults was somewhat arbitrary, the length of the impermeable fault segments may be greater or less than what is mapped.

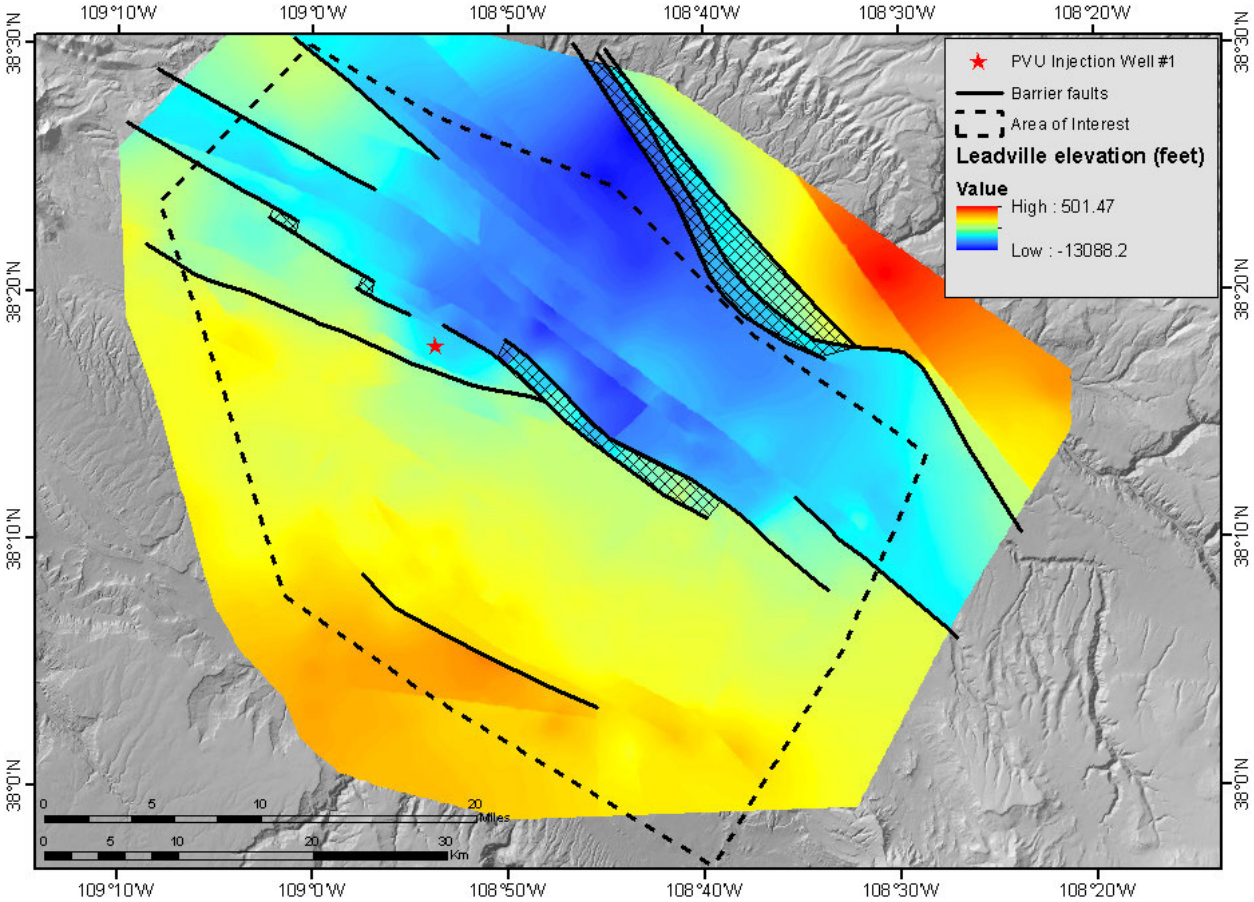

Figure 5-14. Leadville elevation and barrier faults. Areas with cross-hatching show locations with barrier faults separated by less than 3 km.

Additionally, the pressure increase at the wellhead is significantly influenced by the proximity of injection to an impermeable fault. Should a second injection well site near a major mapped fault be selected, the location of the fault should be further refined and the influence on the pressures due to that fault should be modeled.

5.3.2.5 Hydrologic isolation

It is highly desirable to inject into a reservoir that has not already been pressurized by injection into PVU Injection Well #1, for the purposes of keeping the pressure increase and induced seismicity within acceptable levels. For a reservoir to not be already pressurized, it must either be a sufficient distance from PVU Injection Well #1, or separated from PVU Injection Well #1 by an impermeable barrier. There are no monitoring wells in which to measure pressures away from the wellhead, and thus we must use insights from the subsurface structure, geomechanical modeling, and extent of induced seismicity to determine the spatial extent of pressurization from injection into PVU Injection Well #1.

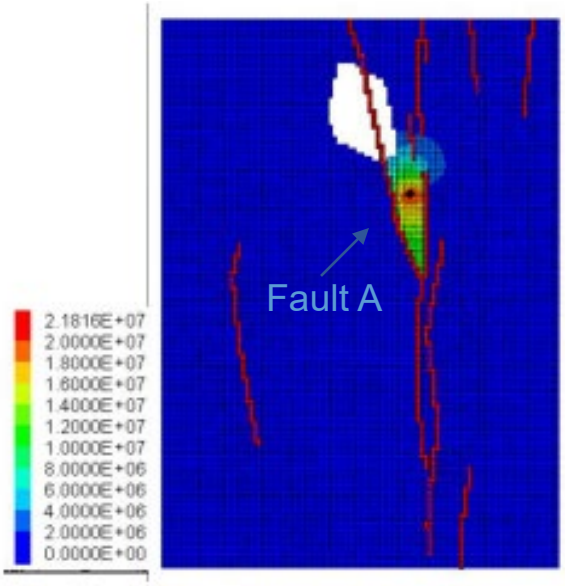

Figure 5-15. Excess pore-pressure, in Pascals. This simulation used model 5, described in Section 5.2.2, and the flow rate history at PVU Injection Well #1 through the end of 2016. Figure taken from Detournay and Dzik (2017). The map is in rotated coordinates, parallel to Paradox Valley.

As discussed in Sections 5.1.1 and 5.3.2.4, the seismic reflection interpretation, geomechanical modeling, and extent of induced seismicity all provide supporting evidence for the existence of an impermeable fault southwest of PVU Injection Well #1 (*Fault A*), and thus we do not expect the reservoir on the southwest side of that fault to have experienced significant pressurization.

The geomechanical modeling results suggest that the pore-pressure increase from PVU Injection Well #1 exceeding 2 MPa is primarily contained between *Fault A* and the faults along the edge of Paradox Valley (Figure 5-15). However, the spatial extent of induced seismicity is much larger, with shallow earthquakes having been recorded at distances of up to about 20 km from PVU Injection Well #1. Thus, either the spatial extent of pore-pressure increase is much larger than modeled, the amount of pore-pressure increase needed to induce earthquakes is very small, or these earthquakes are induced by stress changes rather than pore-pressure increase. However, the move-out of induced seismicity is fit relatively well by a pore-pressure diffusion model (King and Block, 2016), providing support for pore-pressure triggering.

Induced seismicity has occurred around the northern edge of Paradox Valley since 2000, and, in recent years, has also occurred beneath Paradox Valley (Section 4.4.2). While the path of pore-pressure migration to these areas is not clear, and, again, the presence of seismicity is not definitive proof of pore-pressure increase, it does suggest that these areas might have been pressurized by injection into PVU Injection Well #1. The induced seismicity in and on the east side of the southern half of Paradox Valley is much more sparse. There are no mapped faults separating the northern and southern halves of Paradox Valley, and thus it is unknown whether there is a flow barrier that was not able to be identified on the seismic reflection data, or whether there is a flow path to this area and the sparsity of seismicity is for another reason, such as a lack of pre-existing faults or less critical stress conditions.

6 Conclusions

To aid in the site selection for a potential second injection well at the Paradox Valley Unit, several studies were undertaken to improve our knowledge of subsurface conditions. These studies were conducted within a 750-mi^2 (1942-km^2) area encompassing Paradox and Gypsum Valleys and the surrounding region. Data from nearly 600 miles (1000 km) of 2D seismic reflection lines, 90 deep wells, public-domain gravity surveys, a high-resolution aeromagnetic survey, induced earthquakes, and InSAR images were utilized in these studies. Geomechanical and flow modeling was also performed and provided additional insights on geologic considerations for siting an injection well. Results from these studies have improved our knowledge of the lithology, geologic structure, stress state, and likely characteristics of fluid flow within the study area.

In this report, we have summarized the most important results from the individual studies, and we have compared their interpretations of the subsurface. While there are some inconsistencies between interpretations that require further investigation, results from the various analyses are largely complementary and suggest the following conclusions:

- The Leadville formation is a feasible primary injection target because it appears to be present throughout most of the study area, except for a relatively small area where it likely was uplifted and eroded.

- The porosity of the Leadville formation is spatially variable. The limited porosity data available from deep wells in the region yield average Leadville porosity estimates of 0-6%. The majority of wells have higher Leadville porosities than PVU Injection Well #1. Leadville permeability estimates in PVU Injection Well #1 range from ~1-8 mD, and insufficient data are available to reliably assess its spatial variation.

- Depths to the top of the Leadville formation within the study area range from approximately 7,300 to 19,000 ft (2,225 to 5,791 m) and generally increase toward the northeast. The thickness of the Leadville formation varies from ~50 ft (15 m) on structural highs to ~450 ft (137 m), except for one area where the Leadville is fully eroded.

- The Paradox salt formation is a feasible confining layer for injection into the Leadville formation because it is present in considerable thickness for many locations within the study area.

- The thickness of the Paradox salt formation varies from < ~200 ft (61 m) (below the resolution of the seismic reflection data) to >14,000 ft (4267 m). The Paradox salt transitions from nearly pure halite in most of the study area to dominantly siliciclastics in the northeastern region.

- The sub-salt formations are vertically offset by numerous faults. Most of the major faults trend NW-SE, but northeast-trending faults have also been identified. Some of the faults have enough vertical offset to juxtapose the Leadville formation against formations with virtually no effective permeability, creating a barrier to lateral fluid flow. These barrier faults all trend NW-SE, indicating that large-scale flow of injected fluid through the Leadville formation will be preferential in that direction.

- A barrier fault ~2 km southwest of the injection well appears to hydrologically isolate the reservoir for PVU Injection Well #1 from the area to the south and west of the fault. Both the large offset across the fault indicated by the seismic reflection interpretation and the scarcity of induced earthquakes within the Leadville formation on the southwest side of the fault suggest that the fault is impermeable to fluid flow through the Leadville. Additionally, the geomechanical modeling suggests that an impermeable fault model provides a better fit to the observed pressure and flow history at PVU Injection Well #1.

- Ground surface uplift due to injection into PVU Injection Well #1 is estimated to be less than 4 cm, based on geomechanical modeling. This uplift cannot be resolved on InSAR images, as they are dominated by anomalies of up to 10 cm related to other factors such as soil expansion/contraction.

- Regional Paradox Basin pore pressures within the Leadville formation are approximately hydrostatic, with a composite pressure gradient of 0.47 psi/ft. The trend of the Leadville potentiometric surface is consistent with fluid recharge being along the west flank of the San Juan Mountains and the west flank of the Uncompahgre uplift, northeast of our study area.

- The regional *in situ* total principal stresses are oriented in the vertical and horizontal directions, with the maximum horizontal stress $S_{H\max}$ direction approximately N78°W. The magnitude of the total vertical stress $S_{Vertical}$ is approximately the lithostatic load. Assuming a transitional strike-slip to normal faulting stress state, the magnitudes of the total *in situ* horizontal stresses are estimated by $S_{h\min} \approx 0.6\, S_{H\max}$, and $S_{H\max} \approx S_{Vertical}$.

References

Ake, J., Mahrer, K., O'Connell, D., and Block, L., 2005, Deep-injection and closely monitored induced seismicity at Paradox Valley, Colorado: Bulletin of the Seismological Society of America, v. 95, no. 2, p. 664-683.

Allis, R.G., Morgan, C.D., Heuscher, S., and McDonald, A., 2009, Regional Middle Paleozoic Hydrodynamic Pressure Regime of the Paradox Basin, Utah and Colorado, *in* Thomas C. Chidsey, J., ed., The Mississippian Leadville Limestone Exploration Play, Utah and Colorado - Exploration Techniques and Studies for Independents: Salt Lake City, Utah Geological Survey, p. 20.

Arestad, J.F., 2016, Paradox Valley Unit Seismic Data Interpretation Phase 2 Report: Excel Geophysical Services and International Reservoir Technologies, Inc., 62 p.

Arestad, J.F., 2017, Paradox Valley Unit 2D Phase 3 Seismic Report: Detailed Site Interpretation: Excel Geophysical Services and International Reservoir Technologies, Inc., 114 p.

Baars, D.L., and Stevenson, G.M., 1981, Tectonic Evolution of the Paradox Basin, Utah & Colorado, *in* Wiegand, D.L., ed., Geology of the Paradox Basin: Denver, Colorado, Rocky Mountain Association of Geologists, p. 23-31.

Besana-Ostman, G., 2016, Identification of Deformation in Paradox Valley using InSAR Bureau of Reclamation.

Block, L., Yeck, W., King, V., Derouin, S., and Wood, C., 2012, Review of Geologic Investigations and Injection Well Site Selection, Paradox Valley Unit, Colorado: Bureau of Reclamation, 62 p.

Block, L.V., 2017, Trends of Induced Seismicity and Pressures Following the 2013 Change in Injection Operations at the Paradox Valley Unit, Colorado: Bureau of Reclamation, technical Service Center Technical Memorandum TM-85-833000-2017-10, 76 p.

Block, L.V., Wood, C.K., Yeck, W.L., and King, V.M., 2015, Induced seismicity constraints on subsurface geological structure, Paradox Valley, Colorado: Geophysical Jounal International, v. 200, p. 1172-1195.

Bremkamp, W., and Harr, C.L., 1988, Area of Least Resistance to Fluid Movement and Pressure Rise, Paradox Valley Unit Salt Brine Injection Project, Bedrock, Colorado, 39 p.

Bremkamp, W., Harr, C.L., and Prather, O.E., 1984, Geophysical interpretation - Seismic data, Paradox Valley Unit, Montrose County, Colorado, 24 p.

Campbell, J.A., 1981, Summary of Paleozoic stratigraphy and history of western Colorado and eastern Utah, *in* Epis, R.C., and Callender, J.F., New Mexico Geological Society Thirty-Second Field Conference, New Mexico Geological Society, p. 81-88.

Condon, S.M., 1997, Geology of the Pennsylvanian and Permian Cutler Group and Permian Kaibab Limestone in the Paradox Basin, Southeastern Utah and Southwestern Colorado: U. S. Geological Survey, 59 p.

Detournay, C., and Dzik, E., 2017, Geomechanical and Flow Modeling for Paradox Valley Unit, Study for USBR: Summary Report: Itasca Consulting Group, Inc., 337 p.

Dewan, J.T., 1987, Re: BOR Paradox Valley Injection Test Well #1: Acquisition of Logs in the Liner Hole (15,950 to 14,050 ft): Houston, Dewan & Timko, Inc., p. 7.

Dewan, J.T., 1988, Re: BOR Paradox Valley Injection Test Well #1. Interpretation of Logs Run in Liner Hole.: Houston, Dewan & Timco, Inc., p. 32.

Doelling, H.H., 1988, Geology of Salt Valley Anticline and Arches National Park, Grand County, Utah, Salt Deformation in the Paradox Region: Salt Lake City, Utah, Utah Geological and Mineral Survey, p. 1-60.

Dubiel, R.F., Huntoon, J.E., Stanesco, J.D., and Condon, S.M., 2009, Cutler Group alluvial, eolian, and marine deposystems: permian facies relations and climatic variability in the Paradox Basin: The Paradox Basin revisited new developments in petroleum systems and basin analysis.

Dunn, C.S., 1987, Letter No. 510-FL-601 (Revised) Test Results - Internal Casing Test and Open Hole Leak-off Test No. 1, Fenix & Scisson, Inc., p. 8.

Eaton, B.A., 1969, Fracture Gradient Prediction and Its Application in Oilfield Operations.

EDCON-PRJ, 2016, Data acquisition and processing of a high-resolution aeromagnetic survey, Paradox Valley, Colorado and Utah Contract No. R16PX00104, 95 p.

Envirocorp Services and Technology Inc., 1995, Report of Evaluation of Injection Testing for Paradox Valley Injection Test No. 1: Durango, CO, Bureau of Reclamation, p. 67 p.

Excel Geophysical Services, 2016, Data Processing Report, Paradox Valley Unit, Colorado and Utah, Phase 2, 26 p.

Friedman, J.D., Case, J.E., and Simpson, S.L., 1994, Tectonic trends of the northern part of the Paradox Basin, southeastern Utah and southwestrn Colorado, as derived from Landsat Multispectral Scanner imaging and geophysical and geologic mapping, *in* Huffman, A.C.J., ed., Evolution of sedimentary basins - Paradox Basin: U. S. Geological Survey, p. C1-C30.

Grout, M.A., and Verbeek, E.R., 1998, Tectonic and Paleostress Significance of the Regional Joint Network of the Central Paradox Basin, Utah and Colorado, in Laccolith Complexes of Southeastern Utah: Time of Emplacement and Tectonic Setting, U. S. Geological Survey.

Gutierrez, F., 2004, Origin of the Salt Valleys in the Canyonlands Section of the Colorado Plateau - Evaporite-dissolution Collapse versus Tectonic Subsidence: Geomorphology, v. 57, p. 423-435.

Harr, C.L., 1988, Final geological well report, Bureau of Reclamation Injection Test Well No. 1, Paradox Valley, 30-47N-18W, Montrose County, Colorado: Bureau of Reclamation, 141 p.

Heidbach, O., Rajabi, M., Reiter, K., and Ziegler, M., 2016, WSM Team (2016): World Stress Map Database Release 2016, *in* Services, G.D.

Hite, R.J., 1975, An unusual northeast-trending fracture zone and its relations to the basement wrench faulting in northern Paradox Basin, Utah and Colorado, Four Corners Geological Society Guidebook, 8th Field Conf., Canyonlands: Durango, CO, Four Corners Geological Society, p. 217-223.

Huntoon, P.W., 1988, Late Cenozoic Gravity Tectonic Deformation Related to the Paradox Salts in the Canyonlands Area of Utah, Salt Deformation in the Paradox Region, Utah: Salt Lake City, Utah, Utah Geological and Mineral Survey, p. 79-93.

Jaeger, J.C., Cook, N.G.W., and Zimmerman, R., 2007, Fundamentals of Rock Mechanics (4th ed.), Blackwell Publishing Ltd., 488 p.

Katz, L.J., and Carroll, R., 1984, Geophysical Interpretation of Seismic Data, Paradox Valley Unit, Utah Geophysical, Inc., p. 31.

King, V., and Block, L., 2016, Evidence for Far-field Reservoir Pressurization, Paradox Valley, Colorado: Bureau of Reclamation, 97 p.

King, V.M., 2017, Compilation of Well Data in the Vicinity of Paradox Valley, CO Bureau of Reclamation, 155 p.

King, V.M., Block, L.V., Yeck, W.L., Wood, C.K., and Derouin, S.A., 2014, Geological structure of the Paradox Valley Region, Colorado, and relationship to seismicity induced by deep well injection: Journal of Geophysical Research: Solid Earth, v. 119, p. 1-24.

List, D., 2016, Paradox Valley - Geologic Support for Seismic Data Interpretation Phase 2 Report: Excel Geophysical Servies and David List Consulting, Inc., 54 p.

Martínez-Garzón, P., Kwiatek, G., Ickrath, M., and Bohnhoff, M., 2014, MSATSI: A MATLAB Package for Stress Inversion Combining Solid Classic Methodology, a New Simplified User-Handling, and a Visualization Tool: Seismological Research Letters, v. 85, no. 4, p. 896-904.

McClure, K., Morgan, C.D., Thomas C. Chidsey, J., Eby, D.E., and Scott, P., 2003, Heterogeneous Shallow-Shelf Carbonate Buildups in the Paradox Basin, Utah and Colorado: Targets for Increased Oil Production and Drilling Techniques, Deliverable 1.1.2, Regional Paradox Formation Cross Sections, Blanding Sub-Basin, Utah and Colorado: Utah Geological Survey, 29 p.

McKenzie, D.P., 1969, The relation between fault plane solutions for earthquakes and the directions of the principal stresses: Bulletin of the Seismological Society of America, v. 59, no. 2, p. 591-601.

Nuccio, V.F., and Condon, S.M., 1996, Burial and Thermal History of the Paradox Basin, Utah and Colorado, and Petroleum Potential of the Middle Pennsylvanian Paradox Formation: U. S. Geological Survey, 47 p.

Rasmussen, D.L., 2014, Namakiers in Triassic and Permian Formations in the Paradox Basin (USA) with Comparisons to Modern Examples in the Zagros Fold Belt, Iran, *in* MacLean, J.S., Biek, R.F., and Huntoon, J.E., eds., Geology of Utah's Far South: Salt Lake City, Utah, Utah Geological Association.

Reeves, C., 2005, Aeromagnetic Surveys: Principles, Practice & Interpretation, 155 p.

Thomas, W.A., 2007, Pennsylvanian sinistral faults along the southwest boundary of the Uncompahgre uplift, Ancestral Rocky Mountains, Colorado: Geosphere, v. 3, no. 3, p. 119-132.

USGS, 2016, InSAR--Satellite-based technique captures overall deformation "picture", v. 2016, no. June 15.

Walker, J.D., and Geissman, J.G., 2009, Geologic Time Scale: Geological Society of America, 1 p.

Wang, H., Detournay, E., Dusseault, M., Fehler, M., and Frohlich, C., 2015, Report from the Consultant Review Board On Paradox Valley Unit – MASIP / Induced Seismicity, Meeting No. 1, January 28-31, 2015, Grand Junction, Colorado: Bureau of Reclamation, 35 p.

Williams, P.L., 1964, Geology, structure, and uranium deposits of the Moab quadrangle, Colorado and Utah 360 [Report].

Wintermoon Geotechnologies, 2016, Interpretation Report: Data Enhancement, Map-based Interpretation, and Integrated 2D Modeling, 56 p.

Wintermoon Geotechnologies, 2017, Aeromagnetic Interpretation: 3D Modeling, 28 p.

Zoback, M.D., 2007, Reservoir Geomechanics, Cambridge University Press, 449 p.